-

Non-equilibrium phase separation in active matter

Yuting Li

PhD supervisor: Prof. M. E. Cates

Trinity College

This thesis is submitted for the degree of Doctor of Philosophy.

21st October, 2021

Declaration

This thesis is the result of my own work and includes nothing which is the outcome of work done in collaboration except as declared in the Preface and specified in the text. I further state that no substantial part of my thesis has already been submitted, or, is being concurrently submitted for any such degree, diploma or other qualification at the University of Cambridge or any other University or similar institution except as declared in the Preface and specified in the text. It does not exceed the prescribed word limit for the relevant Degree Committee

Chapters 2 and 3 have been published as [1], chapter 4 has been published as [2] and chapter 5 has been published as [3].

Yuting Li
21st October, 2021

Summary

Non-equilibrium phase separation in active matter

Yuting Li

Active matter, characterised by the ability to inject energy into the environment locally, forms an important class of non-equilibrium systems. Recently there has been a surge of interest in active systems with chemical reactions, fuelled in particular by studies in biomolecular condensates, or 'membraneless organelles', within cells. In contrast to their passive counterparts, such systems have conserved and non-conserved dynamics that do not, in general, derive from a shared free energy. This mismatch breaks time-reversal symmetry (TRS) and leads to new types of dynamical competition that are absent in or near equilibrium. We construct a canonical scalar field theory to describe such systems, with conserved and non-conserved dynamics obeying Model B and Model A respectively (in the Hohenberg-Halperin classification), chosen such that the two free energies involved are incompatible. The resulting minimal model is shown to capture the various phenomenologies reported previously for more complicated models within this class, including microphase separation, limit cycles and droplet splitting.

To expand upon the systematic study of non-equilibrium reaction-diffusion systems, we also consider that the diffusive dynamics can break time reversal symmetry in its own right. This happens only at higher order in the gradient expansion, but is the leading behaviour without reactions present. We incorporate the higher gradient terms into Model AB and show that for slow reaction rates the system can undergo a new type of hierarchical microphase separation, which we call 'bubbly microphase separation'. In this state, small droplets of one fluid are continuously created and absorbed into large droplets, whose length-scales are controlled by the competing reactive and diffusive dynamics.

Motivated by the distinct non-equilibrium nature of active systems, we introduce the entropy production rate (EPR) as a quantitative measure of time reversal symmetry breaking. It can be defined either at the particle level or at the level of coarse-grained fields such as the density; the EPR for the latter quantifies the extent to which these

coarse-grained fields behave irreversibly. In this work, we first develop a general method to compute the EPR of scalar Langevin field theories with additive noise (this large class includes the aforementioned Model AB). Treating the scalar field ϕ as the sole observable, we arrive at an expression for the EPR that is non-negative for every field configuration and is quadratic in the time-antisymmetric component of the dynamics. Our general expression is a function of the quasipotential, which determines the full probability distribution for field configurations, and is not generally calculable. To alleviate this difficulty, we present a small-noise expansion of the EPR, that only requires knowledge of the deterministic (mean-field) solution for the scalar field in steady state, which generally is calculable, at least numerically. We demonstrate this calculation for the case of Model AB. We then present a similar EPR calculation for Model AB with the conservative and non-conservative contributions viewed as separate observable quantities. The results are qualitatively different, confirming that the field-level EPR depends on the choice of coarse-grained information retained within the dynamical description.

Acknowledgements

I would first like to thank my supervisor Mike for giving me the opportunity to study active matter and his insightful guidance throughout my PhD. I would also like to thank my colleagues Rosalba Garcia Millan and Étienne Fodor for their patience and persistence.

I am grateful to be a part of the Cambridge Soft Matter group, which provided a warm and supportive working environment. In particular, I benefited greatly from many helpful discussions as well as kind code donations from Rajesh Singh, Elsen Tjhung, Yongjoo Baek and Cesare Nardini. I would like to thank my academic advisor Rob Jack for providing a fresh perspective into my research and a lot of helpful advice for academic life. I would also like to thank all members of the Pyross project, led by Ronojoy Adhikari, for a welcome distraction and a sense of purpose during the Covid pandemic.

Finally, I would like to thank the Cambridge Trust and the Jardine Foundation for their generous financial support, and Trinity College for providing a friendly community, food and a bed for 8 years.

Contents

Chapter 1

Introduction

Active matter, broadly classified as systems where energy is continuously injected on a microscopic scale, has been the focus of intensive theoretical and experimental study in recent years [4–7]. Examples of active matter are abundant in nature: bird flocks, fish schools, bacteria colonies and cell layers; artificial active systems such as shaken grains [8] and vibrated polar disks [9] have also been studied in labs due to their close resemblance to biological systems.

In addition to its relevance in various areas of biology, we are interested in active matter for its unique statistical physics properties. Active matter is distinct from most driven systems (e.g. constant electrical current down a wire, boundary driven fluids) because the forcing is applied locally, whereas most driven systems have built-in anisotropy as a result of macroscopic driving. In other words, while most driven systems have *macroscopic* time reversal symmetry (TRS) breaking, active matter breaks TRS on a *microscopic* scale without imposing global driving. Macroscopic currents can still arise naturally in active systems, as well as a wealth of intriguing non-equilibrium collective behaviours that are qualitatively different from their equilibrium counterparts, including giant number fluctuations [4], microphase separation (pattern formation on a finite scale) [10, 11], and long-range correlations in order-disorder transition [12, 13]. Understanding the emergence of these macroscopic structures from purely local interactions is pivotal to the study of active matter.

1.1 Construction of active field theories

In a typical biological system, due to the sheer number of variables required to track the exact state of a single cell, it is not feasible to formulate a complete description of the dynamics. Therefore we must filter out information to reach an effective theory that is analytically or computationally manageable. One can then connect the parameters of effective theory to more detailed, smaller length-scale behaviours to build a hierarchy of

theories if one wishes. In this thesis we are interested in the collective phenomena of active matter, where the important length-scale is far above the size of an individual active agent. We utilise a tool that has been hugely successful in equilibrium physics: theories of coarse-grained fields that maintain the symmetries and conservation laws of the degrees of freedom of interest. In particular, we focus on field theories of a scalar variables $\phi(x,t)$ that can represent the coarse-grained density at position x, or in case of binary mixtures, the chemical composition variable. There have also been a huge amount of studies on systems with polar or nematic (also known as headless vector) degree of freedom, but they are beyond the scope of this thesis and we refer to these excellent reviews [4, 5] for further details .

Generally, there are two methods of constructing active field theories: the bottom-up approach where we explicitly coarse-grain from an (often abstract and simplified) microscopic model of how individual active agents behave; and the top-down approach where we start with the desired symmetries and conservation laws and build a theory using the lowest order Landau-Ginzberg terms. The two approaches can often be connected with each other by expanding around a uniform state and assuming that the deviation is small. For example, to study the phenomena of motility induced phase separation (MIPS) in self-propelled systems, one can start with the equation of motion for a microscopic model for self-propulsion, such as active Brownian particles [14], run-and-tumble particles [15, 16] or active Ornstein-Uhlenbeck particles (AOUPs) [17, 18], and coarse-grain via Dean's Equation [19] to arrive at a set of Langevin equations for the density field [6, 20]. This is the bottom-up approach. Alternatively, we can write down all the Landau-Ginzberg terms order by order in (ϕ, ∇) that are consistent with mass conservation and isotropy (but importantly, time reversal symmetry is no longer required). At low orders, the result is identical to equilibrium Model B in Hohenberg and Halperin's classification [21], but at order (ϕ^2, ∇^4) we encounter the first TRS-breaking terms, named λ-term and ζ-term in Tjhung et al. [11]. It has been shown that the latter model, called Active Model B+, can be obtained via explicit coarse-graining of an AOUPs-like microscopic model followed by expansions around a uniform state [11].

In chapters 2, 3 and 4 we present a minimal scalar field theory, called Model AB, for a novel class of active systems, characterised by the coexistence of phase-separating conservative dynamics and chemical reactions (defined as processes that change particle number), with no detailed-balance condition linking the two sectors. There has been a large body of literature dating back to the 1990's [22–24] where simulations were done for immiscible liquids with externally maintained chemical reactions, as well as recent resurgence of interest due to its relevance to biological systems. One prominent context has been membraneless organelles, also known as biomolecular condensates, whose active environment can maintain chemical reactions away from equilibrium. Another example

is bacteria: on a long timescale, the intrinsic birth-death dynamics, combined with motility-induced phase separation lead to various novel phenomena not seen in passive counterparts. The characteristics of phase separation across these models are distinct from their equilibrium counterparts, in that microphase separation is often observed without any energetic cause. (In equilibrium, the latter requires long-range interactions mediated by charged species or block copolymers, for example [25, 26].) This suggests, like MIPS, the physics of all these distinct systems can be captured schematically by an active field theory based on minimal ϕ^4-type ingredients.

1.2 Statistical physics of active field theories

In equilibrium, microscopic particle dynamics obey time reversal symmetry (TRS), meaning that the probability of observing a movie of a forward particle trajectory is the same as observing the reverse. Upon coarse-graining to mesoscopic field theories, TRS is manifested as the principle of detailed balance: forward and backward paths among coarse-grained states must still have equal probability in thermal equilibrium. This leads to the equilibrium Boltzmann distribution as well as the well-known fluctuation-dissipation theorem.

In contrast, active matter are far from equilibrium, where none of the above apply. Recent emergence of a new field known as "stochastic thermodynamics" provides a novel framework for understanding the statistical physics of non-equilibrium systems. In particular, starting with general, model-independent considerations, one can write down fluctuation theorems that connect the probabilities of the forward and backward paths to the work done on the system, and hence generalise the concept of entropy production to systems with no energy conservation [27–30].

From an informatic point of view, the entropy production is a quantitative answer to the question: given certain information about the system, how irreversible does the dynamics appear? Sometimes the strong non-equilibrium nature of the underlying microscopic interactions (e.g. self propulsion, chemical driving) do not survive the coarse graining procedure [31] – the dynamics can appear equilibrium-like on a scale much larger than the individual agents [6, 11]. To address this, Nardini et al. extended the definition of the entropy production to field theories by comparing the probability of a forward path and its reverse, quantifying the amount of time reversal symmetry breaking at the macroscopic level [32]. In chapter 5, we build upon the results of Nardini et al. [32] and study the instantaneous field theoretic entropy production rate (EPR) of the general class of scalar field theories with addictive noise. This large class includes equilibrium Model A and Model B in Hohenberg and Halperin's classification [21], as well as their non-equilibrium extensions, such as driven diffusive models [33] and Active Model B+ [6, 11]. The resulting general expression for the EPR is non-negative for all field configurations, in line with the

Second Law of thermodynamics. Lastly, using Model AB as a case study, we demonstrate that the EPR obtained is qualitatively different depending on the amount of information tracked along the trajectories.

Chapter 2

Canonical Model AB

The problem of phase separation in an immiscible binary liquid of molecules or polymers undergoing chemical reactions was considered in a series of papers in the mid 1990's [22–24, 34–37]. In steady state, such chemical reactions were found by simulation, and argued theoretically, to create microphase separation (such as layered phases of finite wavelength) in place of the bulk phase separations seen for immiscible molecules of constant chemistry. However it was soon clarified that microphase separation can happen only under conditions where the chemical reactions are held out of equilibrium [38]. This outcome is required by the general principle that thermodynamic equilibrium is determined solely by the free energy landscape (expressed as a function of the chemical potentials or densities of the various species) and not by kinetic details such as chemical reaction rates. This reasoning holds so long as those rates are chosen to respect the detailed balance condition with respect to the same free energy as governs the phase separation – as must be the case for systems at, or close to, equilibrium. Only far from equilibrium can a steady-state structure emerge whose properties depend on reaction rates, as arises for the microphase separations reported in [22–24, 34, 35].

Recently there has been a resurgence of interest in the case of strongly non-equilibrium phase separation with chemical reactions – which we define here as all processes that change particle type or number, including for instance the birth and death of micro-organisms such as bacteria. One major context has been cell biology, where non-membrane-bound compartments of cells, also called biomolecular condensates or membraneless organelles, can be regarded as phase separated liquid-liquid mixtures [39–41]. These structures reside in the active environment of living cells which can drive chemical reactions far from equilibrium. Models based on these principles account for multi-droplet morphologies observed in some organisms [42, 43] where a mechanism involving equilibrium phase separation alone would (for short-ranged interactions among species) generically lead to one single large droplet per cell. In addition, self-propelled bacteria subject to population dynamics fall into the same general class, and exhibit some similar phenomena [44, 45].

The general class in question is characterised by the non-equilibrium combination of a phase separating mechanism that conserves the total particle density (or composition variable in the case of liquid mixtures), and population dynamics or driven chemical reactions that allows non-conservative variations, with no detailed-balance condition linking the two sectors. Take bacteria as an example: these are known to undergo motility-induced phase separation as a result of lower swim speed in dense regions [6]; the total density is conserved in this process. Separately, bacteria can reproduce via cell division and die as a result of over-crowding; this is the non-conservative part of the dynamics. Similarly, in subcellular fluid mixtures, the chemical reactions among phase-separating species consumes fuel and generates waste, whose concentrations are maintained externally, driving the system far from equilibrium [7].

In this chapter we propose a canonical model for this class of systems via separate Landau-Ginzburg expansions of the conservative and non-conservative dynamics. The outcome is a combination of Model B and Model A, as defined by Hohenberg and Halperin [21], with chemical potentials that are mismatched. Note that in active systems these chemical potentials need not even stem from free energies, let alone a shared one [46, 47]. (This is because activity can result in gradient terms not present in either Model A or B, both of which were originally constructed for near-equilibrium systems only [21].) However, for simplicity of the analysis, and to retain a parameter space of reasonable dimensions, here we focus on the lowest-order non-equilibrium theory, which minimally disequilibrates conservative and non-conservative sectors that would each observe time-reversal symmetry in isolation. (Note that the relevant coarse-grained equations of motion in each sector can be equilibrium-like, in this sense, even if the underlying microphysics is totally irreversible [6].) Time-reversal symmetry is then generically broken directly by the incompatibility of the two free energies that drive the conservative and non-conservative aspects of the dynamics.

As we shall see, however, it is possible to find a low-dimensional subspace of parameters for the coupled model in which time-reversal symmetry is accidentally restored for the dynamics of the density (albeit not of the current). In this fine-tuned subspace, we will map the dynamics of the stochastic non-equilibrium field theory onto one with an altered combination of conserved and non-conserved dynamics that allows an effective free energy to be identified. This exact mapping supersedes one reported previously at mean-field level only (i.e., neglecting fluctuations) [48–50]; it establishes complete dynamic equivalence to an equilibrium system with certain long-range interactions. However, as the phenomena seen in some micro-inspired models are clearly incompatible with equilibrium (such as limit cycles that blatantly break time reversal symmetry), we then introduce the canonical form of our model that fully captures the non-equilibrium nature of the more complicated models.

The chapter is organised as follows. In section 2.1, model AB is introduced. Section 2.2 discusses the special case where an equilibrium mapping exists. Next, in section 2.3, we present the canonical choices of the chemical potentials, followed by a demonstration of arriving at the same model via explicit coarse graining of a microscopic lattice model in section 2.4.

2.1 Construction of the canonical model

We shall present a canonical model for this class of systems, found as a combination of Model B for the conservative sector and Model A for the non-conservative relaxation. Model A and Model B were among those systematically catalogued in the 1970's, from conservation laws and symmetry considerations, to describe the dynamical approach to equilibrium [21]. In principle, each can be separately generalized to non-equilibrium by adding terms that break time reversal symmetry (see, e.g. [10, 11, 46]). We shall briefly recall their definitions before constructing the lowest-order mixed model.

Consider a scalar field $\phi(x,t)$, which can be, say, the rescaled density of bacteria or the composition variable of binary fluid. Model A describes the dynamics of a non-conserved order parameter,

$$\partial_t \phi = -M_{\mathrm{A}} \mu + \sqrt{2\epsilon M_{\mathrm{A}}}\Lambda \tag{2.1}$$

where M_{A} denotes a constant relaxation rate, $\mu(\phi, \nabla\phi, \nabla^2\phi ...)$ is the local chemical potential associated with the process, ϵ governs the noise strength and Λ is a spatio-temporal white noise of unit variance: $\langle \Lambda(\boldsymbol{x},t)\Lambda(\boldsymbol{y},s)\rangle = \delta(\boldsymbol{x}-\boldsymbol{y})\delta(t-s)$. If μ can be written as the derivative $\delta\mathcal{F}/\delta\phi$ of some functional $\mathcal{F}[\phi]$, the steady state solution obeys the Boltzmann distribution, with $\mathcal{F}$ playing the role of the free energy and ϵ the temperature. (A square-gradient, ϕ^4 theory form for $\mathcal{F}$ is traditionally selected, but we defer making this choice until later.)

Model B is defined similarly but for a conserved order parameter, whose amount in any region $\mathcal{V}$, $\int_{\mathcal{V}} \mathrm{d}\boldsymbol{x}\, \phi(\boldsymbol{x},t)$, only changes by virtue of a current $\boldsymbol{J}$ across the surface of that region:

$$\begin{aligned} \partial_t \phi &= -\boldsymbol{\nabla}\cdot\boldsymbol{J} \\ \boldsymbol{J} &= -M_{\mathrm{B}}\boldsymbol{\nabla}\mu + \sqrt{2\epsilon M_{\mathrm{B}}}\boldsymbol{\Lambda} \end{aligned} \tag{2.2}$$

The first of these is the continuity equation enforcing the conservation law, and the second is a constitutive equation describing the transport current from high to low chemical potential, with M_{B} a constant mobility. Again ϵ governs the the noise strength and $\boldsymbol{\Lambda}$ is a vector of uncorrelated unit white noises (each with the statistics of Λ above).

In our mixed systems, both conservative and non-conservative mechanisms are present.

Our Model AB therefore takes the form

$$\begin{aligned} \partial_t \phi &= -\boldsymbol{\nabla} \cdot \boldsymbol{J} - M_{\mathrm{A}} \mu_{\mathrm{A}} + \sqrt{2\epsilon M_{\mathrm{A}}} \Lambda_{\mathrm{A}} \\ \boldsymbol{J} &= -M_{\mathrm{B}} \boldsymbol{\nabla} \mu_{\mathrm{B}} + \sqrt{2\epsilon M_{\mathrm{B}}} \boldsymbol{\Lambda}_{\mathrm{B}} \end{aligned} \tag{2.3}$$

As noted previously, the two chemical potentials $\mu_{\mathrm{A,B}}(\phi, \nabla\phi, \nabla^2\phi ...)$ are not generically functional derivatives of free energies $\mathcal{F}_{\mathrm{A,B}}$ in systems far from equilibrium. For simplicity we shall assume that they are, but we allow that $\mathcal{F}_{\mathrm{A}} \neq \mathcal{F}_{\mathrm{B}}$. This is enough to break time-reversal symmetry, and generically does so at lower order in (∇, ϕ) than the terms needed to break the symmetry in either sector by itself. The latter begin with contributions of order (∇^2, ϕ^2) to the chemical potentials [46] (and for Model B also include a contribution to $\boldsymbol{J}$ that is not the gradient of any local chemical potential [11, 32]). Note also that once $\mathcal{F}_{\mathrm{A}} \neq \mathcal{F}_{\mathrm{B}}$, unequal noise levels in the two sectors can be absorbed by rescaling either free energy, allowing us to set both noises to a common value ϵ in (2.3).

In the next two sections, we first derive a general condition on $\mu_{\mathrm{A,B}}$ under which, despite the fact that $\mathcal{F}_{\mathrm{A}} \neq \mathcal{F}_{\mathrm{B}}$, an exact formal equivalence exists to a Hohenberg-Halperin-type model with a more complicated mobility operator and a single free energy $\mathcal{F}$. After this, we specialise to the particular forms for μ_{A} and μ_{B} that complete the specification of our canonical model.

2.2 A special case: Accidental restoration of time-reversal symmetry for ϕ field

In general, the model defined by (2.3) is out of equilibrium, but under certain conditions on μ_{B} and μ_{A}, time-reversal symmetry is restored, in the sense that the steady-state probability of observing a field trajectory $\phi(\boldsymbol{x}, t)$ is the same as the probability of the time-reversed trajectory. Note however that the separate contributions to the dynamics are not the same in forward and backward paths: in particular the conservative currents have a nonzero average spatial pattern in the microphase-separated steady state, and this current pattern reverses sign under time reversal. This was reported for a more specific model in [44], whereby a pattern of dense and dilute bacterial domains emerges in which particles are born in the dilute regions, then move by phase separation into the dense ones, where they die off (figure 2.1). The same physics applies here, so that time-reversal symmetry is restored only for the ϕ field and not for the full dynamics [32]. However, this is enough to allow the stationary measure for ϕ to be constructed as the Boltzmann distribution of an effective free energy $\mathcal{F}$. Although not solved exactly, the resulting equilibrium theory is already well studied in the context of microphase separation and its behaviour known to high accuracy [25, 26].

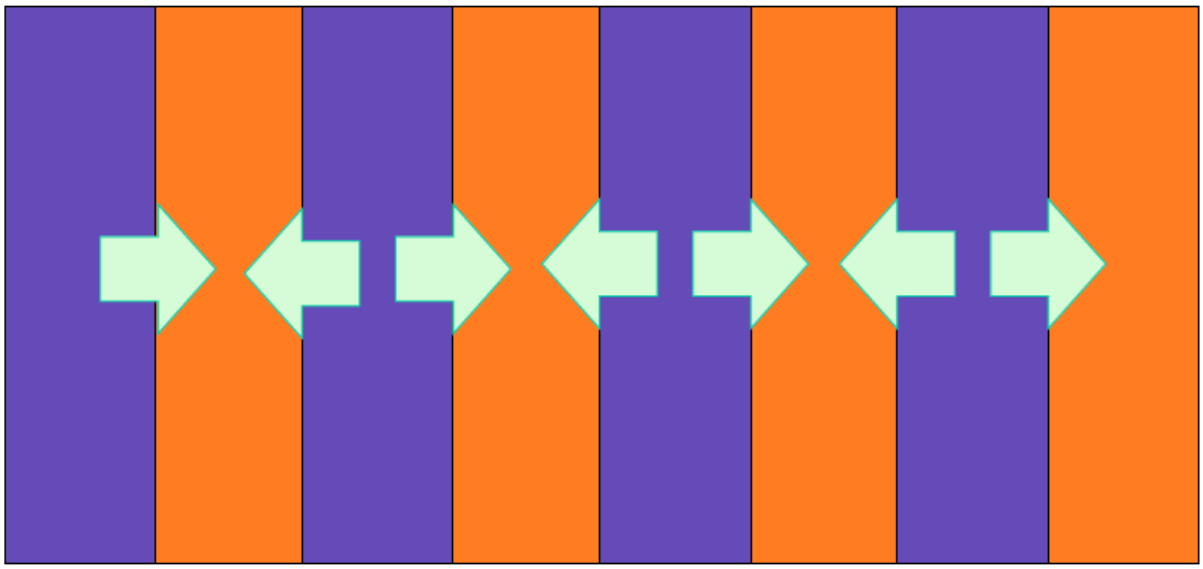

Figure 2.1: Microphase separation in a lamellar phase. On the special parameter subspace the statistics of the ϕ field (orange/purple pattern) are reversible, but there are nonzero mean currents in steady state (arrows). For example in phase-separating bacteria with population dynamics, particles are born in the dilute zones, and diffuse towards the dense ones, where they die [44]. A movie of $\phi(\boldsymbol{x}, t)$ then shows exactly reversible fluctuations whereas the currents are large and irreversible, even at deterministic order.

Let η be the sum of the Model B and Model A noise in equation (2.3): $\eta(\boldsymbol{x}, t) = \sqrt{2\epsilon}\left[-\sqrt{M_\mathrm{B}}\boldsymbol{\nabla}\cdot\boldsymbol{\Lambda}_\mathrm{B}(\boldsymbol{x}, t) + \sqrt{M_\mathrm{A}}\Lambda_\mathrm{A}(\boldsymbol{x}, t)\right]$. Using the addition property of variances for the sum of independent Gaussian distributions,

$$\begin{aligned}\langle\eta(\boldsymbol{x}, t)\eta(\boldsymbol{y}, s)\rangle &= 2\epsilon\left(-M_\mathrm{B}\nabla_x^2 + M_\mathrm{A}\right)\delta(\boldsymbol{x}-\boldsymbol{y})\delta(t-s)\\ &\equiv 2\epsilon K(\boldsymbol{x}-\boldsymbol{y})\delta(t-s)\end{aligned} \tag{2.4}$$

where we have formally introduced a spatial noise kernel $K(\boldsymbol{x})$. Next define a vector operator $\boldsymbol{B}_i(\boldsymbol{x}) = \sqrt{M_\mathrm{B}}\partial_{x_i} + \sqrt{M_\mathrm{A}}$ such that[1] $K(\boldsymbol{x}) = \boldsymbol{B}_i(\boldsymbol{x})\boldsymbol{B}_i^\dagger(\boldsymbol{x})$. With the above operators, we can cast equation (2.3) in a form that closely mimics the relaxational models in [21],

$$\begin{aligned}\partial_t\phi &= \boldsymbol{B}\cdot\left[-\boldsymbol{B}^\dagger\mu + \sqrt{2\epsilon}\boldsymbol{\Lambda}\right]\\ \mu &= \mu_\mathrm{B} + M_\mathrm{A}K^{-1}(\mu_\mathrm{A} - \mu_\mathrm{B})\\ \langle\Lambda_i(\boldsymbol{x}, t)\Lambda_j(\boldsymbol{y}, s)\rangle &= \delta_{ij}\delta(\boldsymbol{x}-\boldsymbol{y})\delta(t-s)\end{aligned} \tag{2.5}$$

If there exists a $\mathcal{F}[\phi]$ that has the given μ as its functional derivative, the steady state probabilities will follow the Boltzmann distribution with $\mathcal{F}$ as the free energy, and detailed

[1]Here $\dagger$ denotes conjugation of the operator. Let f, g be functions that the operator O acts on, $O^\dagger$ is defined as $\int \mathrm{d}\boldsymbol{x} f(Og) = \int \mathrm{d}\boldsymbol{x}(O^\dagger f)g$. For example $\boldsymbol{\nabla}^\dagger = -\boldsymbol{\nabla}$.

balance will be restored. As μ_B is already the functional derivative of $\mathcal{F}_\mathrm{B}$, this requires $K^{-1}(\mu_\mathrm{A}-\mu_\mathrm{B})$ to be a functional derivative. Here K^{-1} is the integral operator inverse to $K(\boldsymbol{x})$: $K^{-1}\psi(\boldsymbol{x}) = \int \bar{K}(\boldsymbol{x}-\boldsymbol{x'})\psi(\boldsymbol{x'})\mathrm{d}\boldsymbol{x'}$ with $\bar{K}(\boldsymbol{x})$ the back Fourier transform of $1/K(\boldsymbol{q})$. Since in Fourier space $K(\boldsymbol{q}) = M_\mathrm{B}q^2 + M_\mathrm{A}$, this $\bar{K}$ is a screened Coulomb (Yukawa) operator.

The simplest case is of course when $\mu_\mathrm{B} = \mu_\mathrm{A}$; then $\mathcal{F} = \mathcal{F}_\mathrm{B} = \mathcal{F}_\mathrm{A}$, meaning that the demixing and the chemical reactions between the two species are controlled by the same chemical potential. This is the case of full thermodynamic equilibrium, with detailed balance at the $(\phi, \boldsymbol{J})$ level, for instance a binary fluid of two immiscible passive species with a simple conversion reaction between the species [7, 38]. The conserved dynamics drives coarsening of coexisting fluid domains whose phase volumes are, however, not conserved due to the reactions. Ultimately the free energy is minimized by the complete elimination of the phase of higher bulk free energy density (or, for a symmetric system, one or other phase at random) so that no interfaces remain and the system is uniform.

A more general and much more interesting case is when $\mu_\mathrm{A} - \mu_\mathrm{B}$ is linear in ϕ. Define (non-local) linear operator Q such that $K^{-1}(\mu_\mathrm{A}-\mu_\mathrm{B}) = Q\phi$. If Q is symmetric under the exchange of spatial/Fourier arguments, then $\mu = \mu_\mathrm{B} + M_\mathrm{A}Q\phi$ is the functional derivative of $\mathcal{F} = \mathcal{F}_\mathrm{B} + \frac{1}{2}M_\mathrm{A}\int \phi(\boldsymbol{x})Q(\boldsymbol{x}-\boldsymbol{x'})\phi(\boldsymbol{x'})\mathrm{d}\boldsymbol{x}\mathrm{d}\boldsymbol{x'}$. The second term is a nonlocal harmonic contribution whose effects on the Boltzmann distribution are readily explicable within equilibrium statistical physics.

As an example, chosen for its relevance to subsequent sections, we now take both $\mathcal{F}_\mathrm{B}, \mathcal{F}_\mathrm{A}$ to be of ϕ^4 square-gradient form but with different linear coefficients: $\mu_\mathrm{B} = c - \alpha\phi + \beta\phi^3 - \kappa_\mathrm{B}\nabla^2\phi$ and $\mu_\mathrm{A} = c + \alpha'\phi + \beta\phi^3 - \kappa_\mathrm{A}\nabla^2\phi$. Note that we can add a constant to μ_B without changing the equations of motion, hence the c terms in μ_B and μ_A are chosen equal here without loss of generality. We can also set $\kappa_\mathrm{A} = 0$ since in the equations of motion this term is absorbed by a shift in α; hereafter we choose $\kappa_\mathrm{B} = \kappa \equiv \kappa_\mathrm{B} - \kappa_\mathrm{A}$ for this reason. We choose $\alpha > 0$ to drive phase separation, but also choose $\alpha' > 0$. The latter means that the non-conserved dynamics would, by itself, take the system towards a uniform target density ϕ_t which is the unique real root of the cubic equation $c + \alpha'\phi_\mathrm{t} + \beta\phi_\mathrm{t}^3 = 0$. So long as this target density lies within the spinodals (resp., binodals) of the phase separation, the uniform state at ϕ_t is locally (resp., globally) unstable. Steady Boltzmann-like states are guaranteed by the equivalence to an equilibrium system, but these must be nonuniform (figure 2.1).

We then have $\mu_\mathrm{A} - \mu_\mathrm{B} = (\alpha' + \alpha)\phi + \kappa\nabla^2\phi$, and, in Fourier space, with normalisation $f(\boldsymbol{q}) = \int \mathrm{d}\boldsymbol{x} f(\boldsymbol{x}) \exp(-i\boldsymbol{q}\cdot\boldsymbol{x})$ and $|\boldsymbol{q}| = q$, we obtain:

$$\mu(\boldsymbol{q}) = \mu_\mathrm{B}(\boldsymbol{q}) + M_\mathrm{A}\frac{(\alpha'+\alpha) - \kappa q^2}{M_\mathrm{B}q^2 + M_\mathrm{A}}\phi(\boldsymbol{q}) \tag{2.6}$$

Defining $m = \sqrt{M_\mathrm{A}/M_\mathrm{B}}$ and $\alpha_\mathrm{eff} = \alpha + \kappa m^2$, the corresponding free energy is

$$\begin{aligned}\mathcal{F}[\phi] &= \int \mathrm{d}\boldsymbol{x}\left[c\phi - \frac{\alpha_\mathrm{eff}}{2}\phi^2 + \frac{\beta}{4}\phi^4 + \frac{\kappa_\mathrm{B}}{2}|\boldsymbol{\nabla}\phi|^2\right] + \frac{m^2}{2}\left(\alpha' + \alpha_\mathrm{eff}\right)\int \frac{\mathrm{d}\boldsymbol{q}}{(2\pi)^d}\frac{|\phi(\boldsymbol{q})|^2}{q^2+m^2} \\ &= \int \mathrm{d}\boldsymbol{x}\left[c\phi - \frac{\alpha_\mathrm{eff}}{2}\phi^2 + \frac{\beta}{4}\phi^4 + \frac{\kappa_\mathrm{B}}{2}|\boldsymbol{\nabla}\phi|^2\right] \\ &\quad + \frac{m^2}{2}\left(\alpha' + \alpha_\mathrm{eff}\right)\int \phi(\boldsymbol{x})U(|\boldsymbol{x}-\boldsymbol{x'}|)\phi(\boldsymbol{x'})\mathrm{d}\boldsymbol{x}\mathrm{d}\boldsymbol{x'}\end{aligned} \tag{2.7}$$

Here $U(r)$, the D-dimensional inverse Fourier transform of $1/(q^2+m^2)$, represents a long-range repulsive interaction of the scalar field. This is the screened Coulomb potential: $U(r) = (4\pi r)^{-1}\exp(-mr)$ in 3D and $U(r) = (2\pi)^{-1}K_0(mr)$ in 2D, with K_0 the modified Bessel function of the second kind. The latter is logarithmic at short distances and decays as $(8\pi mr)^{-1/2}\exp(-mr)$ at large ones. We will explore the consequences of this long-range free energy at the start of the next chapter.

2.3 Canonical choices of μ_B and μ_A

We now revert to the general case in which μ_B and μ_A do not differ by a constant or terms linear in ϕ. This allows many new forms of physical behaviour to enter, so we need to reduce the parameter space to a manageable size. We therefore choose the 'canonical' forms for the two chemical potentials, by writing down the simplest, leading order terms that gives rise to the physical phenomena we aim to explain.

For the Model B sector, to lowest order in ϕ and $\boldsymbol{\nabla}$, we accordingly write

$$\mu_\mathrm{B}(\phi) = -\alpha\phi + \beta\phi^3 - \kappa\nabla^2\phi \tag{2.8}$$

where α, β, κ are positive constants. This is the functional derivative of the usual ϕ^4 free energy, $\mathcal{F}_\mathrm{B}[\phi] = \int \mathrm{d}\boldsymbol{x}\left[f_\mathrm{B} + \frac{1}{2}\kappa\left|\boldsymbol{\nabla}\phi\right|^2\right]$ where $f_\mathrm{B} \equiv -\frac{1}{2}\alpha\phi^2 + \frac{1}{4}\beta\phi^4$. On its own, the Model B free energy is minimised by bulk phase separation into two phases at the binodals $\pm\phi_\mathrm{B} = \pm\sqrt{\alpha/\beta}$, while the interfacial width, ξ_0, obeys $\xi_0 = \sqrt{2\kappa/\alpha}$ and the interfacial tension is $\sigma = (8\kappa\alpha^3/9b^2)^{1/2}$. Note that a linear term in f_B has no effect, and a cubic one can be absorbed by an additive shift of ϕ. This shift effectively defines ϕ to vanish at the critical point, where f_B is symmetric to quartic order.

In the Model A sector, the lowest order relaxational chemical potential towards a fixed target density ϕ_t is $\mu_\mathrm{A}(\phi) \propto (\phi - \phi_\mathrm{t})$, as used for binary mixtures in [22–24]. Nevertheless, as we will see in section 3.4, limit cycles cannot occur at this order due to the lack of nonlinearity. In order to allow our canonical model to capture these cycles (reported for a

more elaborate model in [45]) we take the next lowest order,

$$\mu_{\rm A}(\phi) = u(\phi - \phi_{\rm a})(\phi - \phi_{\rm t}) \tag{2.9}$$

Without loss of generality, we can assume that $\phi_{\rm a} < \phi_{\rm t}$. The non-conservative dynamics then has two fixed points – one stable fixed point at $\phi_{\rm t}$ and an unstable one at $\phi_{\rm a}$. The latter can be used to encode the lowest physical value that the scalar field ϕ can take; for example, if ϕ is a rescaled density of bacteria, $\phi_{\rm a}$ can be chosen at the zero of the physical density. This reflects the situation in population dynamics where the birth-death process has a finite target density, but if the system makes an excursion to zero population it remains there forever in an absorbing state (hence the subscript 'a'). To faithfully represent this behaviour requires multiplicative (and indeed non-Gaussian) noise [51] whereas in the Hohenberg-Halperin framework one always chooses additive Gaussian noise because of the vast algebraic simplification this provides [21, 52]. In combination with (2.9), this simplification is adequate here, because we are interested in phase separations whose binodals $\pm\phi_{\rm B}$ represent physical densities that are both positive, so that $\phi_{\rm a} < -\phi_{\rm B}$. The absorbing state physics does not then interfere with phase separation in the slow reaction limit (which is our main interest below). Note also that in the special case when $\phi_{\rm a} \ll -\phi_{\rm B}$ (representing a narrow phase separation between two phases of nearly equal density) the reaction rate between the two binodals remains approximately linear in ϕ and we recover the simpler form for $\mu_{\rm A}$ used in [22–24].

By virtue of it being quadratic in ϕ, equation (2.9) admits the lowest order mismatch in chemical potentials of the Model A and Model B sectors that *cannot* be incorporated into the equilibrium mapping of the previous section by judicious matching of higher order (i.e., cubic) terms. As stated in the introduction, it is also of lower order than the leading terms able to break time-reversal symmetry in the Model A and B sectors independently. In several ways, therefore, our choice of $\mu_{\rm A,B}$ offers the leading-order realization of genuinely non-equilibrium dynamics for the ϕ field, in systems of Model AB type. This is why we propose the designation 'canonical' for this choice.

2.4 Microscopic lattice model

While the arguments given above have been made on general grounds, it might help to see one concrete example. We start with a microscopic lattice model for bacteria with self-propulsion, quorum sensing, and birth-death dynamics, and arrive at an approximate stochastic partial differential equation for the physical density ρ by explicit coarse-graining the master equation following [53–55].

Before we construct the lattice model, we will perform the van Kampen system size

expansion [54,55] of the birth-death process in the well mixed limit to illustrate the method. Next, following [53], we propose the hopping rates that give the desired continuum limit for a single Active Brownian particle. Finally, we combine the hopping rates with the birth-death rates and perform a system size expansion on the entire lattice model before taking the continuum limit.

This procedure is similar to the explicit coarse graining presented in the appendix of Grafke et al. [45] with the following key differences: (1) we perform the van Kampen system size expansion before taking the continuum limit and hence arrive at an approximate SPDE rather than the exact path integral with Poisson noise obtained by Grafke et al. ; (2) We take the phenomenological approach of looking at the equivalent lattice process of a single active particle and extracting the lattice hopping rates whereas Grafke et al. represent run-and-tumble particles with left/right-movers and coarse-grained them separately before combining into a single density. The end results are the same, although our treatment of the active diffusion extends more easily to higher dimensions.

2.4.1 Birth-death process in the well mixed limit

The birth-death process can be represented by the following chemical equation with birth rate λ_b and death rate λ_d,

$$A + A \leftrightarrow A \tag{2.10}$$

Physically this corresponds to birth by cell division and death by overcrowding. In the well-mixed limit, we assume that the diffusion of particles is sufficiently fast that the density distribution is always homogeneous. Denoting P_n as the probability of having n particles in the system, the master equation for the evolution of the probabilities is

$$\partial_t P_n = \lambda_\mathrm{b}\left[(n-1)P_{n-1} - nP_n\right] + \frac{\lambda_\mathrm{d}}{N}\left[(n+1)nP_{n+1} - n(n-1)P_n\right] \tag{2.11}$$

where N is an extensive variable characterising the typical number of particles in the system. We divide λ_d by this extensive parameter such that the two rate constants have the same scaling with system size – this will become more obvious once we write down the deterministic rate equation. We can write the master equation in an equivalent form by defining a translation operator $\mathbb{E}(a)$ that acts on any function $f(n)$ as $\mathbb{E}(a)f(n) = f(n+a)$

$$\partial_t P_n = \lambda_\mathrm{b}\left[\mathbb{E}(-1) - 1\right] nP_n + (\lambda_\mathrm{d}/N)\left[\mathbb{E}(1) - 1\right] n(n-1)P_n \tag{2.12}$$

To make connection with macroscopic quantities, we change variable to a new scaled density $\rho = n/N$. The probabilities in terms of ρ evolves as follows,

$$\partial_t P(\rho,t) = N\lambda_\mathrm{b}\left[\mathbb{E}(-1/N) - 1\right]\rho P(\rho,t) + N\lambda_\mathrm{d}\left[\mathbb{E}(1/N) - 1\right]\rho\left(\rho - \frac{1}{N}\right)P(\rho,t) \tag{2.13}$$

Recall from quantum mechanics that the momentum operator is the generator of spatial translation. We can define a similar conjugate operator here as $\hat{\rho} = -i\partial_\rho$ after taking ρ to be continuous[2]. Then the translation operator $\mathbb{E}(a) = e^{i\hat{\rho}a} = 1 + a\partial_\rho + \frac{a^2}{2}\partial_\rho^2 \dots$ Now treating $1/N$ as small, we can expand the exponentials. This is the Kramers-Moyal expansion [54,55]. To second order, the master equation becomes a Fokker-Planck equation,

$$\partial_t P(\rho,t) = -i\hat{\rho}(\lambda_\mathrm{b}\rho - \lambda_\mathrm{d}\rho(\rho - 1/N))P - \frac{\hat{\rho}^2}{2N}(\lambda_\mathrm{b}\rho + \lambda_\mathrm{d}\rho(\rho - 1/N))P + O(\hat{\rho}^3 N^{-2}P) \quad (2.14)$$

Note we cannot say that this Fokker-Planck equation is accurate to $O(N^{-2})$ without knowing the shape of $P(\rho,t)$. For example, if $P(\rho,t)$ is a Gaussian distribution with width $\approx 1/\sqrt{N}$, $\hat{\rho}P \approx \sqrt{N}P$ and $\hat{\rho}^2 P \approx P/N$. However, we can self-consistently perform a perturbative expansion of $P(\rho,t)$ by assuming that $P(\rho,t)$ is Gaussian and justify *a posteriori*. This yields the van Kampen system size expansion $\rho = \rho_0(t) + \rho_1(t)/\sqrt{N}$, with $\rho_0(t)$ as the deterministic trajectory and $\rho_1(t)$ the lowest order variation,

$$\begin{aligned} \dot{\rho_0} &= \lambda_\mathrm{b}\rho_0 - \lambda_\mathrm{d}\rho_0^2 \\ \partial_t P(\rho_1,t) &= -i(\lambda_\mathrm{b}\rho_0 - 2\lambda_\mathrm{d}\rho_0^2)\hat{\rho}_1\rho_1 P + \frac{1}{2}(\lambda_\mathrm{b}\rho_0 + \lambda_\mathrm{d}\rho_0^2)\hat{\rho}_1^2 P \end{aligned}$$

where, as before, $\hat{\rho}_1 = -i\partial_{\rho_1}$ is the conjugate momentum of ρ_1. If we wish to know higher order variations we would need to do the Kramers-Moyal expansion to higher order and perform the perturbative calculation order by order. Note that the first order van Kampen system size expansion is equivalent to the first order low noise expansion in $\sqrt{1/N}$ of the Itô stochastic differential equation,

$$\partial_t \rho = \lambda_\mathrm{b}\rho - \lambda_\mathrm{d}\rho^2 + \sqrt{(\lambda_\mathrm{b}\rho + \lambda_\mathrm{d}\rho^2)/N}\Lambda \quad (2.15)$$

where Λ is a white noise.

2.4.2 Active Particles

The next ingredient in the construction of a lattice representation of the full model is finding the hopping rates that yield the desired self-propulsion dynamics of the active particles. We start with the Itô Langevin equation of Active Brownian particles [56]

$$\dot{\boldsymbol{r}} = (\boldsymbol{V} + \boldsymbol{\nabla}D) + \sqrt{2D}\boldsymbol{\Lambda} \quad (2.16)$$

[2]In [53], they have the conjugate variable $\hat{n} = i\hat{\rho}$ and explicitly integrate over imaginary $\hat{n}$ in the path integral.

where $\boldsymbol{V} = -\tau v_0 \boldsymbol{\nabla} v_0/d$, $D = \tau v_0^2/d$, $v_0(r)$ is the swim speed, τ is the tumbling time and d is the dimension of the system. Define $\mu = \log v_0$ such that $D\boldsymbol{\nabla}\mu = \boldsymbol{V} + \boldsymbol{\nabla} D$. We will next show that the above SDE is equivalent to the lattice diffusion model with diffusion rate $\omega_{ij} = \frac{D_i}{a^2} \exp\left(-\frac{f_{ij}}{2}\right)$ where $f_{ij} = -(\mu_j - \mu_i)/a$ is the force vector from site i to site j and a is the lattice spacing.

The master equation in 1D is

$$\partial_t P_i = \omega_{i+1,i} P_{i+1} + \omega_{i-1,i} P_{i-1} - \left(\omega_{i,i+1} + \omega_{i,i-1}\right) P_i \tag{2.17}$$

Let $x = an$. Using the translation operator $E(1) = \exp(iap)$ where $p = -i\partial_x$, we can write the master equation as

$$\begin{aligned}
\partial_t P_x &= \left(e^{iap} - 1\right) \omega_{x,x-a} P_x + (e^{-iap} - 1)\omega_{x,x+a} P_x \\
&= \left[\left(iap - \frac{a^2}{2}p^2 + O(a^3)\right)\omega_{x,x-a} + \left(-iap - \frac{a^2}{2}p^2 + O(a^3)\right)\omega_{x,x+1}\right] P_x \\
&= \left[-iap\left(\omega_{x,x+a} - \omega_{x,x-a}\right) - \frac{a^2}{2}p^2\left(\omega_{x,x+a} + \omega_{x,x-a}\right) + O(a)\right] P_x
\end{aligned}$$

Now we compute the symmetric and antisymmetric parts of the diffusion rates:

$$\begin{aligned}
w_{x,x+a} - w_{x,x-a} &= \frac{D_x}{2a^2}(f_{x,x-a} - f_{x,x+a}) = -\frac{D_x}{a}\partial_x \mu_x + O(a^0) \\
w_{x,x+a} + w_{x,x-a} &= \frac{2D_x}{a^2} + O(a^0)
\end{aligned} \tag{2.18}$$

Collecting the terms and taking $a \to 0$, we obtain

$$\begin{aligned}
\partial_t P &= -\partial_x\left[-(\partial_x \mu) DP - \partial_x(DP)\right] \\
&= -\partial_x\left[fDP - \partial_x(DP)\right]
\end{aligned}$$

This is indeed the Fokker-Planck equation corresponding to the Itô stochastic differential equation of active Brownian particles in equation (2.16).

2.4.3 Minimal model

For multiple particles hopping on a lattice, we use the same hopping rates $\omega_{i,j}$ as found in the previous section, but make v_0 depend on the density and its gradients [56].

$$\begin{aligned}
\partial_t P(\{n_i\}, t) &= \left(\mathcal{L}_{\text{bd}} + \mathcal{L}_{\text{diff}}\right) P(\{n_i\}, t) \\
\mathcal{L}_{\text{bd}} &= \sum_i \lambda_{\text{b}}\left[\mathbb{E}_i(-1) - 1\right] n_i + (\lambda_{\text{d}}/N)\left[\mathbb{E}_i(1) - 1\right] n_i(n_i - 1) \\
\mathcal{L}_{\text{diff}} &= \sum_i \left[\mathbb{E}_i(1)\mathbb{E}_{i-1}(-1) - 1\right]\omega_{i,i-1} n_i + \left[\mathbb{E}_i(-1)\mathbb{E}_{i-1}(1) - 1\right]\omega_{i-1,i} n_{i-1}
\end{aligned} \tag{2.19}$$

Change variable to $\rho_i = n_i/N$ as before, and let $\hat{\rho}_i = -i\partial_{\rho_i}$

$$\begin{aligned}
\mathcal{L}_{\text{diff}} &= \sum_i \left[i(\hat{\rho}_i - \hat{\rho}_{i-1}) - \frac{1}{2N}(\hat{\rho}_i - \hat{\rho}_{i-1})^2 \right] \omega_{i,i-1}\rho_i \\
&\quad + \sum_i \left[-i(\hat{\rho}_i - \hat{\rho}_{i-1}) - \frac{1}{2N}(\hat{\rho}_i - \hat{\rho}_{i-1})^2 \right] \omega_{i-1,i}\rho_{i-1} \\
&= \sum_i i(\hat{\rho}_i - \hat{\rho}_{i-1}) \left(\omega_{i,i-1}\rho_i - \omega_{i-1,i}\rho_{i-1}\right) - \frac{1}{2N}(\hat{\rho}_i - \hat{\rho}_{i-1})^2 \left(\omega_{i,i-1}\rho_i + \omega_{i-1,i}\rho_{i-1}\right)
\end{aligned} \tag{2.20}$$

Using the diffusion rates from before, we have

$$\begin{aligned}
\omega_{i,i-1}\rho_i - \omega_{i-1,i}\rho_{i-1} &= \frac{1}{a}\partial_x(D\rho) + \frac{1}{a}(\partial_x\mu_i)D_i\rho_i + O(a^0) \\
\omega_{i,i-1}\rho_i + \omega_{i-1,i}\rho_{i-1} &= \frac{2}{a^2}D\rho + O(1/a)
\end{aligned} \tag{2.21}$$

Collecting the terms, the Louville operator for the diffusion of active particles is,

$$\begin{aligned}
\mathcal{L}_{\text{diff}} &= \sum_i \frac{i(\hat{\rho}_i - \hat{\rho}_{i-1})}{a} \left[\partial_x(D_i\rho_i) + (\partial_x\mu_i)D_i\rho_i + O(a)\right] \\
&\quad - \sum_i \frac{(\hat{\rho}_i - \hat{\rho}_{i-1})^2}{2Na^2} \left(2D\rho + O(a)\right) \\
&= \sum_i -i\hat{\rho}_i\partial_x \left[\partial_x(D_i\rho_i) + (\partial_x\mu_i)D_i\rho_i + O(a)\right] \\
&\quad - \frac{1}{2N}\sum_{i,j} \hat{\rho}_i\hat{\rho}_j \left[-\partial_x \left(2D\rho + O(a)\right)\partial_x\right]_{ij}
\end{aligned} \tag{2.22}$$

Now we add the birth-death dynamics. Recall from equation (2.14),

$$\mathcal{L}_{\text{bd}} = -\sum_i \left[i\hat{\rho}_i(\lambda_{\text{b}}\rho_i - \lambda_{\text{d}}\rho_i(\rho_i - 1/N)) + \frac{\hat{\rho}_i^2}{2N}(\lambda_{\text{b}}\rho_i + \lambda_{\text{d}}\rho_i(\rho_i - 1/N)) \right] \tag{2.23}$$

As before, we perform a system size expansion, $\rho_i = \rho_i^0 + \sqrt{\epsilon}\rho_i^1$ where $\epsilon = 1/N$. The zeroth order and the first order equation are the same as the low noise expansion of the following SDE

$$\partial_t\rho_i = \lambda_{\text{b}}\rho_i - \lambda_{\text{d}}(\rho_i)^2 + \partial_x \left[\partial_x(D_i\rho_i) + (\partial_x\mu_i)D_i\rho_i + O(a)\right] + \Lambda_i \tag{2.24}$$

where Λ_i is a Gaussian noise with variance

$$\langle \Lambda_i(t)\Lambda_j(s)\rangle = \epsilon\delta(t-t') \left[(-\partial_x 2D\rho\partial_x)_{ij} + \delta_{ij}\left(\lambda_{\text{b}}\rho_i + \lambda_{\text{d}}\rho_i^2\right) + O(a) \right] \tag{2.25}$$

Taking the continuum limit $\rho' = \rho/a, \lambda'_{\mathrm{d}} = a\lambda_{\mathrm{d}}$ (then relabelling back) and $a \to 0$, we find

$$\begin{aligned} \partial_t \rho &= \lambda_{\mathrm{b}}\rho - \lambda_{\mathrm{d}}\rho^2 + \partial_x \left[\partial_x(D\rho) + (\partial_x \mu) D\rho\right] + \Lambda \\ \langle \Lambda(x,t)\Lambda(y,s)\rangle &= \epsilon \left[\partial_x \partial_y 2D\rho + \lambda_{\mathrm{d}}\rho + \lambda_{\mathrm{d}}\rho^2\right] \delta(x-y)\delta(t-s) \end{aligned} \tag{2.26}$$

We can see that we have conservative phase separation with the chemical potential μ as well as non-conservative dynamics. The above equation can be easily generalised to higher dimensions with careful treatment of the lattice diffusion terms [53]. The result is the same as replacing the spatial derivatives with vector gradient operators and taking the appropriate dot products.

Equation (2.26) involves multiplicative noise, rendering analysis of the equation hard in general. We instead perturbatively expand $\rho = \rho_0(1+\phi)$ and only keep the lowest terms in gradients and ϕ for both the conservative and non-conservative part. We obtain, in vector notations,

$$\begin{aligned} \partial_t \phi &= M\nabla^2 \mu - u(\phi+1)(\phi - \phi_{\mathrm{t}}) + \Lambda \\ \mu &= -\alpha\phi + \beta\phi^3 - \kappa\nabla^2\phi \\ \langle \Lambda(\boldsymbol{x},t)\Lambda(\boldsymbol{y},s)\rangle &= \left[-2\epsilon M\nabla_x^2 + \epsilon u(2+\phi_{\mathrm{t}})\right] \delta(\boldsymbol{x}-\boldsymbol{y})\delta(t-s) \end{aligned} \tag{2.27}$$

We can also freely rescale ϕ by any factor to adjust the relative magnitude of α and β (so that we can set the binodal density to 1 later), and after relabelling the parameters, this gives

$$\begin{aligned} \partial_t \phi &= M\nabla^2 \mu - u(\phi-\phi_{\mathrm{a}})(\phi - \phi_{\mathrm{t}}) + \Lambda \\ \mu &= -\alpha\phi + \beta\phi^3 - \kappa\nabla^2\phi \\ \langle \Lambda(\boldsymbol{x},t)\Lambda(\boldsymbol{y},s)\rangle &= \left[-2\epsilon M\nabla_x^2 + \epsilon u(-2\phi_{\mathrm{a}} + \phi_{\mathrm{t}})\right] \delta(\boldsymbol{x}-\boldsymbol{y})\delta(t-s) \end{aligned} \tag{2.28}$$

This is of the form of the canonical model proposed in equation (3.22) with additional relations between the constants.

In such a setting we can, if we wish, relate all the expansion parameters back to microscopic quantities such as the swim speed of the bacteria, and we can indeed see that $\phi = \phi_{\mathrm{a}}$ corresponds to the zero of the physical density ρ. Note that this explicit coarse graining on a specific model yields an additional relation between u, ϕ_{t} and ϕ_{a}: $u = (-\phi_{\mathrm{a}} + \phi_{\mathrm{t}}/2)^{-1}$. For illustrative purposes, we adopt this choice in simulations throughout this chapter.

Finally we may rescale space and other parameters to set $M_{\mathrm{B}} = 1$. Collecting all the

terms, our canonical version of Model AB is therefore

$$\begin{aligned}
\partial_t \phi &= -\boldsymbol{\nabla} \cdot \boldsymbol{J} - M_{\mathrm{A}} \mu_{\mathrm{A}} + \sqrt{2\epsilon M_{\mathrm{A}}} \Lambda_{\mathrm{A}} \\
\boldsymbol{J} &= -\boldsymbol{\nabla} \mu_{\mathrm{B}} + \sqrt{2\epsilon} \boldsymbol{\Lambda}_{\mathrm{B}} \\
\mu_{\mathrm{B}} &= -\alpha \phi + \beta \phi^3 - \kappa \nabla^2 \phi \\
\mu_{\mathrm{A}} &= u(\phi - \phi_{\mathrm{a}})(\phi - \phi_{\mathrm{t}})
\end{aligned} \tag{2.29}$$

These are the equations we will solve time and again in the next chapter where we explore the parameter space of the canonical Model AB.

2.5 Conclusion

In this chapter, we formulated a scalar field theory (Model AB) for non-equilibrium phase-separating systems with chemical reactions. It combines Model B for the conservative dynamics and Model A for the non-conservative reactions, with incompatibility between the free energies that drive each sector.

In general the system is far from equilibrium and no effective global free energy exists, although within a certain subspace of parameters reversibility is recovered at the level of the space-time trajectories of the order parameter ϕ (but not if one also monitors its conservative current $\boldsymbol{J}$). The effect of reactions within this subspace is to introduce repulsive screened Coulomb interactions that frustrate bulk phase separation (as will be discussed in more details in the next chapter). This equilibrium mapping, which is exact where it exists at all, significantly improves upon earlier works that establish a related equivalence to an (unscreened) Coulomb interaction. The latter mapping is not exact because it holds at the level of deterministic mean-field dynamics only.

In order to study the more general case, we constructed a 'canonical' version of Model AB, retaining lowest order terms in the Landau Ginzburg expansion in each sector, plus one additional nonlinearity required to ensure that the global mean density does not dynamically decouple from other degrees of freedom. The canonical Model AB amounts to choosing a symmetric ϕ^4 square-gradient free energy $\mathcal{F}_{\mathrm{B}}$ for the Model B sector and a nonlinear local logistic-growth type chemical potential μ_{A} for the Model A sector. This canonical model is more general than it might at first appear, since parameter shifts can absorb both linear and cubic terms in $\mathcal{F}_{\mathrm{B}}$ and Laplacian terms in μ_{A}. Within the model, each sector remains separately time-reversal symmetric but with incompatible free energies driving their dynamics. (Technically our chosen form of the model has an absorbing state which could break the time reversal symmetry if entered, but we do not work in this region of very low physical density.) We also performed an explicit lattice coarse-graining of Active Brownian particles with birth-death dynamics to show that, though initially

constructed only from symmetries and conservation laws, Model AB can also be arrived at via a bottom-up approach if one wishes to relate the model parameters to real biological systems.

Chapter 3

Phenomenology of Model AB

Materials undergoing both conservative phase separation and chemical reactions form an important class of non-equilibrium systems. In the last chapter, we constructed a canonical scalar field theory to describe such systems, with conserved and non-conserved dynamics obeying Model B and Model A respectively, chosen such that the two free energies involved are incompatible and there is no overall free energy structure.

There have been numerous studies in literature on more complex, micro-inspired models in this class. One common feature is that they all exhibit micro-phase separation, where the domains coarsen (or anti-coarsen) to a finite length scale [7, 22–24, 34–37, 43, 44, 48, 57, 58]. But some more exotic phenomena have also been reported for specific models: in one model of bacteria colonies with birth-death [45], it was found that in some parameter regime, the system undergoes steady state limit cycles between a homogeneous and a phase-separated state; in another model tailored for biomolecular condensates (also known as membraneless organelles), it was observed that one large droplet can spontaneously split into two as a pathway to anti-coarsen towards microphase separation [59].

In the last chapter, we showed that it is possible to find a special subspace of parameters in Model AB in which time-reversal symmetry is accidentally restored for the dynamics of the density (albeit not of the current). In this fine-tuned subspace, we can identify an effective free energy that readily explains the emergence of microphase-separated states, and captures physics that should still apply in neighbouring regions of parameter space. In more distant parameter regions, however, dynamics is seen that is clearly incompatible with any kind of equilibrium model, such as limit cycles that break time reversal symmetry. In this chapter we survey the phenomenology of our canonical model across various regimes, making connections with results already discovered in more specific models within the same general class.

The chapter is organised as follows. In section 3.1, we review the special equilibrium subspace found in the previous chapter and discuss the stationary states found by minimising the associated free energy. Section 3.2 catalogues some stationary solutions of the

dynamics, including lamellar patterns and droplet suspensions, with the key feature that the phase separation is always arrested at a fixed length-scale. Next, in section 3.3, we investigate the droplet splitting transient state via linear stability analysis of the angular Fourier modes of a droplet. In section 3.4 we address steady-state limit cycle solutions. In section 3.5, the results are summarised and compared to more complicated, problem-specific models found in the literature. Most, but not all, of the analytical work reported here is at mean-field level, though most numerical simulations were performed with weak noise. All simulations are obtained via numerical integration using the pseudospectral method: computing derivatives in Fourier space and multiplications in real space [60]. Fourier transforms are implemented using standard fast Fourier transforms (FFTs) and higher frequencies are cut off with 2/3 dealiasing procedure [61]. Time integration is performed using the explicit Euler–Maruyama method [62].

3.1 Microphase separation in the special equilibrium subspace

Starting with the full stochastic equations of Model AB,

$$\begin{aligned} \partial_t \phi &= -\boldsymbol{\nabla}\cdot\boldsymbol{J} - M_{\mathrm{A}}\mu_{\mathrm{A}} + \sqrt{2\epsilon M_{\mathrm{A}}}\Lambda_{\mathrm{A}} \\ \boldsymbol{J} &= -M_{\mathrm{B}}\boldsymbol{\nabla}\mu_{\mathrm{B}} + \sqrt{2\epsilon M_{\mathrm{B}}}\boldsymbol{\Lambda}_{\mathrm{B}} \end{aligned} \tag{3.1}$$

and recalling from section 2.2 that by judiciously choosing the chemical potentials μ_{A} and μ_{B}, we can cast the above equation in a form that closely mimics the Hohenberg-Halperin relaxational models [21] with a free energy that takes the following form,

$$\begin{aligned} \mathcal{F}[\phi] &= \mathcal{F}_{\mathrm{loc}}[\phi] + \mathcal{F}_{\mathrm{nl}}[\phi] \\ \mathcal{F}_{\mathrm{loc}}[\phi] &= \int \mathrm{d}\boldsymbol{x}\left[c\phi - \frac{\alpha_{\mathrm{eff}}}{2}\phi^2 + \frac{\beta}{4}\phi^4 + \frac{\kappa}{2}|\boldsymbol{\nabla}\phi|^2\right] \\ \mathcal{F}_{\mathrm{nl}}[\phi] &= \frac{m^2}{2}\left(\alpha' + \alpha_{\mathrm{eff}}\right)\int \frac{\mathrm{d}\boldsymbol{q}}{(2\pi)^d}\frac{|\phi(\boldsymbol{q})|^2}{q^2+m^2} \end{aligned} \tag{3.2}$$

The local part of the free energy favours phase separation into bulk phases whenever $\alpha_{\mathrm{eff}} > 0$. However the non-local part is repulsive for $\alpha' + \alpha_{\mathrm{eff}} > 0$ and thereby frustrates phase separation. This is particularly easy to comprehend in the unscreened limit (recovered as $m^2 \to 0$ at constant $m^2\alpha' \equiv \alpha''$) where the Coulomb cost of a bulk phase separation of oppositely charged species grows faster than the system volume V, and so cannot be overcome by any local contribution to $\mathcal{F}$. At small scales however, the local terms still dominate, creating coexisting phases which must therefore organize themselves into a microphase separated pattern on some finite length scale.

The unscreened limit of our mapping is closely related to one studied previously for deterministic models of similar physical content (e.g., [48]). In this limit, it might appear that the steady-state density $\bar{\phi}$ of any uniform state must vanish, so as to avoid an otherwise divergent contribution $V^2\alpha''\bar{\phi}^2/2$ from the long-ranged interaction in equation (3.2). However, this conclusion is invalidated by the fact that uniform states form a null space of the purely conservative dynamics (with noise kernel $K(\boldsymbol{q}) = M_{\rm B}q^2$) that prevails in the same limit. The physically correct outcome is instead found by retaining nonzero m, for which the nonlocal term in (3.2) remains extensive, and equates to $V(\alpha' + \alpha_{\rm eff})/2$. Thus for homogeneous states, the free energy per unit volume, $f = \mathcal{F}/V$, becomes

$$f(\bar{\phi}) = c\bar{\phi} + \frac{\alpha'}{2}\bar{\phi}^2 + \frac{\beta}{4}\bar{\phi}^4 \tag{3.3}$$

Hence for the uniform state, minimizing our $\mathcal{F}$ recovers the Model A target density, $\bar{\phi} = \phi_{\rm t}$. This is inevitable, because, as stated above, uniform states have no Model B dynamics.

Next we consider fluctuations about such a uniform state: $\phi(\boldsymbol{x}) = \phi_{\rm t} + \delta\phi(\boldsymbol{x})$ for which we have

$$\begin{aligned} F[\phi] = f(\phi_{\rm t}) &+ \frac{1}{2}\int \frac{{\rm d}\boldsymbol{q}}{(2\pi)^d}\left[-\alpha_{\rm eff} + 3\beta\phi_{\rm t}^2 + \kappa q^2 + \frac{\alpha' + \alpha_{\rm eff}}{m^{-2}q^2 + 1}\right]|\delta\phi(\boldsymbol{q})|^2 \\ &+ \frac{\beta}{4}\int {\rm d}\boldsymbol{x}\ \left(\delta\phi^4 + 4\phi_{\rm t}\delta\phi^3\right) \end{aligned} \tag{3.4}$$

For $(\alpha - 3\beta\phi_{\rm t}^2)^2 \leq 4\kappa m^2(\alpha' + 3\beta\phi_{\rm t}^2)$, the coefficient of the quadratic term is non-negative for all k, and the homogeneous state is locally stable. Equality gives the onset threshold (or spinodal) of microphase-separated patterning at the mean field level.

However, it is well known that for the equilibrium microphase separation transition, fluctuations can alter the phase boundaries, and generically drive the transition first order by suppressing the spinodal instability [63]. Depending on whether c is identically zero, one either get lamellar patterns or droplet suspensions. For simplicity we will work through both cases assuming that reactions are much slower than the conservative dynamics ($4\kappa m^2\alpha' \ll \alpha^2$) so that the interfacial widths are small compared to the domain size. As a rule of thumb, we enforce the smallest domain to be at least $10\xi_0$ for all numerical evaluations where $\xi_0 = \sqrt{2\kappa/\alpha}$ is the interfacial width.

3.1.1 Lamellar patterns

Tarzia et al. have presented a comprehensive study of the case with $c = 0$ (which also implies $\phi_{\rm t} = 0$) using the Brazovskii (Hartree) approximation [25, 26]. They found a first order phase transition from the uniform state to the lamellar phase as the noise strength decreases. The lamellar patterns have a domain length $L \propto (\sqrt{\kappa^{-1}(\alpha' + \alpha) + m^2} - m)^{-1/2}m^{-1/2}$ close

to the transition[1]. Further away from the transition, the Hartree approximation no longer applies as the interfaces sharpen. Here it is more appropriate to substitute a pseudo-1D square wave ansatz, similar to the approach in [57].

We assume a quasi-1D ansatz $\phi(x) = \phi_2 - (\phi_1 - \phi_2)H(x - \zeta L/2) + (\phi_1 - \phi_2)H(x + \zeta L/2)$ for $x \in [-L/2, L/2]$ where $H(x)$ is the Heaviside step function for all free energy calculations except the κ-term, where we approximate the interfaces as tanh-shaped curves connecting the two domains. ζ is the ratio taken up by the ϕ_1 phase in a period of length L. Note that ζ is a function of (ϕ_1, ϕ_2), fixed by the constraint that the total amount of reaction must sum to zero.

First we will calculate the additional free energy contribution of each interface [57]. As the interface is narrow compared to the domain length, they can be approximate with $(\phi_1 + \phi_2)/2 + (\phi_1 - \phi_2)\tanh(x/\xi_0)/2$ where $\xi_0 = \sqrt{2\kappa/\alpha}$ is the interfacial width [47],

$$\int_{-\infty}^{\infty} \mathrm{d}x\ \kappa \left[\frac{\phi_1 - \phi_2}{2}\partial_x \tanh(x/\xi_0)\right]^2 = \sqrt{\frac{\alpha\kappa}{18}}(\phi_1 - \phi_2)^2 \tag{3.5}$$

Together with the contributions from the bulk, the local part of the free energy gives a contribution per unit volume of,

$$V^{-1}\mathcal{F}_{\mathrm{loc}} = f_{\mathrm{loc}}(\phi_1)\zeta + f_{\mathrm{loc}}(\phi_2)(1 - \zeta) + \frac{2}{L}\sqrt{\frac{\alpha\kappa}{18}}(\phi_1 - \phi_2)^2 \tag{3.6}$$

For the non-local part, let $\Psi(q) = \frac{m^2}{2}(\alpha' + \alpha_{\mathrm{eff}})(q^2 + m^2)^{-1}\phi(q)$, and $\Psi(x)$ be its Fourier transform, so that $\mathcal{F}_{\mathrm{nl}} = \int \mathrm{d}x \Psi(x)\phi(x)$. $\Psi(x)$ obeys the differential equation,

$$\left(-\partial_x^2 + m^2\right)\Psi(x) = \frac{m^2}{2}(\alpha' + \alpha_{\mathrm{eff}})\phi(x) \tag{3.7}$$

Substituting in for $\phi(x)$ and enforcing continuity of $\Psi(x), \partial_x\Psi$ at the boundaries, we obtain, up to an additive constant,

$$\Psi(x) = \frac{1}{2}(\alpha' + \alpha_{\mathrm{eff}}) \begin{cases} a\cosh(mx) + \phi_1 & \text{for } |x| \le \zeta L/2 \\ b\cosh(m(x - L/2)) + \phi_2 & \text{for } \zeta L/2 < |x| < L/2 \end{cases} \tag{3.8}$$

where, in this section, we define $z = mL/2$ and

$$\begin{aligned} a &= \frac{(-\phi_1 + \phi_2)\,\mathrm{sech}(z\zeta)}{1 + \coth(z(1 - \zeta))\tanh(z\zeta)} \\ b &= \frac{(\phi_1 - \phi_2)\,\mathrm{sech}(z(1 - \zeta))}{1 + \coth(z\zeta)\tanh(z(1 - \zeta))} \end{aligned} \tag{3.9}$$

[1]The uniform state is identified as paramagnetic in these papers, whereas the ferromagnetic phase occurs for $\alpha + \alpha' < 0$, corresponding to when the Model A sector also prefers phase separation. This requires bistable chemical reactions, which goes beyond the simple class we are interested in here.

Integrating $\Psi(x)\phi(x)$, we obtain the non-local part of free energy density,

$$\begin{aligned} V^{-1}\mathcal{F}_{\text{nl}} = &\frac{1}{2}(\alpha' + \alpha_{\text{eff}})\phi_1 \left(\zeta\phi_1 - (\phi_1 - \phi_2)\frac{\sinh(z(1-\zeta))\sinh(z\zeta)}{z\sinh(z)}\right) \\ &+ \frac{1}{2}(\alpha' + \alpha_{\text{eff}})\phi_2 \left((1-\zeta)\phi_2 + (\phi_1 - \phi_2)\frac{\sinh(z\zeta)\sinh(z(1-\zeta))}{z\sinh(z)}\right) \end{aligned} \tag{3.10}$$

The total free energy density $V^{-1}\mathcal{F}$ for a lamellar pattern is plotted against L in figure 3.2a, where there is a clear minimum at a finite value of L, implying that the periodicity of the pattern is finite. One can then minimise the free energy by differentiating with respect to (L, ϕ_1, ϕ_2), although the resulting systems of equations are not particularly enlightening or analytically tractable, so we will turn to numerical evaluations instead. However, when m is sufficiently small, we can expand the non-local part as a power series in $z = mL/2$, and check for self-consistency,

$$V^{-1}\mathcal{F}_{\text{nl}} \approx \frac{1}{2}(\alpha' + \alpha_{\text{eff}})\left[\left(\zeta\phi_1^2 + (1-\zeta)^2\phi_2^2\right) + \frac{1}{3}(\phi_1 - \phi_2)^2\zeta^2(1-\zeta)^2z^2 + O(z^4)\right] \tag{3.11}$$

This gives a simpler expression for the total free energy density

$$V^{-1}\mathcal{F}(\phi_1, \phi_2, L) = f(\phi_1, \phi_2) + (\phi_1 - \phi_2)^2\left[\sqrt{\frac{2\alpha\kappa}{9}}L^{-1} + \frac{m^2(\alpha' + \alpha_{\text{eff}})}{24}\zeta^2(1-\zeta^2)L^2\right] \tag{3.12}$$

Minimising with respect to L gives the length-scale of the lamellar pattern: $L \propto m^{-2/3}(\alpha' + \alpha + \kappa m^2)^{-1/3}(\alpha\kappa)^{1/6}$. A sufficient condition for self-consistency is $m^2\kappa \ll \alpha$ (i.e. the reaction rate is slow compared to diffusion) and the expression further simplifies to $L \propto m^{-2/3}$.

The typical shape of the f against L curve is shown in figure 3.2a: for small L the interfacial cost is the main contribution whereas for large L the non-local screened Coulomb eventually dominates. In the limit where the reaction rates are small ($m^2 \ll \kappa^{-1}(\alpha + \alpha')$), the pattern length obeys $L \propto m^{-2/3}$ for the square wave ansatz which applies further away from the transition, compared to $L \propto m^{-1/2}$ close to the transition. Interestingly, this outcome is consistent with the results in [57] (see also [24]) even though their models do not live in a parameter subspace where an equilibrium mapping holds.

3.1.2 Droplet suspension in 2D

Assume $c \leq 0$ without loss of generality, and postulate spherical droplets at density ϕ_1 with radius R on a square or hexagonal lattice with spacing L in a bath of density ϕ_2. The scalar field ϕ is, up to an additive constant to obtain the correct spatial average, a convolution of a disk function $\phi_{\text{disk}}(\boldsymbol{x}) = (\phi_1 - \phi_2)\,(1 - H(|\boldsymbol{x}| - R))$, where H is the same step function as before, and a Dirac comb function at the lattice points. Hence we can

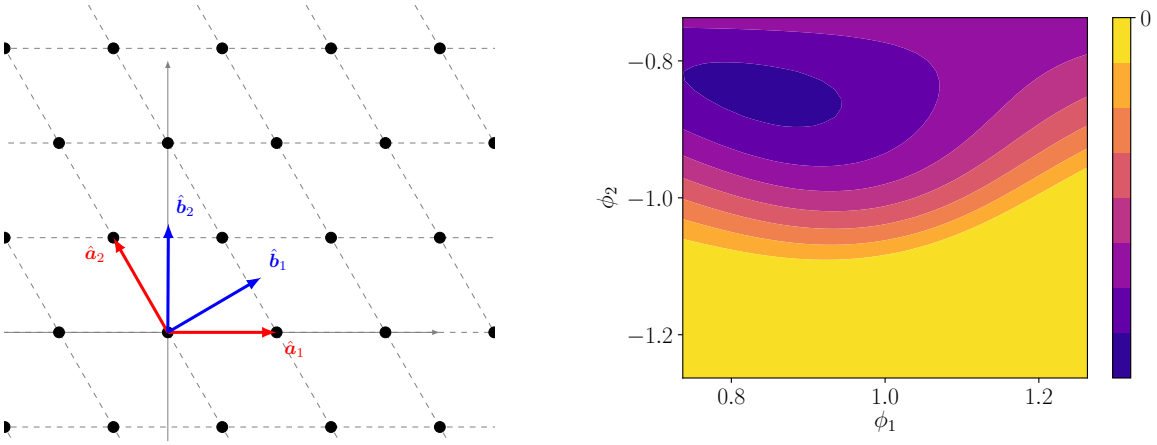

(a) (b)

Figure 3.1: (a) shows the unit vectors of a hexagonal lattice in real and Fourier space. (b)shows a colormap of the partially minimised free energy for each value of (ϕ_1, ϕ_2) to find the global minimum for a hexagonal lattice of droplets.

Fourier transform both functions and multiply in Fourier space using the Convolution Theorem. In 2D the Fourier transform of a disk of height $(\phi_1 - \phi_2)$ is

$$\phi_{\text{disk}}(\boldsymbol{k}) = (\phi_1 - \phi_2)\frac{2\pi R}{|\boldsymbol{k}|}J_1(|\boldsymbol{k}|R) \tag{3.13}$$

where J_1 is the Bessel function of the first kind. A square or hexagonal lattice with unit vectors $(\hat{\boldsymbol{a}}_1, \hat{\boldsymbol{a}}_2)$ and spacing L can be represented the Dirac comb function $\sum_{n_1,n_2}\delta(\boldsymbol{x} - L(n_1\hat{\boldsymbol{a}}_1 + n_2\hat{\boldsymbol{a}}_2))$. Its Fourier transform is the following sum,

$$\phi_{\text{latt}}(\boldsymbol{k}) = \sum_{n_1,n_2}\exp[-i(n_1\boldsymbol{k}\cdot\hat{\boldsymbol{a}}_1 + n_2\boldsymbol{k}\cdot\hat{\boldsymbol{a}}_2)] \tag{3.14}$$

We can choose unit vectors $\hat{\boldsymbol{b}}_1, \hat{\boldsymbol{b}}_2$ such that they are respectively orthogonal to $\hat{\boldsymbol{a}}_2, \hat{\boldsymbol{a}}_1$ as shown in figure (3.1a) for a hexagonal lattice. In this basis, letting $\boldsymbol{k} = k_1\hat{\boldsymbol{b}}_1 + k_2\hat{\boldsymbol{b}}_2$, the above sum factorises to

$$\phi_{\text{latt}}(\boldsymbol{k}) = \sum_{n_1}\exp\Big(-ik_1n_1L\hat{\boldsymbol{a}}_1\cdot\hat{\boldsymbol{b}}_1\Big)\sum_{n_2}\exp\Big(-ik_2n_2L\hat{\boldsymbol{a}}_2\cdot\hat{\boldsymbol{b}}_2\Big) \tag{3.15}$$

Note that $\hat{\boldsymbol{a}}_1\cdot\hat{\boldsymbol{b}}_1 = \hat{\boldsymbol{a}}_2\cdot\hat{\boldsymbol{b}}_2 \equiv s$, say. The Fourier series identity gives

$$\phi_{\text{latt}}(\boldsymbol{k}) = \Delta_k^2\sum_{n_1,n_2}\delta(k_1 - n_1\Delta_k)\delta(k_2 - n_2\Delta_k) \tag{3.16}$$

where $\Delta_k = 2\pi/(sL)$ is the lattice spacing in reciprocal space. Using the Convolution Theorem, the Fourier transform of the scalar field is,

$$\phi(\boldsymbol{k}) = (\phi_1 - \phi_2)2\pi R\Delta_k^2 \frac{J_1(|\boldsymbol{k}|R)}{|\boldsymbol{k}|} \sum_{n_1,n_2} \delta(k_1 - n_1\Delta_k)\delta(k_2 - n_2\Delta_k) + (2\pi)^2\phi_2\delta^2(\boldsymbol{k}) \quad (3.17)$$

where the last term gives the density ϕ_2 of the continuous phase. Note that due to the orthogonality relations, we also have $\hat{\boldsymbol{a}}_1 \cdot \hat{\boldsymbol{a}}_2 = \hat{\boldsymbol{b}}_1 \cdot \hat{\boldsymbol{b}}_2 = \sqrt{1-s^2}$. Hence the volume element $\mathrm{d}k_x\mathrm{d}k_y = s\,\mathrm{d}k_1\mathrm{d}k_2$, and the non-local part of the free energy density is (noting that $[2\pi\delta(0)]^d = V$),

$$\begin{aligned} V^{-1}\mathcal{F}_{\mathrm{nl}} &= \frac{1}{2}(\alpha' + \alpha_{\mathrm{eff}}) \left[\frac{s^2m^2R^2\Delta_k^4}{(2\pi)^2}(\phi_1 - \phi_2)^2 \sum_{k_1,k_2} \frac{J_1^2(kR)}{k^2(m^2+k^2)} + \phi_2^2 \right] \\ &= \frac{1}{2}(\alpha' + \alpha_{\mathrm{eff}}) \left[\left(\frac{mR}{\Delta_k L}\right)^2 (\phi_1 - \phi_2)^2 \sum_{n_1,n_2} \frac{J_1(Rn\Delta_k)^2}{n^2\left(m^2\Delta_k^{-2} + n^2\right)} + \phi_2^2 \right] \end{aligned} \quad (3.18)$$

where $k = \left(k_1^2 + k_2^2 + \sqrt{1-s^2}k_1k_2\right)^{1/2}$, $n = \left(n_1^2 + n_2^2 + \sqrt{1-s^2}n_1n_2\right)^{1/2}$. The local ($\phi^4$) part of the free energy can be calculated as for the $c = 0$ case,

$$V^{-1}\mathcal{F}_{\mathrm{loc}} = f_{\mathrm{loc}}(\phi_1)\frac{\pi R^2}{sL^2} + f_{\mathrm{loc}}(\phi_2)\left(1 - \frac{\pi R^2}{sL^2}\right) + \sqrt{\frac{\alpha\kappa}{18}}(\phi_1 - \phi_2)^2\frac{2\pi}{sL}\frac{R}{L} \quad (3.19)$$

where f_{loc} is the local free energy. We can see that there are four parameters: $\phi_1, \phi_2, L, R/L$. However since the total amount of reaction must sum to zero in equilibrium, $R/L \equiv \zeta$ is a function of ϕ_1, ϕ_2. We will also write $m/\Delta_k \equiv \chi$. The non-local part simplifies,

$$V^{-1}\mathcal{F}_{\mathrm{nl}} = \frac{1}{2}(\alpha' + \alpha_{\mathrm{eff}}) \left[\chi^2\zeta^2 (\phi_1 - \phi_2)^2 \sum_{n_x,n_y} \frac{J_1(\frac{2\pi}{s}\zeta|n|)^2}{|n|^2(\chi^2 + |n|^2)} + \phi_2^2 \right] \quad (3.20)$$

So does the local part of the free energy

$$V^{-1}\mathcal{F}_{\mathrm{loc}} = f_{\mathrm{loc}}(\phi_1)\frac{\pi}{s}\zeta^2 + f_{\mathrm{loc}}(\phi_2)\left(1 - \frac{\pi}{s}\zeta^2\right) + \sqrt{\frac{2\alpha\kappa}{9}}(\phi_1 - \phi_2)^2\frac{\pi\zeta}{sL} \quad (3.21)$$

The total free energy for a square lattice ($s = 1$) and a hexagonal lattice ($s = \sqrt{3}/2$) with the same (ϕ_1, ϕ_2) are shown in figure 3.2a and we can indeed see that the minimum of the free energy occurs at a finite length, where the long range screened Coulomb interaction dominates the short range interactions. This minimum for a hexagonal lattice is then plotted in figure 3.1b for various values of (ϕ_1, ϕ_2).

Further minimisation over ϕ_1, ϕ_2 yields the global minimum for each lattice type, which can be compared against the minimum free energies for lamellar patterns and the

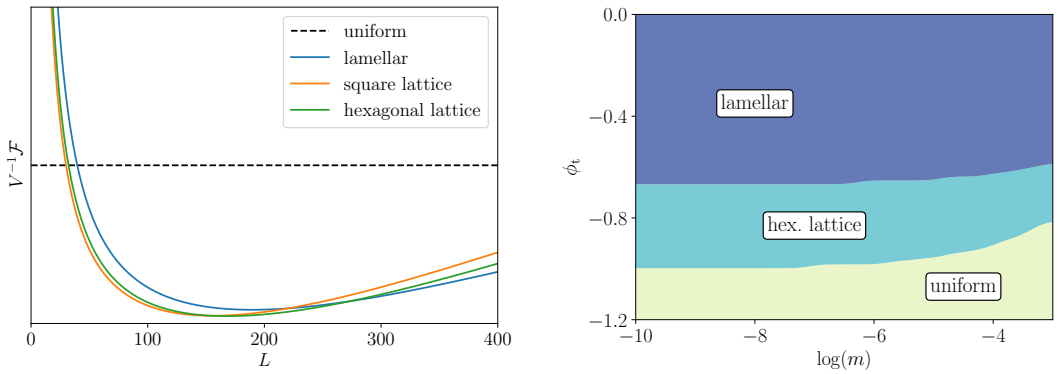

(a) (b)

Figure 3.2: (a) shows a plot of the total free energy density against the pattern length L for the uniform state at ϕ_t and square and hexagonal lattices of droplets, all at $(\phi_1, \phi_2) = (0.86, -0.86)$. (b) is an equilibrium phase diagram in the $(\log(m), \phi_t)$ plane showing the regions where the free energy is minimised by the uniform state, lamellar patterns and hexagonal droplet lattices. The square lattice phase is never the global minimizer for the range of parameters considered here.

uniform state to obtain the phase diagram in figure 3.2b, which is the major result of this section. There are other possible candidates for the stationary pattern, but the literature on microphase separations [63] suggest that lamellar patterns and droplet suspensions are the only two found in 2D, though in 3D more exotic patterns exist, composed of structural motifs including bilayers, Y-junction cylinders, cylindrical micelles and spherical micelles [64].

This equilibrium subspace is special in allowing us to use equilibrium precepts to quantify the microphase-separated structure; nevertheless, we expect it to remain generic in terms of the patterns that emerge. Model parameters that are near, but not on, this subspace should therefore give qualitatively similar patterning, but they will also have steady-state entropy production [32], at the level of the ϕ dynamics, that is absent in the subspace itself. However, if one chooses to track the Model A and Model B sectors separately, as will be explored in chapter 5, the new steady-state entropy production is generically swamped by the contribution from steady-state currents, which remain large in the equilibrium limit (figure 2.1). This adds further support to our view that the qualitative behaviour in our ϕ-reversible subspace is not exceptional, but shared by neighbouring parameter values.

3.2 Generic microphase separation

To explore regimes away far from the equilibrium subspace, we focus instead on the canonical choices of $\mu_{\mathrm{A}}, \mu_{\mathrm{B}}$ proposed in section 2.3,

$$\begin{aligned} \partial_t \phi &= -\boldsymbol{\nabla} \cdot \boldsymbol{J} - M_{\mathrm{A}} \mu_{\mathrm{A}} + \sqrt{2\epsilon M_{\mathrm{A}}} \Lambda_{\mathrm{A}} \\ \boldsymbol{J} &= -\boldsymbol{\nabla} \mu_{\mathrm{B}} + \sqrt{2\epsilon} \boldsymbol{\Lambda}_{\mathrm{B}} \\ \mu_{\mathrm{B}} &= -\alpha\phi + \beta\phi^3 - \kappa \nabla^2 \phi \\ \mu_{\mathrm{A}} &= u(\phi - \phi_{\mathrm{a}})(\phi - \phi_{\mathrm{t}}) \end{aligned} \tag{3.22}$$

Consider a system with target density ϕ_{t} and a very small reaction coefficient uM_{A}. This is the only uniform density sustainable by the Model A dynamics, but if it lies between the spinodals $\pm\phi_{\mathrm{S}} = \pm\sqrt{\alpha/3\beta}$ of $\mathcal{F}_{\mathrm{B}}$ (meaning $d^2 f_{\mathrm{B}}/d\phi^2 < 0$), the uniform state at ϕ_{t} is unstable. Full bulk phase separation is then not possible in an infinite system. The phase separation is arrested at a fixed length scale, set by a balance between the flux across the interfaces and the reaction rates within the two phases. According to the equilibrium mapping of section 3.1 above, the same scenario also holds outside the spinodal but within the binodals: $|\phi_{\mathrm{t}}| < \phi_{\mathrm{B}}$. Roughly speaking, matter is created in the dilute regions ($\phi < 0$), pumped across the phase boundary by the Model B dynamics, and eventually destroyed in the dense regions ($\phi > 0$), see figure 2.1. Qualitatively the above reasoning still holds for finite rather than very small uM_{A}, although the binodals and spinodals do then vary with uM_{A} (see section 3.2.2 below).

Some typical steady state patterns found numerically are shown in figure 3.3. For ϕ_{t} close to zero, the system shows lamellar patterns similar to those obtained in [22–24]. Otherwise, we either see either a droplet phase (disconnected regions of $\phi > 0$) or its inverse, a bubble phase, depending on which binodal ϕ_{t} is closer to. This echoes the findings in [59] for a related model. Some of these steady states are reached via spinodal decomposition, others via nucleation and growth. We start by considering the linear stability of the only viable uniform state at ϕ_{t} in section 3.2.1, followed by an analysis of the pattern close to the onset of the instability using the amplitude equation in section 3.2.1.1. For parameter regimes far away from the instability threshold, we expect lamellar patterns if $\phi_{\mathrm{t}} = 0$ and droplet suspensions otherwise. For $\phi_{\mathrm{t}} = 0$, the length of the lamellar pattern is probed with numerical simulations in section 3.2.1.2. To make analytical progress on droplet suspensions, we first consider a single dense droplet in a dilute bath in section 3.2.2.1 and subsequently add complexity by allowing multiple droplets in section 3.2.2.2.

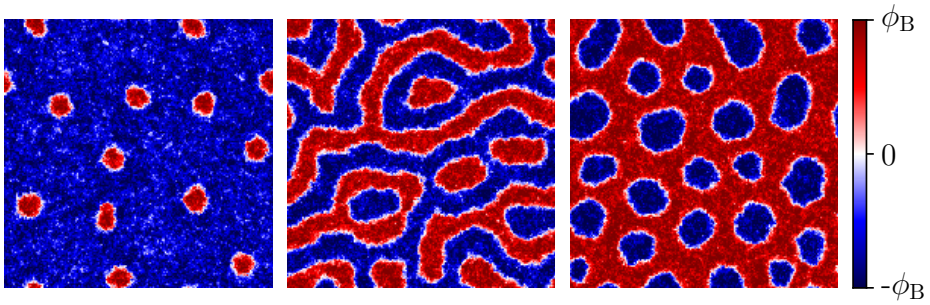

Figure 3.3: Patterns observed for $\phi_t = -0.6, 0, 0.3$. The left panel shows a dilute suspension of droplets nucleated out of the uniform phase. The other two panels show stripe and bubble patterns that appears via spinodal decomposition. The remaining parameters are $\alpha = \beta = 0.2, \kappa = 1, uM_\Lambda = 5 \times 10^{-5}, \phi_a = -10, \epsilon = 0.1$.

3.2.1 Spinodal decomposition

We consider a small perturbation about the uniform target state,

$$\phi(x) = \phi_t + (2\pi)^{-d} \int \mathrm{d}\boldsymbol{q} \delta\phi(\boldsymbol{q}) \exp(-i\boldsymbol{q} \cdot \boldsymbol{x}) \tag{3.23}$$

and expand the deterministic part of equations (3.22) to linear order:

$$\begin{aligned} \partial_t \delta\phi(\boldsymbol{q}) &= (\tilde{\alpha} q^2 - \kappa q^4 - \tilde{u}) \delta\phi(\boldsymbol{q}) \\ &\equiv \sigma(q) \delta\phi(\boldsymbol{q}) \end{aligned} \tag{3.24}$$

where $\tilde{\alpha} = \alpha - 3\beta\phi_t^2$, $\tilde{u} = M_\Lambda u(-\phi_a + \phi_t)$ and we have defined the linear growth rate

$$\sigma(q) = \left[\left(\frac{\tilde{\alpha}^2}{4\kappa} - \tilde{u} \right) - \kappa(q^2 - q_c^2)^2 \right] \tag{3.25}$$

where $q_c = \sqrt{\tilde{\alpha}(2\kappa)^{-1}}$. Linear stability analysis tells us that the homogeneous state is unstable when two conditions are met: (i) $\tilde{\alpha} > 0$ so that ϕ_t lies between the spinodals of $\mathcal{F}_B$; and (ii) $\tilde{\alpha}^2/4\kappa > \tilde{u}$, so that the diffusive phase-separating dynamics is strong enough to overcome the non-conservative relaxation towards a uniform density.

3.2.1.1 Near the threshold: Amplitude equation.

We define $\Delta = \tilde{\alpha}^2(4\kappa\tilde{u})^{-1} - 1$ as a measure of the distance to the onset of the patterning instability. Also setting $\tau = 1/\tilde{u}$, $\xi = (\kappa/\tilde{u})^{1/4}$, we can rewrite the growth rate for each Fourier mode as

$$\sigma(q) = \frac{1}{\tau} \left[\Delta - \xi^4 (q^2 - q_c^2)^2 \right] \tag{3.26}$$

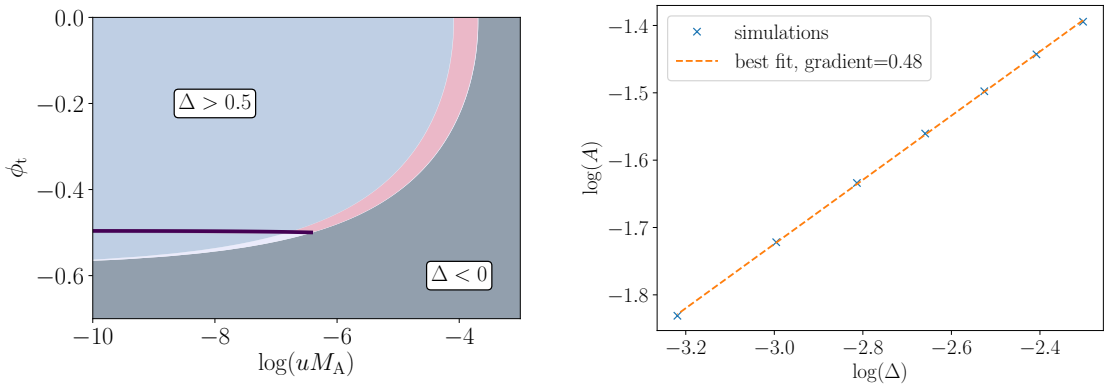

(a) (b)

Figure 3.4: (a) The pink region, enclosed by the $\Delta = 0$ and $\Delta = 0.5$ contours and the dark purple line, above which the expansion is self-consistent (see section 3.2.1.1), indicates where the amplitude equation solution applies. (b) Log-log plot of the amplitude against Δ. The simulations fall closely onto a straight line and the best fit gradient is close to 1/2, as predicted by the amplitude equation.

The amplitude equation is a self-consistent expansion in the small parameter Δ [65, 66]. Starting with the deterministic part of the full equation (3.22) and the growth rate of the linear terms (3.26), we will split the equation into linear and nonlinear parts. Note that we can still rescale both time and space as we have assumed the noise to be small and only work with the deterministic part: $t' = t/\tau$, $x' = x/\xi$ using τ, ξ defined in equation (3.26). For convenience we will also relabel $\delta\phi \to \phi$,

$$\partial_t \phi = -\left[\nabla^2 + \lambda^2\right]^2 \phi + \Delta\phi + \delta_1 \nabla^2 \phi^2 + \delta_2 \nabla^2 \phi^3 - \delta_3 \phi^2 \tag{3.27}$$

where $\lambda = q_c \xi$, $\delta_1 = 3\beta\phi_t \tau \xi^{-2}$, $\delta_2 = \beta\tau\xi^{-2}$ and $\delta_3 = M_A u \tau$.

Close to the threshold (Δ small), the band of unstable modes is narrowly centred at λ, leading to a sinusoidal pattern at wavelength $\approx 1/\lambda$ with its amplitude modulated on a much larger length scale. According to linear stability analysis, the width of the band of growing modes roughly scales as $\Delta^{1/2}$ so we expect the length scale of the slow spatial modulation to scale like $\Delta^{-1/2}$. Similarly, the growth rate scales as Δ, implying that the characteristic time scale of growth is proportional to Δ^{-1}. We will now separate the two scales by defining the slow variables $\boldsymbol{X} = \boldsymbol{x}\Delta^{1/2}, T = t\Delta$ relative to the fast variables $\boldsymbol{x}, t$, and expanding ϕ perturbatively in powers of $\Delta^{1/2}$ to match the spatial and temporal scaling,

$$\phi(\boldsymbol{X}, T, \boldsymbol{x}, t) = \Delta^{1/2}\phi_0 + \Delta\phi_1 + \Delta^{3/2}\phi_2 \tag{3.28}$$

By the chain rule, $\partial_t \to \partial_t + \Delta\partial_T$ and $\boldsymbol{\nabla} \to \boldsymbol{\nabla}_x + \Delta^{1/2}\boldsymbol{\nabla}_X$. For convenience, we also define $L_x = \nabla_x^2 + \lambda^2$. In terms of the slow and fast variables, $L_x \to L_x + 2\Delta^{1/2}\boldsymbol{\nabla}_x \cdot \boldsymbol{\nabla}_X + \Delta\nabla_X^2$

and $L_x^2 \to L_x^2 + 4\Delta^{1/2}\boldsymbol{\nabla}_X \cdot \boldsymbol{\nabla}_x L_x + \Delta(2L_x + 4\nabla_x^2)\nabla_X^2$. Now we can write the entire equation in terms of the slow and fast variables. Keeping everything to at most $O\left(\Delta^{3/2}\right)$,

$$\begin{aligned}\Delta\partial_T(\Delta^{1/2}\phi_0) = &- \left[L_x^2 + 4\Delta^{1/2}\boldsymbol{\nabla}_X \cdot \boldsymbol{\nabla}_x L_x + \Delta(2L_x + 4\nabla_x^2)\nabla_X^2\right](\Delta^{1/2}\phi_0 + \Delta\phi_1 + \Delta^{3/2}\phi_2) \\ &+ \Delta^{3/2}\phi_0 \\ &+ \delta_1\left(\nabla_x^2 + 2\Delta^{1/2}\boldsymbol{\nabla}_x \cdot \boldsymbol{\nabla}_X\right)(\Delta^{1/2}\phi_0 + \Delta\phi_1)^2 \\ &+ \delta_2\nabla_x^2(\Delta^{1/2}\phi_0)^3 \\ &- \delta_3(\Delta^{1/2}\phi_0 + \Delta\phi_1)^2 + O(\Delta^2)\end{aligned} \tag{3.29}$$

To order $\Delta^{1/2}$, we get the linear equation at the threshold,

$$(\nabla_x^2 + \lambda^2)\phi_0 = 0 \Rightarrow \phi_0 = A(\boldsymbol{X}, T)\exp(\mathrm{i}\boldsymbol{\lambda} \cdot \boldsymbol{x}) + \text{c.c.} \tag{3.30}$$

where $\boldsymbol{\lambda}$ is a vector with length λ and consistent with the boundary conditions, and c.c. means complex conjugate. Collecting together the $O(\Delta)$ terms of equation (3.29),

$$\begin{aligned}L_x^2\phi_1 &= -4L_x\boldsymbol{\nabla}_x \cdot \boldsymbol{\nabla}_X\phi_0 + \delta_1\nabla_x^2\phi_0^2 - \delta_3\phi_0^2 \\ &= -\left(4\delta_1\lambda^2 + \delta_3\right)A(\boldsymbol{X}, T)^2\exp(2\mathrm{i}\boldsymbol{\lambda} \cdot \boldsymbol{x}) + \text{c.c.}\end{aligned} \tag{3.31}$$

We can substitute in the *lhs* to check that the following is a solution,

$$\phi_1(\boldsymbol{X}, T, \boldsymbol{x}, t) = -\frac{4\delta_1\lambda^2 + \delta_3}{9\lambda^4}A(\boldsymbol{X}, T)^2\exp(2\mathrm{i}\boldsymbol{\lambda} \cdot \boldsymbol{x}) + \text{c.c.} \tag{3.32}$$

To order $\Delta^{3/2}$, the lowest Fourier components are

$$\partial_T\phi_0 = -\left(2L_x + 4\nabla_x^2\right)\nabla_X^2\phi_0 + \phi_0 + 2\delta_1\nabla_x^2(\phi_0\phi_1) + \delta_2\nabla_x^2\phi_0^3 - 2\delta_3\phi_0\phi_1 - L_x^2\phi_2 \tag{3.33}$$

Collecting all the $\exp(\mathrm{i}\boldsymbol{\lambda} \cdot \boldsymbol{x})$ terms and noting that L_x^2 annihilates any such term in ϕ_2, the amplitude equation is

$$\begin{aligned}\partial_T A &= 4\lambda^2\nabla_X^2 A + A - g|A|^2 A, \\ g &= 3\lambda^2\delta_2 - \frac{(2\delta_1\lambda^2 + 2\delta_3)(4\delta_1\lambda^2 + \delta_3)}{9\lambda^4}\end{aligned} \tag{3.34}$$

For self-consistency, we require $g > 0$ so the linear growth is suppressed by higher order terms and the amplitude has a finite stationary value, implying that

$$27\lambda^6\delta_2 > (2\delta_1\lambda^2 + 2\delta_3)(4\delta_1\lambda^2 + \delta_3) \tag{3.35}$$

Recall that $\delta_1 = 3\phi_t\delta_2$ and $\delta_2 = \beta\tau\xi^{-2} > 0$. Substituting $z = 3\lambda^2\delta_2$, we obtain

$$8\phi_t^2 z^2 + (10\phi_t\delta_3 - 9\lambda^4)z + 2\delta_3^2 < 0 \tag{3.36}$$

Note that z is by definition always positive and at $z = 0$ the *lhs* evaluates to $2\delta_3^2 > 0$. Treating $lhs = 0$ as a quadratic equation in z, the *lhs* has negative parts if and only if both roots of the quadratic equation are positive. This requires

$$\begin{aligned} 10\phi_t\delta_3 - 9\lambda^4 &< 0 \\ (10\phi_t\delta_3 - 9\lambda^4)^2 - 64\phi_t^2\delta_3^2 &> 0 \end{aligned} \tag{3.37}$$

Combining the two inequalities yields the first condition,

$$\phi_t\delta_3 < \lambda^4/2 \tag{3.38}$$

Provided that the above is true, the inequality (3.36) holds for $z_- < z < z_+$, where $z_\pm$ are the two roots of the quadratic equation. Writing in terms of $\delta_2 = z/3\lambda^2$, this becomes $\delta_- < \delta_2 < \delta_+$, where

$$\delta_\pm = \frac{-(10\phi_t\delta_3 - 9\lambda^4) \pm \sqrt{(10\phi_t\delta_3 - 9\lambda^4)^2 - 64\phi_t^2\delta_3^2}}{48\lambda^2\phi_t^2} \tag{3.39}$$

To grasp the physical implications, we will look at the simplified case of $\phi_a \gg \phi_B = 1$. The first condition is automatically true, and the second condition reduces to,

$$\delta_2 < \frac{3\lambda^2}{8\phi_t^2} \tag{3.40}$$

Recall $\delta_2 = \beta\tau\xi^{-2}$ and $\lambda^2 = q_c^2\xi^2$, the expression can be written in a rather simple form

$$\phi_t^2 < \frac{3}{25}\phi_B^2 \tag{3.41}$$

where recall ϕ_B is the binodal density defined as $\phi_B = \sqrt{\alpha/\beta}$. This is a more stringent constraint than the spinodal (local instability). Recall that the homogeneous solution is only unstable when $\tilde{\alpha} > 4\kappa\tilde{u}$. So for small $\tilde{u}$, we have a regime where the homogeneous solution is unstable but the scheme cannot be made self-consistent, meaning that the solution is not well modelled by a sine wave with small amplitude around a homogeneous background state of density.

In summary, close to the threshold (Δ small), the growth of the narrow band of linearly unstable modes is saturated by the nonlinear terms, leading to a sinusoidal pattern at q_c with an amplitude $\propto \sqrt{\Delta}$, within a regime of validity in parameter space as shown in

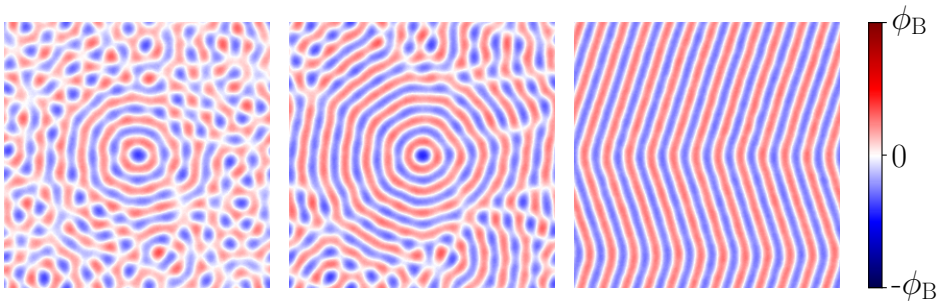

Figure 3.5: Snapshots of the time evolution for $\Delta = 0.1, \epsilon = 1 \times 10^{-4}$ starting with a dense droplet in the middle, showing the gradual alignment of the domains after the initial spinodal decomposition. The bends in the final pattern are due to the extremely low rate of the nucleation of more domains, as would be required to achieve the desired spacing between them. So instead, the domains are bent to have the desired spacing. This undulation of layers whose preferred thickness times their number is less than the width of the sample is called the Helfrich instability (see [67]). For even lower noise magnitudes, the pattern would be effectively arrested at the concentric rings stage (second panel) as the breaking up of rings is also noise-driven. The rest of the parameters are $\alpha = \beta = 0.2$, $\phi_a = -10$, $\phi_t = 0$ and uM_A is fixed by Δ.

figure 3.4. In 1D, this simply gives $\phi(x) \propto \sqrt{\Delta}\sin(q_c x)$. In two dimensions, the pattern selection depends on the initial conditions and the amount of the noise in the simulation, as shown in figure 3.5.

3.2.1.2 Far away from the threshold

As $M_A u$ decreases, the parameter Δ is no longer small and the wavelength of the pattern deviates significantly from the fastest growing mode $2\pi/q_c$. Numerical simulations and theoretical work have been done in 2D by Glotzer et al [22–24]. They found a scaling of $L \sim (M_A u)^{-1/4}$ for relative large $M_A u$ by taking the dimension of the field ϕ to infinity (equivalent to approximating the shape by small sinusoidal perturbations around a homogeneous state), and for $M_A u \to 0$, it was argued that the reactions arrest the coarsening process, leading to $L \sim (M_A u)^{-1/3}$. Curiously, Christensen et al derived the same scaling relations in 2D for the two regimes by substituting in sinusoidal and square wave ansatzes respectively, and minimising an inexactly constructed free energy with respect to the amplitude and the wavelength [57]. While Glotzer's argument for $M_A u \to 0$ depends on the scaling law for the coarsening process and therefore the dimension of the system, Christensen's does not since the pattern is always quasi-1D. Figure 3.6 shows that our simulation results in 1D with finite noise for the domain length L as a function of $M_A u$ (without noise, the steady state depends strongly on initial conditions). For each noise strength, the pattern length obeys a power law close to $L \sim (M_A u)^{-1/4}$ for all regimes of $M_A u$ probed. However, for the smaller values of $M_A u$, we found the patterns to be

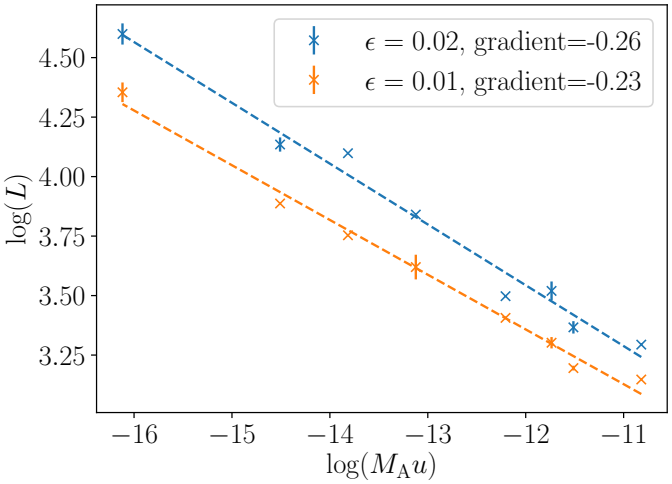

Figure 3.6: Log-log plot of the pattern length L against the birth-death rate $M_A u$ with random initial conditions for $\epsilon = 0.01, 0.02$. The gradients of the best fit lines for both values of ϵ are close to $-1/4$, although the pattern selected depends on the noise magnitude, similar to the case of 2D droplet suspensions in Section 3.2.2.2.

square wave shaped instead of the sinusoidal shape that the $L \sim (M_A u)^{-1/4}$ scaling law of Glotzer et al and Christensen et al is supposed to fit. Thus the origin of the observed power law remains so far unexplained.

3.2.2 Nucleation and arrested growth

Globally, linear stability analysis does not capture the full picture. There is a region in parameter space where although the uniform state at ϕ_t is locally stable, there exists a competing steady state where both phases are present at a ratio that balances the total amount of reactions in the system. In the absence of reactions, $uM_A \to 0$, this is the usual nucleation and growth regime of Model B: $\phi_S < |\phi_t| < \phi_B$. Here droplets nucleate out of the uniform state and, once they are larger than a certain size, they grow by diffusion (and may also coalesce if the volume of the minority phase is not small) until full bulk phase separation has been reached. The diffusive growth process of droplets is commonly known as Ostwald ripening [47, 68–70]; the same scaling laws also control diffusive growth of bicontinuous domains. In our canonical Model AB, we show below that the equivalent of the Ostwald calculation reveals an additional critical radius where the growth stops, arresting the coarsening process at a finite length scale, similar to the findings in Zwicker et al. [58]. Although the kinetics differs, the steady states can again be understood in terms of microphase separation, at least close to the parameter subspace where the exact mapping of section (2.2) holds. (Recall that this mapping shows microphase separation for

ϕ_t in the binodal region.) The deterministic limit of our equations of motion reads (3.22),

$$\begin{aligned} \partial_t \phi &= -\boldsymbol{\nabla} \cdot \boldsymbol{J} + g(\phi) \\ \boldsymbol{J}_1 &= -\boldsymbol{\nabla} \left[-\alpha\phi + \beta\phi^3 - \kappa\nabla^2\phi \right] \\ g(\phi) &= -M_A u(\phi - \phi_a)(\phi - \phi_t) \end{aligned} \tag{3.42}$$

where we have written $-M_A \mu_A(\phi) = g(\phi)$ to save writing later. In the analysis that follows, for tractability we will study dilute phases of well-defined droplets with sharp interfaces, although as we will see later the qualitative observations apply more generally. For definiteness we work in two dimensions but the generalization to 3D is straightforward and should not change qualitative outcomes for droplet suspensions.

3.2.2.1 Single droplet

We first consider a single high-density ($\phi > 0$) droplet of radius $R \gg \xi_0$ in an infinite bath of the dilute ($\phi < 0$) phase. (Recall ξ_0 is the interfacial width in Model B.) Let $\phi_\pm(\boldsymbol{r})$ be the order parameter profile inside and outside the droplet respectively, and define variables $\psi_\pm(\boldsymbol{r})$ as the deviation from the binodal densities:

$$\begin{aligned} \phi_-(\boldsymbol{r}) &= -\phi_B + \psi_-(\boldsymbol{r}) \quad |\boldsymbol{r}| \geq R \\ \phi_+(\boldsymbol{r}) &= \phi_B + \psi_+(\boldsymbol{r}) \qquad 0 \leq |\boldsymbol{r}| < R \end{aligned} \tag{3.43}$$

Outside the droplet, as $r \to \infty$ the gradient terms are negligible and we must have $g(\phi_-) = 0$, implying that $\phi_- \to \phi_t$ at infinity. In contrast to the standard calculation for a purely conserved order parameter [47], the steady-state supersaturation, $\phi(\infty) + \phi_B$, is therefore not dependent on droplet size, but fixed by the non-conserved dynamics. Assuming monotonicity of the deviation ψ_- on physical grounds, we have an upper bound: $\psi_- \leq \phi_t + \phi_B$. Hence for $r \geq R$, expanding equation (3.42) to linear order is a good approximation as long as ϕ_t is close to $-\phi_B$ and $\phi_a \ll -\phi_B$. Inside the droplet, to zeroth order we have $D\nabla^2\psi_+ = g(\phi_B)$ where $D = 2\alpha$, leading to a maximum deviation of approximately $g(\phi_B)R^2/D$. The corresponding fractional deviation is $\psi_+/\phi_B = D^{-1}R^2/(g(\phi_B)^{-1}\phi_B) \equiv \tau_{diff}/\tau_{reac}$ where τ_{diff} represents the time to diffusive across the droplet while τ_{reac} is the time to deplete the dense phase by reaction. Roughly speaking, the dynamics inside the droplet is approximately linear if reaction is much slower than diffusion.

Provided that all the stated conditions hold, the linearised equations can be written down in the following concise form,

$$\begin{aligned} \partial_t \psi_-(\boldsymbol{r}) &= D\nabla^2\psi_- + g_-^0 + g_-^1\psi_- \qquad |\boldsymbol{r}| \geq R \\ \partial_t \psi_+(\boldsymbol{r}) &= D\nabla^2\psi_+ + g_+^0 + g_+^1\psi_+ \qquad 0 \leq |\boldsymbol{r}| < R \end{aligned} \tag{3.44}$$

where as before $D = 2\alpha$ and we have defined $g^0_\pm = g(\pm\phi_\mathrm{B}), g^1_\pm = g'(\pm\phi_\mathrm{B})$ for convenience. The linearised equations need to be solved with the appropriate boundary conditions. At $|\boldsymbol{r}| \to 0$ and $|\boldsymbol{r}| \to \infty$, we only require that $\psi_\pm$ is finite; at the boundary of the droplet, the interfacial tension σ creates a curvature-induced offset $\delta = (d-1)\sigma/(2\phi_\mathrm{B} f''_\mathrm{B}(\phi_\mathrm{B})R)$ to the binodal density [47]. In two dimensions we have

$$\delta = \frac{\gamma}{R}, \quad \gamma = \sqrt{\frac{\kappa}{18\beta}} \tag{3.45}$$

The Ostwald calculation now proceeds along standard lines [47], although non-standard outcomes are expected due to the different boundary conditions at infinity [58]: we fix the droplet radius R, solve for the stationary state of the two linearised equations with $\psi_\pm(R) = \gamma R^{-1}$, then compute the current $J_\pm$ at the droplet interface using the quasi-static solutions, and finally determine the growth rate of the radius R from the mismatch of currents across the interface.

The linearised equations are the modified Helmholtz equations and a spherically symmetric solution in 2D can be written in terms of the modified Bessel functions I_0, K_0. Since $K_0(y) \to \infty$ as $y \to 0$ whereas $I_0(y) \to \infty$ as $y \to \infty$, finiteness of ϕ imposes that the solution must be of the following form,

$$\begin{aligned} \psi_-(\boldsymbol{r}) &= c_- + a_- K_0(k_- r) \qquad |\boldsymbol{r}| \geq R \\ \psi_+(\boldsymbol{r}) &= c_+ + a_+ I_0(k_+ r) \qquad 0 \leq |\boldsymbol{r}| < R \end{aligned} \tag{3.46}$$

where $k_\pm = \sqrt{-g^1_\pm/D}$ and $c_\pm = -g^0_\pm/g^1_\pm \approx \phi_\mathrm{t} \mp \phi_\mathrm{B}$, and $a_\pm$ are constant coefficients whose values can be obtained by matching conditions at the droplet surface where $\psi_\pm = \gamma R^{-1}$:

$$\begin{aligned} a_+ &= (\gamma R^{-1} - c_+)/I_0(k_+ R) \\ a_- &= (\gamma R^{-1} - c_-)/K_0(k_- R) \end{aligned} \tag{3.47}$$

The diffusive currents on both sides of the interface are in the radial direction due to spherical symmetry. Using the properties of the Bessel functions,

$$\begin{aligned} \boldsymbol{J}_+(R) &= -D\boldsymbol{\nabla}\phi_+|_{r=R} = -Dk_+ a_+ I_1(k_+ R)\,\hat{\boldsymbol{r}} \\ \boldsymbol{J}_-(R) &= -D\boldsymbol{\nabla}\phi_-|_{r=R} = Dk_- a_- K_1(k_- R)\,\hat{\boldsymbol{r}} \end{aligned} \tag{3.48}$$

Whenever there is a mismatch of these currents, the interface moves accordingly. Since the interfacial width is small ($R \gg \xi_0$), reactions within the interface are negligible, and

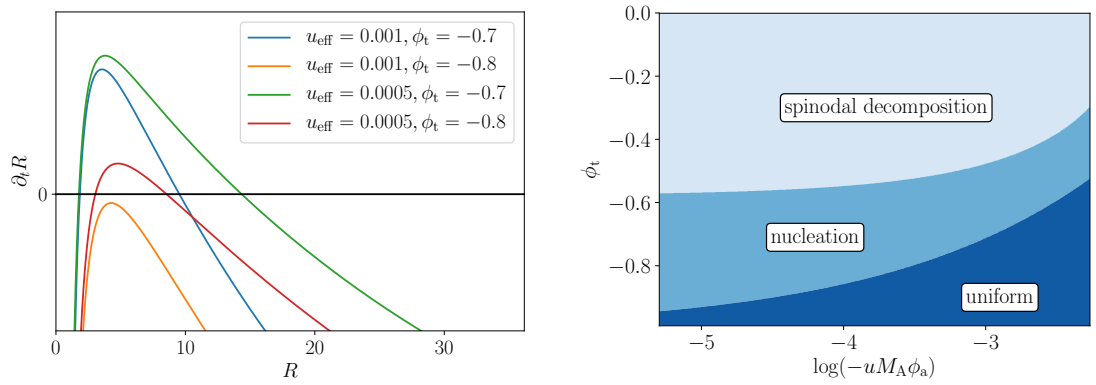

(a) (b)

Figure 3.7: (a) Droplet growth rate $\dot{R}$ against R for four sets of parameters. The orange curve is entirely below the y-axis, indicating that droplets at all radii shrink; the other three curves have two fixed points – the one on the left is the unstable Ostwald radius R_O and the one on the right is the stable droplet radius R_s. (b) Phase diagram in the $(-uM_A\phi_a, \phi_t)$ plane, showing the spinodal decomposition, nucleation and uniform phase. On the far left of the diagram, we have the Model B spinodal and binodal boundaries; these move closer together with increasing reaction rate.

the growth rate of the droplet radius is fixed by the conservative dynamics as

$$\begin{aligned} 2\phi_B \dot{R} &= J_+ - J_- \\ &= D\left[-a_+ k_+ I_1(k_+R) - a_- k_- K_1(k_-R)\right] \\ &= D\left[\left(c_+ - \frac{\gamma}{R}\right) k_+ \frac{I_1(k_+R)}{I_0(k_+R)} + \left(c_- - \frac{\gamma}{R}\right) k_- \frac{K_1(k_-R)}{K_0(k_-R)}\right] \end{aligned} \tag{3.49}$$

We will now disentangle the terms in the above equation. Recall that $c_\pm = -g^0_\pm/g^1_\pm \approx \phi_t \mp \phi_B$, so $c_+ < 0$ and $c_- > 0$. Combined with the fact that modified Bessel functions are positive, we can see that the first term is always negative whereas the second term can be positive. Next, we need to find the relevant parameters. As we can always choose to rescale ϕ, x, t such that $\alpha = \beta = \kappa = 1$, the only three remaining parameters are $M_A u, \phi_t, \phi_a$. We are in the $\phi_a \ll -\phi_B$ regime where the Model A terms can be well approximated by linearity: $\mu_A \approx -M_A u \phi_a(\phi - \phi_t)$. Hence only the combinations $(-M_A u \phi_a)$ and ϕ_t are meaningful.

Roughly speaking, ϕ_t shifts the growth rate curve $\dot{R}(R)$ vertically whereas $(-M_A u \phi_a)$ changes the shape. Growth rate curves for four different sets of parameters are plotted in figure 3.7a. In the absence of reactions $\dot{R}$ is negative at small R, and positive and decaying towards zero at large R, with a single unstable fixed point at a critical radius R_O that depends on supersaturation (see figure 2 (a) of [47]). This scenario gives the familar Ostwald process, whereby large droplets grow at the expense of small ones giving a scaling $R_O \sim (\sigma t/\phi_B^2)^{1/3}$ [47]. A nonzero reaction rate, however small, enforces fixed

supersaturation at infinity such that the largest droplets also shrink, which changes this scenario completely. There are now two distinct cases: (i) the entire curve has negative $\dot{R}$, implying that droplets at all radii shrink and the uniform state is stable; (ii) there is an unstable fixed point at R_{O} as well as a new stable fixed point at a larger radius R_{s}. In the second case, R_{O} is the Ostwald ripening radius; smaller droplets shrink and larger droplets grow, but with the key difference that the growth of these larger droplets stops at the second critical radius R_{s}, similar to findings in [7].

3.2.2.2 Multiple droplets

Typically, within the nucleation and growth regime, multiple droplets are nucleated prior to attaining a steady state. For low phase volumes of the dispersed phase, the existence of neighbouring droplets does not alter the flux pattern close to the interface of each one [68, 69]. However, we do need to account for effect of reactions in distant droplets on the supersaturation at infinity [58].

We consider a system of volume V in 2D with periodic boundary conditions[2]. We continue to assume that $\phi_{\mathrm{a}} \ll -\phi_{\mathrm{B}}$, and consider a target density ϕ_{t} close to (but above) $-\phi_{\mathrm{B}}$ with slow chemical reactions. This ensures (a) that droplets remain dilute because the reaction (the nonconservative part of $\dot{\phi}$) must integrate to zero over the whole volume in any steady state, and (b) that the linear approximation to the reaction rates remains accurate in both the dilute and the dense phase.

Following the usual analysis route for Ostwald problems, we now single out one droplet and treat the rest as a homogeneous background. Let $\lambda = V^{-1}\sum_j \pi R_j^2$ be the area fraction of droplets, and the radius of the singled out droplet be R_i. As before, we denote the density inside and outside the droplet as $\phi_\pm = \pm\phi_{\mathrm{B}} + \psi_\pm$. The approximate linear equation is unchanged in the dense phase, but in the dilute phase, the injection of mass by other droplets plays a role,

$$\partial_t \psi_- = D\nabla^2\psi_- + (1-\lambda)\, g_-^0 + g_-^1\psi_- + V^{-1}\sum_j 2\pi R_j J_-^j \tag{3.50}$$

where J_-^j denotes the current at the surface of the jth droplet. Solving the equation quasi-statically, we obtain a self-consistent equation for the current J_-^i:

$$\begin{aligned} J_-^i &= -D\left(c_-^i - \frac{\gamma}{R_i}\right) k_- \frac{K_1(k_-R_i)}{K_0(k_-R_i)} \\ c_-^i &= c_-(1-\lambda) - (g_-^1 V)^{-1}\sum_j 2\pi R_j J_-^j \end{aligned} \tag{3.51}$$

[2]This choice is made for convenience; the same calculations can be easily repeated with no flux boundary conditions at a distant surface.

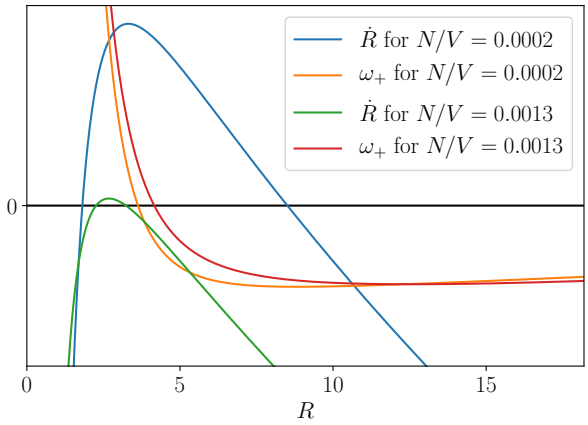

(a)

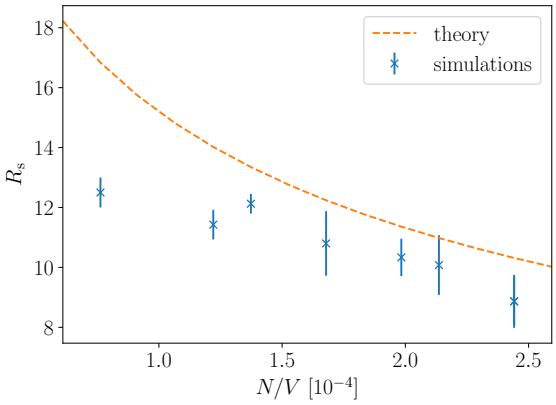

(b)

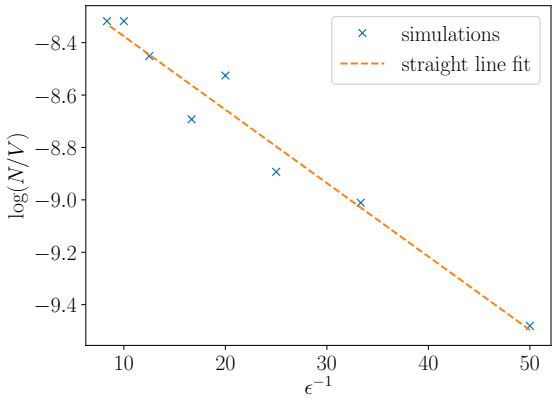

(c)

Figure 3.8: (a) Droplet growth rate $\dot{R}$ and exchange-mode eigenvalue ω_+ plotted against R for two different number densities of droplets in the suspension. The stability of the droplet suspension is indicated by the sign of ω_+ at the stable radius R_s – the second root of the $\partial_t R$ curve. The droplet suspension with $N/V = 0.0013$ is unstable while $N/V = 0.0002$ is stable. (b, c) The stable radius R_s plotted against the N/V and N/V against ϵ for several simulations with the same parameters (except ϵ). Panel (b) shows a reasonable agreement between the theory and the simulations given N/V. Panel (c) indicates that the relation between N/V and ϵ can be approximated using classical nucleation theory.

where $c_- = -g_-^0/g_-^1$ as before, and c_-^i represents the density at infinity as seen by the ith droplet. One solution is for all the droplets to be of the same size. Letting this size be R, the current can be obtained by substituting the second equation into the first

$$J_- = -Dk_- \frac{K_1(k_-R)}{K_0(k_-R)} \left(c_-(1-\lambda) - \frac{\gamma}{R}\right) \left(1 - \frac{2\lambda D k_-}{g_-^1 R}\frac{K_1}{K_0}\right)^{-1} \tag{3.52}$$

Since the equation for ψ_+ is unchanged, we can use the result from equation (3.48) for J_+. The growth rate of the droplet radius then obeys

$$2\phi_{\mathrm{B}}\dot{R} = Dk_+ \frac{I_1}{I_0}\left(c_+ - \frac{\gamma}{R}\right) + Dk_- \frac{K_1}{K_0}\left(c_-(1-\lambda) - \frac{\gamma}{R}\right)\left(1 - \frac{2\lambda D k_-}{g_-^1 R}\frac{K_1}{K_0}\right)^{-1} \tag{3.53}$$

The resulting growth rate $\dot{R}(R)$ curve is plotted in figure 3.8a. We see that the structure of having one unstable fixed point and one stable fixed point remains, but the position of the stable fix point R_{s} shifts to smaller value as the number of droplets increases. Crudely we can understand it in terms of balancing the production of order parameter in the bath (g_-^0) and its consumption in the droplets (g_+^1): the ratio of the volume of the dilute and the dense phase must be around $|g_+^0/g_-^0|$ in steady state.

So far, our calculations suggest that there can be multiple steady states with different numbers of identical droplets as long as the $\dot{R}(R)$ curve has a stable fixed point. However, not all these states are stable against perturbation of the droplet sizes. Consider a perturbation of the form $R_i = R_{\mathrm{s}} + \delta R_i$, where R_{s} is the stationary radius for an N-droplet suspension in volume V, i.e. the stable fixed point of equation (3.53). In addition, let the current on the outside the ith droplet be $J_-^i = J(R_{\mathrm{s}}) + \delta J_-^i$ where δJ_-^i is first order in $\{\delta R_i\}$. Expand equation (3.51) to first order in δR_i,

$$(1+a)\delta J_i + a\sum_{j\neq i}\delta J_j = b\,\delta R_i + c\sum_{j\neq i}\delta R_j \tag{3.54}$$

where in this subsection (only),

$$\begin{aligned}
a &= -\frac{2\lambda D k_-}{N g_-^1 R}\frac{K_1}{K_0} \\
b &= -Dk_-^2\left(1 - \frac{1}{k_-R}\frac{K_1}{K_0} + \frac{K_1^2}{K_0^2}\right)\left[(1-\lambda)c_-^0 - \frac{\gamma}{R} - \frac{2\lambda J}{g_-^1 R}\right] \\
&\quad - Dk_-\frac{K_1}{K_0}\left[\frac{\gamma}{R^2} - \frac{2\lambda}{NR}\left(c_- + \frac{2J}{g_-^1 R}\right)\right] \\
c &= \frac{2\lambda D k_-}{NR}\frac{K_1}{K_0}\left(c_- + \frac{J}{g_-^1 R}\right)
\end{aligned} \tag{3.55}$$

Here $c_- = -g_-^0/g_-^1$ as before, and $c_-^0 = c_-(1-\lambda) - (g_-^1 V)^{-1} N 2\pi R J$ is the density at

infinity seen by the unperturbed droplets (see equation (3.51)). Since equation (3.54) is true for every i, we have N equations with N variables, which can be written in the vector equation form

$$\boldsymbol{M}_1 \delta \boldsymbol{J}_- = \boldsymbol{M}_2 \delta \boldsymbol{R} \tag{3.56}$$

The currents on the inside of the droplets are unaffected by the presence of neighbouring droplets, implying that $\delta \boldsymbol{J}_+ = z\delta \boldsymbol{R}$ where z is obtained by expanding equation (3.48) to first order in $\{\delta R_i\}$,

$$z = Dk_+ \left[k_+ \left(c_+ - \frac{\gamma}{R} \right) \left(1 - \frac{1}{k_+ R} \frac{I_1}{I_0} - \frac{I_1^2}{I_0^2} \right) + \frac{\gamma}{R^2} \frac{I_1}{I_0} \right] \tag{3.57}$$

Putting the currents together for the ith droplet, we can get the growth rate $\partial_t \delta R_i$,

$$\begin{aligned} 2\phi_{\mathrm{B}} \partial_t \delta \boldsymbol{R} &= \delta \boldsymbol{J}_+ - \delta \boldsymbol{J}_- \\ &= \left(z\boldsymbol{I} - \boldsymbol{M}_1^{-1} \boldsymbol{M}_2 \right) \delta \boldsymbol{R} \end{aligned} \tag{3.58}$$

Notice that both $\boldsymbol{M}_1$ and $\boldsymbol{M}_2$ are of a special form: $(\boldsymbol{M}_1)_{ij} = (1+2a)\delta_{ij} - a$ and $(\boldsymbol{M}_2)_{ij} = (b+c)\delta_{ij} - c$. They can be simultaneously diagonalised and the vector equation can be solved separately in the eigen-space of the two matrices. The (unnormalised) eigenvalues are of two types,

$$\begin{aligned} \boldsymbol{v}_1 &= (1, 1, ..., 1) \\ \boldsymbol{v}_2 &= \left(-1, \frac{1}{N-1}, ..., \frac{1}{N-1} \right) \end{aligned} \tag{3.59}$$

The first one is the synchronised growth of all the droplets, and the second one is an exchange of flux: mass flows from one droplet into all the rest. The first eigenmode is always stable provided that the stationary radius exists in the first place – in fact, its eigenvalue is the gradient of the *rhs* of equation (3.53) with respect to R, which is always negative at a stable fixed point. Therefore we are only interested in the second set of eigenvectors. Let

$$\begin{aligned} \delta \boldsymbol{R} &= \delta R \left(-1, \frac{1}{N-1}, ..., \frac{1}{N-1} \right) \\ \delta \boldsymbol{J}_- &= \delta J_- \left(-1, \frac{1}{N-1}, ..., \frac{1}{N-1} \right) \end{aligned} \tag{3.60}$$

We can solve the matrix equation to obtain that

$$\delta J_- = (b-c)\delta R \tag{3.61}$$

Therefore the eigenvalue of the flux exchange mode is found as

$$\begin{aligned} \partial_t \delta R &= \omega_+ \delta R \\ \omega_+ &= (2\phi_{\mathrm{B}})^{-1}(z - b + c) \end{aligned} \tag{3.62}$$

where we recall that b, c are defined in (3.55). The eigenvalue ω_+ is plotted as a function of R along with $\dot{R}$ in figure (3.8a). If the eigenvalue is positive at the stationary radius R_{s}, $\omega_+(R_{\mathrm{s}}) > 0$, the droplet suspension is unstable against flux exchange and the number of droplet decreases as a result. As the number density of droplets increases, the ω_+ curve shifts to the right as the stationary radius R_{s} shifts to the left, giving rise to a maximum density. This provides a more stringent upper bound on the number density of droplets in suspension than simply requiring that (3.53) has a fixed point.

Simulations show that the actual number of droplets per unit volume depends on the noise strength ϵ. Crudely, classical nucleation theory for Model B predicts that the nucleation rate is $\sim \exp(-\Delta F/\epsilon)$ where ΔF represents the free energy barrier. Starting with the uniform state at the target density, once droplets have nucleated, the flux exchange happens on the much slower time-scale of the reactions. Hence a finite number of droplets can nucleate before the suspension stabilises, leading to an inverse relation between the number of droplets and the nucleation rate, $N/V \sim \exp(-\Delta F/\epsilon) \to \log(N/V) = -\Delta F/\epsilon + \text{const}$, as the linear fit in figure 3.8c shows. Once the number of droplets is determined, their common radius is fairly well predicted by our approximate linear theory (see figure 3.8b).

3.3 Droplet splitting

Droplets of sufficiently large radii can become unstable against shape perturbations: they can stretch and subsequently split into two smaller droplets as shown in figure 3.9. To understand this phenomenon, we consider the simple situation of a single circular droplet in an infinite bath and perturb its interface. Then, for perturbed boundary conditions we can solve equations (3.44) for the scalar field inside and outside the droplet as before. Taking the quasi-static limit, we can then compute interfacial fluxes to determine the stability of the circular droplet against perturbations. Our method is inspired by a similar calculation Zwicker et al performed in 3D [59].

Consider small angular perturbations about a circular droplet of radius $\bar{R}$,

$$\begin{aligned} R(\theta) &= \bar{R} + \sum_{l=1}^{\infty} \delta R_l \\ \delta R_l &= \delta R_l^{\mathrm{c}} \cos(l\theta) + \delta R_l^{\mathrm{s}} \sin(l\theta) \end{aligned} \tag{3.63}$$

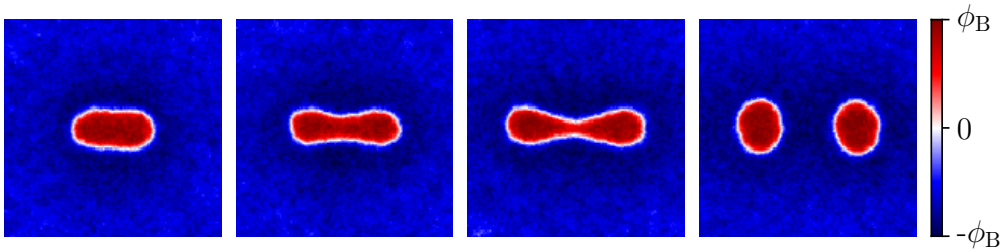

Figure 3.9: Four snapshots of a slightly stretched droplet elongating and splitting into two. The simulation is done with parameters $\phi_t = -0.6, \phi_a = -10, uM_A = 4 \times 10^{-5}, \alpha = \beta = 0.2, \kappa = 1, \epsilon = 0.01$ with periodic boundary conditions.

Note that the $l = 1$ mode corresponds to simple spatial translation. Thus the lowest relevant mode is the $l = 2$ mode, in the shape of a dumbbell. Recall equation (3.44) for $\psi_\pm$ (the excess over the binodal densities: $\phi_\pm = \pm\phi_B + \psi_\pm$)

$$\begin{aligned} \partial_t \psi_+ &= D\nabla^2\psi_+ + g_+^0 + g_+^1\psi_+ \\ \partial_t \psi_- &= D\nabla^2\psi_- + g_-^0 + g_-^1\psi_- \end{aligned} \tag{3.64}$$

The values of $\psi_\pm$ at the interface are set by the local curvature H, which is now modified by the shape distortion,

$$\begin{aligned} \psi_\pm(R(\theta),\theta) &= \gamma H(R(\theta),\theta) \\ &= \frac{\gamma}{\bar{R}}\left[1 + \frac{1}{\bar{R}}\sum_{l=1}^{\infty}(l^2-1)\delta R_l\right] \end{aligned} \tag{3.65}$$

The problem simplifies in polar coordinates because the angular degree of freedom separates from the radial one. Write $\psi_\pm(r,\theta) = \Psi_\pm(r)\Theta_\pm(\theta)$, equation (3.64) reduces to

$$r^2\Psi_\pm''/\Psi_\pm + r\Psi_\pm'/\Psi_\pm + r^2\frac{g_\pm^1}{D} = -\Theta_\pm''/\Theta_\pm \tag{3.66}$$

where prime denotes differentiation with respect to the single argument. Note that all the r-dependence is on the *lhs* while the *rhs* is only a function of θ, hence they must both equal the same constant. Denoting the constant as $l_\pm^2$,

$$\begin{aligned} \Theta_\pm'' &= -l_\pm^2\Theta_\pm \\ r^2\Psi_\pm'' + r\Psi_\pm' - r^2k_\pm^2\Psi_\pm &= l_\pm^2\Psi_\pm \end{aligned} \tag{3.67}$$

where $k_\pm^2 = -g_\pm^1/D$. Solving the eigenvalue equations,

$$\begin{aligned}\Theta_\pm^l(\theta) &= a_l^\pm \cos(l\theta) + b_l^\pm \sin(l\theta)\\ \Psi_\pm^l(r) &= c_l^\pm I_l(k_\pm r) + d_l^\pm K_l(k_\pm r)\end{aligned} \tag{3.68}$$

Periodicity of θ enforces that $l \in \mathbb{N}$, and I_l and K_l are modified Bessel functions. Recall that $I_l(y) \to \infty$ as $y \to 0$ and $K_l(y) \to \infty$ as $y \to \infty$. As a result, the finiteness of $\psi_\pm$ in their respective domains requires that

$$\begin{aligned}\psi_+(r,\theta) &= c_+ + a_0^+ I_0(k_+ r) + \sum_{l=1}^{\infty} I_l(k_+ r)\left(a_l^+ \cos(l\theta) + b_l^+ \sin(l\theta)\right)\\ \psi_-(r,\theta) &= c_- + a_0^- K_0(k_- r) + \sum_{l=1}^{\infty} K_l(k_- r)\left(a_l^+ \cos(l\theta) + b_l^+ \sin(l\theta)\right)\end{aligned} \tag{3.69}$$

The constant term in equation (3.64) fixes $c_\pm = -g_\pm^0/g_\pm^1$. At the interface $R(\theta)$, to first order in δR_l, we have,

$$\begin{aligned}\psi_+(\theta) &= c_+ + a_0^+\left(I_0(k_+\bar{R}) + k_+ I_0'(k_+\bar{R})\sum_{l=1}^{\infty}\delta R_l\right) + \sum_{l=1}^{\infty} I_l(k_+\bar{R})\left(a_l^+\cos(l\theta) + b_l^+\sin(l\theta)\right)\\ \psi_-(\theta) &= c_- + a_0^-\left(K_0(k_-\bar{R}) + k_- K_0'(k_-\bar{R})\sum_{l=1}^{\infty}\delta R_l\right) + \sum_{l=1}^{\infty} K_l(k_-\bar{R})\left(a_l^-\cos(l\theta) + b_l^-\sin(l\theta)\right)\end{aligned} \tag{3.70}$$

After a rather long and tedious calculation, omitted here for brevity, the matching conditions in equation (3.65) yields the following expressions for the coefficients,

$$\begin{aligned}a_0^+ &= \frac{\gamma/\bar{R} - c_+}{I_0(k_+\bar{R})},\ a_0^- = \frac{\gamma/\bar{R} - c_-}{K_0(k_-\bar{R})}\\ a_l^\pm &= \chi_l^\pm \delta R_l^{\mathrm{c}},\ b_l^\pm = \chi_l^\pm \delta R_l^{\mathrm{s}}\\ \chi_l^+ &= \frac{\gamma(l^2-1)/\bar{R}^2 - a_0^+ k_+ I_0'(k_+\bar{R})}{I_l(k_+\bar{R})},\ \chi_l^- = \frac{\gamma(l^2-1)/\bar{R}^2 - a_0^- k_- K_0'(k_-\bar{R})}{K_l(k_-\bar{R})}\end{aligned} \tag{3.71}$$

Collecting the terms together, to $O(\delta R)$, the fields inside and outside the droplet are directly related to the angular perturbations δR_l,

$$\begin{aligned}\psi_+(r,\theta) &= c_+ + a_0^+ I_0(k_+ r) + \sum_{l=1}^{\infty}\chi_l^+ I_l(k_+ r)\delta R_l\\ \psi_-(r,\theta) &= c_- + a_0^- K_0(k_- r) + \sum_{l=1}^{\infty}\chi_l^- K_l(k_- r)\delta R_l\end{aligned} \tag{3.72}$$

Having obtained the quasi-static solutions for any small shape perturbation, we next

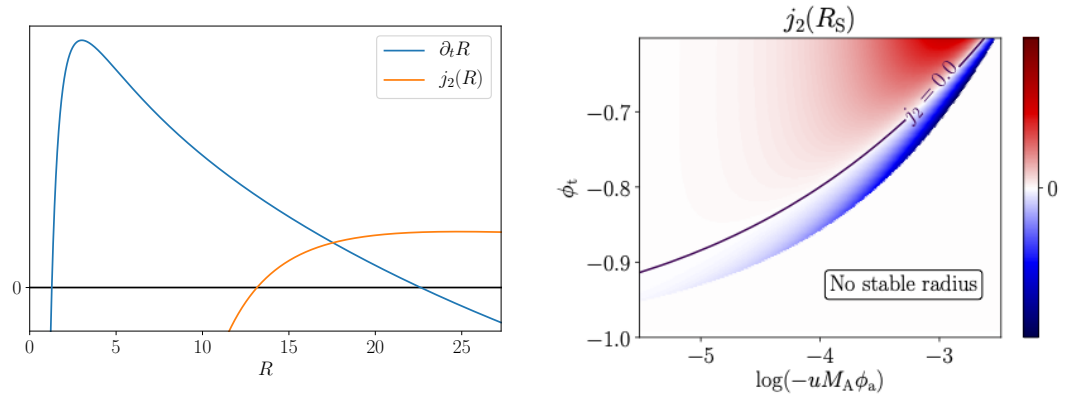

(a) (b)

Figure 3.10: The panel on the left shows the growth rate of a spherical droplet and j_2 for $\phi_t = -0.6, uM_A = 4 \times 10^{-5}$. We can see that j_2 is positive at the stable radius R_s, implying that the circular droplet is unstable against dumbbell-shaped perturbations. The right panel shows the sign of j_2 at the stable droplet radius for a range of ϕ_t and $-uM_A\phi_a$, and the white region on the bottom right corresponds to when no stable droplets can form. The other parameters are $\alpha = \beta = 0.2, \kappa = 1, \phi_a = -10$

calculate the diffusive currents on both sides of the interface to see which direction the interface moves. The difference between the currents can be written as

$$\begin{aligned}\frac{1}{D}\left[\boldsymbol{J}_+(\theta) - \boldsymbol{J}_-(\theta)\right] &= -\boldsymbol{\nabla}\psi_+(R(\theta),\theta) + \boldsymbol{\nabla}\psi_-(R(\theta),\theta) \\ &= j_0(\bar{R})\,\hat{\boldsymbol{r}} + \sum_{l=1}^{\infty}\left[j_l(\bar{R})\delta R_l\,\hat{\boldsymbol{r}} + h_l(\bar{R})(\partial_\theta \delta R_l)\,\hat{\boldsymbol{\theta}}\right]\end{aligned} \tag{3.73}$$

Here $j_0(\bar{R})$ is the isotropic radial flux that controls the growth of a spherical droplet, exactly the same as in section 3.2.2. The remaining two terms give rise to anisotropic flux as a result of the shape perturbation.

To lowest order in δR, the difference between the currents on the two sides of the interface is

$$\begin{aligned}\frac{1}{D}\left[\boldsymbol{J}_+(\theta) - \boldsymbol{J}_-(\theta)\right] &= j_0(\bar{R})\,\hat{\boldsymbol{r}} + \sum_l\left[j_l\left(\bar{R}\right)\delta R_l\,\hat{\boldsymbol{r}} + h_l\left(\bar{R}\right)\left(\partial_\theta \delta R_l\right)\hat{\boldsymbol{\theta}}\right] \\ j_0(\bar{R}) &= -\left(\frac{\gamma}{\bar{R}} - c_+\right)k_+\frac{I_1}{I_0} - \left(\frac{\gamma}{\bar{R}} - c_-\right)k_-\frac{K_1}{K_0} \\ j_l(\bar{R}) &= f'(\bar{R}) - \chi_l^+ k_+ I_l'(k_+\bar{R}) + \chi_l^- k_- K_l'(k_-\bar{R}) \\ h_l(\bar{R}) &= \frac{1}{\bar{R}}\left[-\chi_l^+ I_l(k_+\bar{R}) + \chi_l^- K_l(k_-\bar{R})\right] = \bar{R}^{-1} j(\bar{R})\end{aligned} \tag{3.74}$$

Recall that $j_0(\bar{R})$ governs the growth of the spherical droplet as in section 3.2.2. In addition, the various terms cancel out in such a way that $h_l(\bar{R})$ is proportional to $j_0(\bar{R})$.

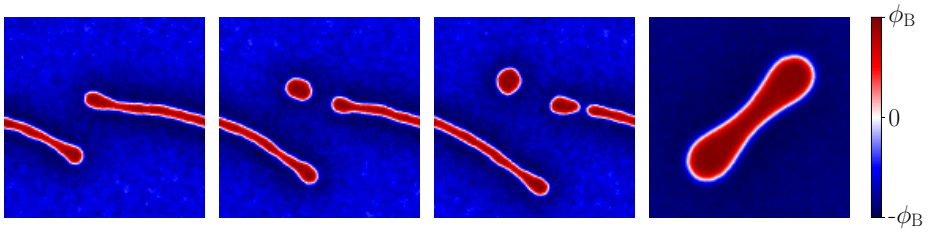

Figure 3.11: The first three panels show another pathway to droplet formation: starting with a single droplet as before, the $l = 2$ mode becomes unstable; as a result, the droplet elongates to form a long stripe whose ends can pinch off to form smaller droplets. Panel 4 shows an arrested dumbbell shape; this shape occurs when ϕ_a is close to $-\phi_B$.

Thus at the stable radius (the stable fixed point of $2\phi_B \partial_t R = j_0(R)$), the only remaining term is $j_l(\bar{R})$ and its sign determines whether the shape is stable: if it is positive, there is a net flow outwards at the protrusion and inwards at the depressions, leading to further deformation of the droplet. Using the properties of Bessel functions $I_l'(z) = I_{l-1}(z) - \frac{l}{z} I_l(z)$, $I_0' = I_1, K_0' = -K_1$, $j_l(\bar{R})$ simplifies to

$$\begin{aligned} j_l = &- k_+^2 \left(\frac{\gamma}{\bar{R}} - a_+\right)\left(1 - \frac{I_1}{k_+ R I_0}\right) - k_-^2 \left(\frac{\gamma}{\bar{R}} - a_-\right)\left(1 - \frac{K_1}{k_- R K_0}\right) \\ &- \left(k_+ \frac{I_{l-1}}{I_l} - \frac{l}{R}\right)\left[\frac{\gamma(l^2-1)}{\bar{R}^2} - \left(\frac{\gamma}{\bar{R}} - a_+\right)\frac{k_+ I_1}{I_0}\right] \\ &+ \left(k_- \frac{K_{l-1}}{K_l} - \frac{l}{R}\right)\left[\frac{\gamma(l^2-1)}{\bar{R}^2} + \left(\frac{\gamma}{\bar{R}} - a_-\right)\frac{k_- K_1}{K_0}\right] \end{aligned} \tag{3.75}$$

As shown in figure 3.10, for a certain range of parameters the $l = 2$ dumbbell mode is linearly unstable, and this stretching is exactly what we see in figure 3.9.

The linear stability analysis tells us whether a shape perturbation will grow, but there are several possibilities of subsequent behaviours following the initial stretch. Figure 3.9 shows the skewed droplet evenly splitting into two round droplets within a relatively confined volume. In a larger volume, the droplet elongates into a long stripe. This is different from the immediate splitting into smaller droplets as was reported for a similar model in 3D [59]. This is because a cylindrical tube in 3D confined by surface tension is unstable against perturbations along the tube, known as the Plateau-Rayleigh instability, whereas such instabilities do not occur in 2D. Instead, the pinching off of smaller droplets at the end of the stripe is induced by noise (figure 3.11). It is also possible to arrest the stretching when the reaction rates are significantly nonlinear in the dilute phase, giving rise to a dumbbell shape as shown in the rightmost panel of figure 3.11.

3.4 Limit cycles

Above we have discussed various forms of arrested phase separation that occur for both linear and quadratic reaction rates. Next we seek to understand a curious non-equilibrium steady state that is specific to nonlinear μ_{A}, comprising limit cycles that oscillate between the homogeneous state and the phase separated state, as shown in figure (3.12a). This behaviour may be particularly relevant in bacteria as it mimics, in simplified form, a biofilm lifecycle where the bacteria alternates between swimming freely in a dilute 'planktonic' phase and forming a condensed, static colony. Ref. [45] reports similar phenomena to those found below, but we will find that the use of our canonical model allows significantly greater progress in understanding the dynamics analytically.

Such limit cycles are found in a region in parameter space where the conservative phase separation is much faster than the reactions, so that u is finite but very small. Let $\varphi(t) = V^{-1} \int \mathrm{d}\boldsymbol{x}\, \phi(\boldsymbol{x}, t)$ be the average order parameter value in the system. In a finite volume V, for each φ, there is at least one stable solution of the Model B dynamics. These form the slow manifold of the Model AB system. In the limit $M_{\mathrm{A}} \to 0$, the reaction terms only move the system along the slow manifold [71]. A sample space-time plot of the ϕ-field in 1D on a domain of spatial extent X is shown in figure (3.12a) and the corresponding circuit in $\dot{\varphi}, \varphi$ shown as a phase-space plot in figure (3.12b). We can see that the full dynamics indeed evolve very close to the slow manifold for the parameters chosen there, verifying the time-scale separation. The phase-space plot shows two key conditions for the limit cycle to occur:

(C1) The rate of change of the global population, $\dot{\varphi}$, must be negative when there is a phase separation and remain so until φ has been driven towards a density where the phase separated state is no longer locally stable. This leads to the turning point around $\varphi = -0.8$.

(C2) $\dot{\varphi}$ must be positive for the uniform state (the upper branch of figure (3.12b)) and remain so until local (spinodal) instabilities kick in to induce phase separation. This corresponds to the turning point around $\varphi = -0.5$.

3.4.1 Uniform state

On the upper branch in the phase space plot in figure (3.12b), $\phi(x, t) = \varphi(t)$ and the uniform phase is locally stable. All conservative terms vanish and $\varphi(t)$ evolves only according to the global Model A dynamics,

$$\dot{\varphi} = -M_{\mathrm{A}} u (\varphi - \phi_{\mathrm{a}})(\varphi - \phi_{\mathrm{t}}) \tag{3.76}$$

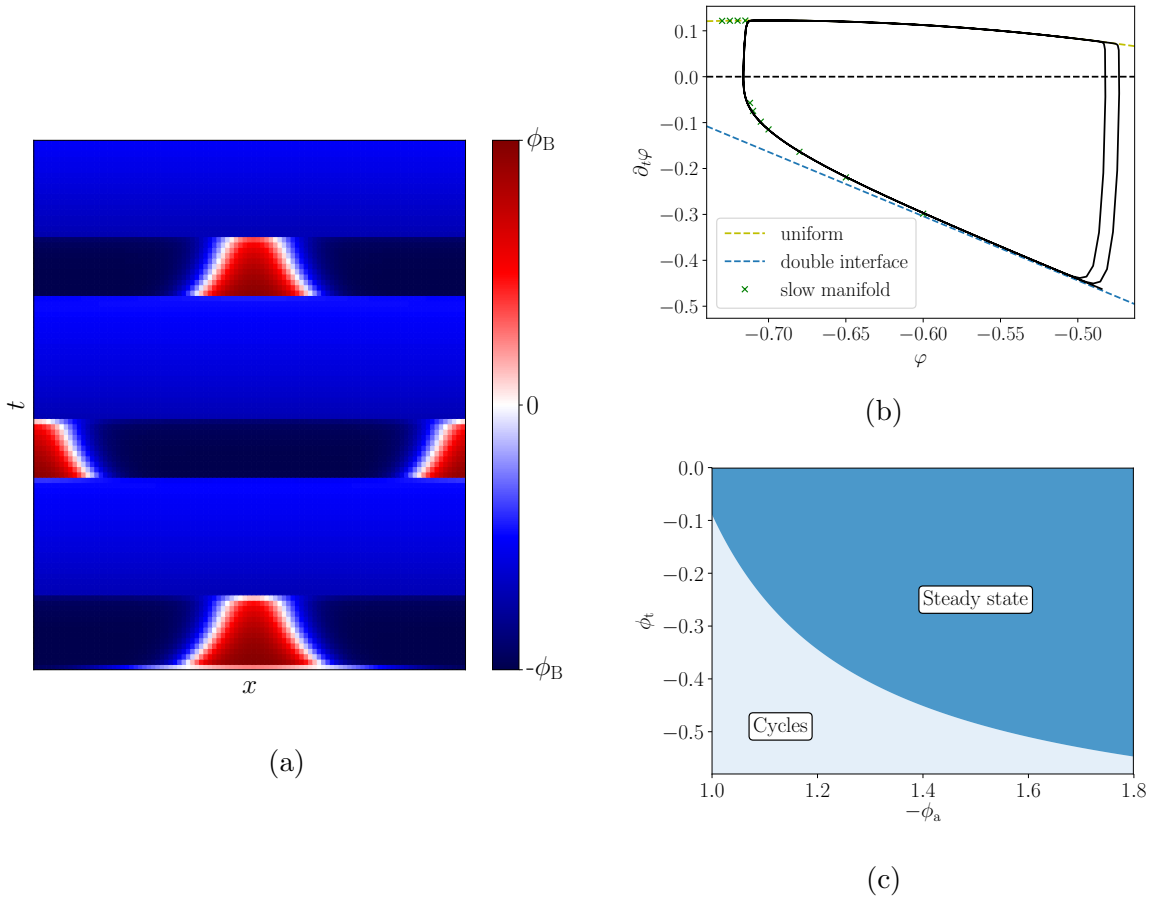

Figure 3.12: (a) shows a space-time plot of the ϕ field and (b) shows the phase-space plot of the same simulation. In (b) the green crosses are numerical simulations of the slow manifold, the yellow line corresponds to equation (3.76) and the blue line corresponds to equation (3.79). The parameters for the simulation are $uM_A = 5 \times 10^{-10}, \phi_a = -1.05, \phi_t = -0.35, \alpha = \beta = 0.001, \kappa = 1, X = 800$. Panel (c) shows the phase diagram in the $(-\phi_a, \phi_t)$ plane in the limit $uM_A \to 0$.

Thus $\dot{\varphi}$ is positive for $\varphi < \phi_\mathrm{t}$. As long as ϕ_t is within the spinodals, condition (C2) will be satisfied[3].

3.4.2 Phase-separated state

The nonlinearity of the reaction rates is crucial in satisfying (C1). For suppose the reaction rates are linear: $\mu_\mathrm{A} = -u(\phi - \phi_\mathrm{t})$. Integrating over the spatial coordinates gives $\dot{\varphi} = -M_\mathrm{A} u(\varphi - \phi_\mathrm{t})$, implying that φ exponentially decays towards ϕ_t regardless of the spatial distribution $\phi(\boldsymbol{x}, t)$. Since (C2) constrains that ϕ_t must lie within the spinodals, where a bulk phase-separated solution is always stable, (C1) can never be satisfied without nonlinearity in the Model A sector.

To address the effects of such nonlinearity within our canonical Model AB, defined by (3.22), we will need to know the spatial distribution $\phi(\boldsymbol{x})$ for the phase-separated states that make up the slow manifold. To simplify the analysis, we restrict to 1D (or higher dimensions but with spatial variation of the density along a single axis only) where Model B can be solved analytically in an infinite system:

$$\phi(x) = \phi_\mathrm{B} \tanh\left(q_c(x - x_0)\right) \tag{3.77}$$

Here $q_c = \sqrt{\alpha/2\kappa}$ as before, and the value of x_0 is such that $\int \mathrm{d}x \phi(x) = X\varphi$, where X is the length of the domain. In a finite system with periodic boundary conditions, we can construct an approximate solution by adding two tanh profiles together [72]. Taking a domain $\Omega = [-X/2, X/2]$,

$$\phi(x)/\phi_\mathrm{B} = 1 - \tanh\left(q_c(x - x_0)\right) + \tanh\left(q_c(x + x_0)\right) \tag{3.78}$$

Notice that this solution breaks down when φ gets too close to the binodals, $\varphi = \pm\phi_\mathrm{B} + \mathcal{O}(1/q_c X)$, as the minority phase region is then smaller than the width of two tanh-profiled interfaces. Otherwise, the approximate solution holds (see figure 3.12b); we can then substitute (3.78) into (3.22) and integrate over Ω, to obtain

$$\begin{aligned} \dot{\varphi} &= -M_\mathrm{A} u(-\phi_\mathrm{a} - \phi_\mathrm{t})(\varphi - \phi_\mathrm{nt}), \\ \phi_\mathrm{nt} &= \frac{\phi_\mathrm{a}\phi_\mathrm{t} + \phi_\mathrm{B}^2(1 - 4(q_c X)^{-1})}{\phi_\mathrm{a} + \phi_\mathrm{t}} \end{aligned} \tag{3.79}$$

Noting that $\phi_\mathrm{a} < 0$, we thereby predict a new target (subscript "nt") for the global density φ in the phase-separated system that can be less than ϕ_t for uniform states.

The limit-cycle arises when a negative $\dot{\varphi}$, caused by phase separation, remains negative

[3]Strictly speaking, we require ϕ_t to lie within the range of φ that makes the lowest Fourier mode of ϕ fluctuations linearly unstable; this defines the spinodal regime for a finite, as opposed to infinite, system.

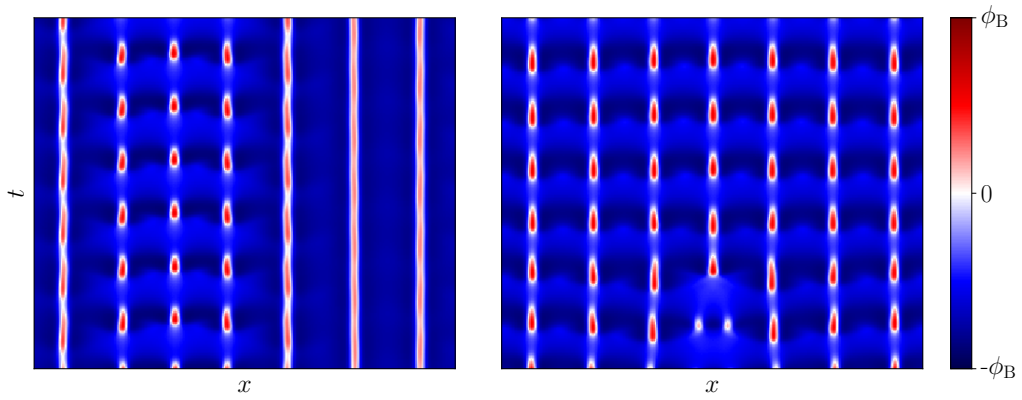

Figure 3.13: Space-time plots of two simulation runs with the same parameters but different initial conditions. The left panel starts with a uniform state with small random noise; the right panel is initialised with a high-density bump in the middle. The parameters are $\phi_a = -1.05, \phi_t = -0.45, uM_A = 2 \times 10^{-4}, \alpha = \beta = 0.1, \kappa = 1, X = 600$.

until the phase-separated state becomes locally unstable under the Model B dynamics and it remixes. The new target density obtained above gives a useful guideline: cyclic behaviour is predicted for $\phi_{nt} < -\phi_B$, modulo our use of approximation (3.78). To improve on this criterion requires numerical simulations of the slow manifold – the green crosses in figure (3.12b). Close to the turning point on the left, the slow manifold has deviated significantly from the tanh-profiled approximation: the dense phase occupies a region of order the interfacial width, and the peak density of this dense region is much lower than the binodal density. To obtain a more accurate estimation of the threshold between limit cycles and the steady state, we must look at the phase-separated state on the slow manifold with the smallest φ and calculate the total reaction rate (for various ϕ_a and ϕ_t). If the total rate is negative, (C1) is satisfied and there is a limit cycle. The resulting phase diagram in shown in figure (3.12c).

Roughly speaking, limit cycles only occur for ϕ_a close to $-\phi_B$ and ϕ_t close to $-\phi_S$, so that the two phases ($\pm\phi_B$) have vastly different reaction rates, and the loss of ϕ within in a small region of the dense phase can balance the total production of ϕ in the much larger region of dilute phase. This leads to a steady decline in the global density φ within the phase-separated state, which brings the system back close to the binodal density, at which point it remixes. Having done so, there is now a net global production ($\dot{\varphi} > 0$) and the global density grows again until the spinodal density is reached, causing phase separation and completing the cycle.

3.4.3 Limit cycles beyond the slow reaction limit

In previous sections, we studied cycles in the limit $M_\mathrm{A} \to 0$. In practice, this requires the reaction to be significantly slower than diffusion so the dynamics can be formulated in terms of evolution along a slow manifold formed by steady states of the conservative sector [45]. More precisely, the time scale of reaction is $\sim 1/M_\mathrm{A}$ and the time scale of diffusion is characterised by the time to diffusive across the entire system, and is therefore of order $\sim X^2/D$, where $D = 2\alpha$ is the diffusion constant in either phase. Hence there is a time scale separation if $M_\mathrm{A} \ll D/X^2$.

When the time scales are comparable, the system goes through more complex limit cycles where all or part of the system oscillates between a phase separated state with multiple domains and the homogeneous state, as shown in figure 3.13. In this regime, for one unit of reaction time, the particles can only diffusive across part of the system, and this sets the domain lengths of the (transiently) phase separated state, not unrelated to the steady-state microphase separations discussed previously in which there is balance between diffusive fluxes and chemical processes of the kind shown in figure 2.1.

3.4.4 Mechanism of limit cycles

The limit cycle is an interesting but mathematically delicate phenomenon that requires some fine-tuning of parameters within our canonical Model AB. We can imagine that by choosing a different conservative model (with non-quartic $\mathcal{F}_\mathrm{B}$, and hence different spinodal and binodal curves) we might be able to expand the size of the "limit-cycle phase" in parameter space. However, there are many advantages in sticking with the canonical model because of its analytic tractability.

In particular, Grafke et al. studied the same limit cycle for a non-canonical model of bacterial phase separation with population dynamics, described by a non-polynomial $\mathcal{F}_\mathrm{B}$ with multiplicative noise [45]. There, the homogeneous to phase-separated limit cycle was suggested as a pre-evolutionary prototype for the planktonic-to-colonial life-cycle in bacteria. However the relative complexity of the model made it hard to fully elucidate the physical mechanism underlying the limit cycle. Addressing the same cycle within our much simpler Model AB allows the mechanism to be exposed more clearly, and with it, some potential limitations to its relevance to the bacterial life-cycle. Specifically, since the *global* density of motile bacteria must decrease with time throughout the lifetime of a colony, between its initial formation by phase separation and final loss by remixing, rather high rates of death (or at least of immotilization [45]) are required within the colony itself. Indeed, in the limit of small reaction rates, a single colony can sustain itself in coexistence with a finite planktonic reservoir but never an infinite one: in the latter case, such colony is predicted to redisperse on the fast (Model B) timescale. However, synchronised oscillations

with a finite density of colonies remain possible instead (cf. figure 3.13). The system size thus enters in a possibly unexpected way that would need to be better understood within any intended biophysical context involving an isolated colony.

3.5 Conclusion

In our exploration of the parameter space of Model AB, we found that our canonical model shows various phenomena previously reported for diverse, more microscopically inspired, and often more complicated, models spread across the literature. These phenomena include lamellar and droplet microphase separated patterns; emergence of a stable radius in the single-droplet Ostwald process; droplet splitting dynamics; and steady state oscillations between a homogeneous ('planktonic') and a phase-separated ('colonial') state [7, 22, 23, 44, 45]. Of these phenomena, the limit cycles require oscillations of the global mean density in concert with the phase separation, so that choices of the nonlinearity parameter ϕ_a in the Model A sector, as well as its target density ϕ_t, is crucial in that regime.

In contrast, the other phenomena listed above can, in the main, be well accounted for using only linear reaction dynamics. This gives just two free parameters in the Model A sector at the deterministic level: the target density ϕ_t, and the reaction rate uM_A. The time evolution, starting from a uniform state, then falls into one of three categories: spinodal decomposition, nucleation and growth, and remaining homogeneous. In the limit of the reaction rate going to zero, these regimes correspond exactly to their Model B counterparts, but with the important restriction that ϕ_t sets both the global density and the far-field supersaturation in single-droplet growth (so that this supersaturation ceases to depend on droplet size, dramatically changing the growth law, see section 3.2.2). Moreover, the spinodal and binodal lines merge towards $\phi = 0$ as the reaction rate increases, until eventually the homogeneous state remains stable for all ϕ_t.

When the target density ϕ_t lies between the binodals, the Model AB dynamics leads to the coarsening becoming arrested by the reactions at a finite length-scale, resulting in microphase separation. This comprises lamellar or droplet/bubble patterns, whose geometry depends on the phase volume ratio. This is in turn set by the global mean density φ which, for linear reactions, evolves autonomously towards ϕ_t in steady state. These steady states may or may not show long range order; this depends on the noise level, and we have not explored it in detail, but see [44] for examples found within a more complicated non-canonical model framework. All such outcomes have natural explanations within the equilibrium mapping referred to above, but the same physics (figure 2.1) is seen far outside the parameter subspace where that mapping exists. In particular, the addition of Model A nonlinearity, introducing an extra unstable zero at ϕ_a in μ_A, obviates the mapping but does not change or destroy these three regimes, although it also admits new

behaviours, including a curious example where the stationary solution in a finite domain is a pronounced dumbbell-shaped droplet (figure 3.11).

If, instead of starting from a homogeneous phase, the system is initialized with large domains of the two phases, the system anti-coarsens until the steady-state microphase-separation pattern is recovered (see, for example, figure 3.5). This is again easily explained within the subspace of the equilibrium mapping where there is a unique Boltzmann equilibrium which the stochastic dynamics of Model AB will find eventually (modulo the possible intrusion of glass physics with long relaxation times to escape metastable states). One notable mechanism of anti-coarsening involves a large droplet stretching into a dumbbell shape and splitting into two or more smaller ones (figure 3.9).

Within the subspace of the equilibrium mapping, the role of noise in steady states is fully addressable using the methods of finite-temperature equilibrium statistical mechanics. Away from this subspace it is relatively intractable analytically. Therefore, in addressing the more general phenomenology of Model AB, the effects of noise were only studied numerically in this work. There is room for further exploration of noise effects; for example, we found that the length-scales of the same microphase-separated morphologies depend strongly on the noise strength ϵ. For droplets, the noise provides (via nucleation) a selection mechanism which decides the number density of droplets in the system; without it, there is separately stable static solution for any such number density. A very similar effect was reported recently in a purely conservative model (Active Model B+) where gradient nonlinearities, rather than non-conservative dynamics, are responsible for arrest of phase separation [11]. Accordingly, the role of noise in model AB represents an interesting avenue for future work.

Chapter 4

Hierarchical microphase separations in Model AB+

In the previous chapters, we explored the phenomenology of Model AB, constructed to describe active mixtures with phase-separating conservative dynamics and chemical reactions of separate energetic causes. One distinct feature of Model AB is that microphase separation, rather than bulk phase separation, occurs whenever the stable fixed point of the homogeneous reaction dynamics lies between the binodals of the conservative phase separation.

Meanwhile, microphase separated states have also been reported in fully conservative active systems described by Active Model B+ (AMB+). This model is constructed by adding a complete set of lowest-order non-equilibrium current terms to the standard (passive) Model B [21] (with differing outcomes, in more than one dimension, from an earlier, less complete, Active Model B [73]) [11]. The active terms in AMB+ can send into reverse the Ostwald process for droplets, which would normally lead to full phase separation by causing small droplets to shrink and disappear while large ones grow [47]. The reverse Ostwald process, which formally emerges through a negative effective interfacial tension in the expression for the Laplace pressure at the droplet surface, instead equalises the droplet sizes. (Note that other definitions of interfacial tension do not become negative, so that droplets remain stably spherical for example.) In the absence of noise, this mechanism creates a set of uniformly sized droplets whose number is governed by the initial condition. However, when noise is present, this ultimately selects the length scale for microphase separation by a subtle interplay of various effects. (Those effects include noise-induced nucleation of small droplets and coalescence of large ones, coupled to a collective homogenization of droplet size caused by reverse Ostwald [11].)

As just described, Model AB and AMB+ both involve a single scalar field on its own. More elaborate active field theories can be constructed by coupling a compositional scalar to a momentum-preserving fluid flow, along lines establised in passive systems

such as 'Model H' [21]. It is known that this coupling can give further distinctive routes to microphase separation, for example when activity in effect reverses the sign of the interfacial tension that governs the stress exerted on the fluid at the boundary of the droplet (but without doing the same for the Ostwald currents). This happens when the droplet is made of so-called 'contractile' material [74, 75]. In this chapter we omit these further complications, and consider only how to combine the types of physics already captured by Model AB and AMB+, in which there is no separate momentum conservation, and the reaction-diffusion dynamics of ϕ give a complete description of the pertinent physics.

In chapters 2 and 3, we broke TRS only at the lowest possible order in $(\boldsymbol{\nabla}, \phi)$. This entails choosing chemical potentials for the Model B and Model A sectors that could each give an equilibrium system in the absence of the other, so that $\mu_{\mathrm{A,B}} = \delta F_{\mathrm{A,B}}/\delta\phi$, but also choosing $F_{\mathrm{A}} \neq F_{\mathrm{B}}$. This leads to phase separation via the mechanism described previously. However, in a given physical system, once TRS is broken in this fashion it is likely to be broken elsewhere as well. In particular, we know that the active currents represented by the mass-conserving AMB+ (which do not derive from any local chemical potential, of the form $\delta F/\delta\phi$ or otherwise), can independently cause microphase separation via the reverse Ostwald process [11]. Even if these are formally subdominant when expanding in $(\boldsymbol{\nabla}, \phi)$, such terms can in principle interact in a strongly non-additive way with the microphase separation in Model AB, particularly if parameters are chosen so that the two mechanisms act on well-separated length- and time-scales.

Accordingly, in this chapter we construct Model AB+ which includes both types of TRS breaking at once, and use it to give a first account of the interplay between the two mechanisms of microphase separation. Our aim in this brief and exploratory study is not to comprehensively explore the parameter space, but rather to show proof of principle that new physics can indeed emerge from this combination of mechanisms. In particular, in the case where the chemical reactions are slow, we will give numerical evidence for a hierarchical phase separation in which the conservative and non-conservative mechanisms act simultaneously at small and large length-scales respectively. This results in a new, dynamical steady-state structure that we call 'bubbly microphase separation'.

This chapter is organised as follows. In section 4.1, we summarise the original Model AB and recall its various stationary patterns before introducing Model AB+. Section 4.2 then explores some steady states of Model AB+ with comparisons to the corresponding Model AB pattern without the active current terms from AMB+. These include droplet emulsions alongside the bubbly microphase-separated state. We then present in section 4.3 a mean-field Ostwald-type calculation for growth of a $\phi > 0$ (liquid) droplet in a bath with $\phi < 0$ (vapour). This explains a transition (or crossover) between statistically different droplet emulsion states upon increasing the target density of the chemical reactions above

the dilute binodal of the conservative phase separation. Section 4.4 briefly summarises these findings and suggests directions for future work.

4.1 Model AB+

We will first briefly recap Model AB and introduce Active Model B+, before combining their dynamics to construct Model AB+.

Model AB, constructed in chapter 2 as a combination of Model B and Model A, is a minimal field theory for a scalar composition variable $\phi(\boldsymbol{x})$, in reaction-diffusion systems in which the conservative part of the dynamics, taken alone, would give phase separation. Recall from equation (2.29),

$$\begin{aligned} \partial_t \phi &= -\boldsymbol{\nabla}\cdot\boldsymbol{J} - M_{\mathrm{A}}\mu_{\mathrm{A}} + \sqrt{2\epsilon M_{\mathrm{A}}}\Lambda_{\mathrm{A}} \\ \boldsymbol{J} &= -M_{\mathrm{B}}\boldsymbol{\nabla}\mu_{\mathrm{B}} + \sqrt{2\epsilon M_{\mathrm{B}}}\boldsymbol{\Lambda}_{\mathrm{B}} \\ \mu_{\mathrm{B}} &= -\alpha\phi + \beta\phi^3 - \kappa\nabla^2\phi \\ \mu_{\mathrm{A}} &= u(\phi-\phi_{\mathrm{a}})(\phi-\phi_{\mathrm{t}}) \end{aligned} \tag{4.1}$$

Here $M_{\mathrm{A,B}}$ are mobility constants, $\Lambda_{\mathrm{A}}, \boldsymbol{\Lambda}_{\mathrm{B}}$ are spatiotemporal white noises and α, β, κ, u are positive constants. The parameter ϵ is temperature, or an equivalent noise parameter in cases where the primary noise source is not thermal. We also assume that $\phi_{\mathrm{a}} < \phi_{\mathrm{t}}$. Here ϕ_{a} is the absorbing state composition of the reaction diffusion dynamics (this would be the zero density state for a birth-death system), which marks the physical lower limit for ϕ, whereas ϕ_{t} is the 'target density' of the chemical reactions, such that there is a stable fixed point of the dynamics at $\phi(\boldsymbol{x}) = \phi_{\mathrm{t}}$, *if* the diffusive tendency to phase separate is switched off.

As discussed in the previous chapter, if the reactions are switched off ($M_{\mathrm{A}} \to 0$), the diffusive sector of the dynamics drives the system towards bulk phase separation with the two coexisting phases at the binodal densities, $\phi = \pm\phi_{\mathrm{B}} = \pm\sqrt{\alpha/\beta}$, as long as the mean density ($\bar{\phi} = \frac{1}{V}\int \mathrm{d}\boldsymbol{x}\, \phi(\boldsymbol{x})$) is between the binodals. With reactions, broadly speaking, if the target density ϕ_{t} of the non-conservative sector is between the binodals, the system exhibits microphase separation, where material is created in a dilute region, transported across the interface by the Model B current, and eventually destroyed in a dense region. The morphology depends on the value of ϕ_{t}, as shown in the upper panels of figure (4.1). For ϕ_{t} close to zero, the system shows lamellar patterns; otherwise, we either see a droplet phase or its inverse, a bubble phase, depending on which binodal ϕ_{t} is closer to.

Model AB breaks time reversal symmetry solely by having mismatched free energies in the nonconserved (Model A) and conserved (Model B) sectors. But of course, each sector can, in principle, break detailed balance on its own. In the Model A sector this

requires gradient terms in μ_{A} that do not stem from a free energy. At leading order in the gradient expansion, the resulting 'Model A+' will not lead to microphase separation under steady-state conditions because, without a conservation law, there are no interfaces in the steady state at which such terms could be large. Instead we expect relaxation towards a uniform state at zero μ_{A}, or $\phi = \phi_{\mathrm{t}}$. These active 'A+' terms can of course modify the microphase separation caused by the competing conserved and non-conserved dynamics in Model AB, but we don't expect them to introduce a second type of microphase separation.

In what follows, we therefore focus on enhancing Model AB by adding active gradient terms to the conservative sector where such terms can lead to microphase separation in their own right. The terms in question are those of Active Model B+ [11],

$$\begin{aligned} \partial_t \phi &= -\boldsymbol{\nabla} \cdot \boldsymbol{J} \\ \boldsymbol{J} &= M_{\mathrm{B}} \left[-\boldsymbol{\nabla} \left(\mu_{\mathrm{B}} + \lambda \left| \nabla \phi \right|^2 \right) + \zeta (\nabla^2 \phi) \boldsymbol{\nabla} \phi \right] + \sqrt{2 \epsilon M_{\mathrm{B}}} \boldsymbol{\Lambda}_{\mathrm{B}} \end{aligned} \tag{4.2}$$

where μ_{B} is the same as before. The λ and ζ terms are the lowest order Landau-Ginzburg terms that break TRS in systems with ϕ conservation. (One other term at this order can be absorbed into a ϕ-dependent square-gradient coefficient $\kappa(\phi)$ without breaking the free energy structure [76].) It has been shown that the λ and ζ terms not only shift the binodals, but that the latter can also lead to effectively negative surface tensions for either liquid droplets ($\phi > 0$) or vapour bubbles ($\phi < 0$), albeit not both at once, depending on the sign of ζ [11]. The tension in question is the one governing Laplace pressures and hence Ostwald ripening, not other physics (such as fluctuations at the interface between phases which remains stable). The resulting reverse Ostwald process causes microphase separation into an emulsion of finite droplets that do not coarsen, which is of course not seen in equilibrium Model B. In renormalization-group terms, this microphase separation appears to be connected with a strong coupling regime at large enough values of (λ, ζ). As such, these variables remain important even though, being higher order in the Landau-Ginzburg expansion, the are formally irrelevant in the neighbourhood of the Wilson-Fisher fixed point which controls the critical onset of bulk phase separation [76].

This suggests that equally important physics could also be lost by ignoring these non-integrable gradient terms in the conservative sector for systems with both conserved and non-conserved dynamics, whereas we did ignore them when constructing Model AB as a canonical model for that case in chapters 2 and 3. In light of this, we now construct Model AB+ by adding the λ and ζ terms to the conservative sector of Model AB, so that

(4.1) is replaced by:

$$\begin{aligned}
\partial_t \phi &= -\boldsymbol{\nabla} \cdot \boldsymbol{J} - M_{\mathrm{A}} \mu_{\mathrm{A}} + \sqrt{2\epsilon M_{\mathrm{A}}} \Lambda_{\mathrm{A}} \\
\boldsymbol{J} &= M_{\mathrm{B}} \left[-\boldsymbol{\nabla} \left(\mu_{\mathrm{B}} + \lambda \left| \nabla \phi \right|^2 \right) + \zeta (\nabla^2 \phi) \boldsymbol{\nabla} \phi \right] + \sqrt{2\epsilon M_{\mathrm{B}}} \boldsymbol{\Lambda}_{\mathrm{B}} \\
\mu_{\mathrm{B}} &= -\alpha \phi + \beta \phi^3 - \kappa \nabla^2 \phi \\
\mu_{\mathrm{A}} &= u(\phi - \phi_{\mathrm{a}})(\phi - \phi_{\mathrm{t}})
\end{aligned} \tag{4.3}$$

The rest of this chapter addresses Model AB+ as written in the form (4.3). All numerical simulations are performed in $d = 2$ with periodic boundary conditions. The simulation techniques are the same as before (see beginning of chapter 3). Throughout this chapter, unless otherwise stated, we set $M_{\mathrm{B}} = 1, \alpha = \beta = 0.25, \kappa = 1, u = (-\phi_{\mathrm{a}} + \phi_{\mathrm{t}}/2), \phi_{\mathrm{a}} = -10$ for consistency with chapter 3. Note that we make no attempt at a systematic exploration of parameter space, but focus on selected regimes where new physics can be expected by adding nonzero λ, ζ terms to parameter sets that we used previously to study Model AB. (In particular, the somewhat arbitrary choice for u was adopted in the previous chapter and is kept here for consistency. In principle, one can simply set $u = 1$ and the results will be qualitatively the same.)

4.2 Steady states

Model AB+ has at most one stationary state of uniform density, which lies at the target density ϕ_{t}. (Any other uniform state has $\dot{\phi} \neq 0$ from the reactions, with no diffusive currents that could balance this.) Similar to the calculation for Model AB in section 3.2.1, linear stability analysis finds this uniform state to be unstable to spatial perturbations if

$$M_{\mathrm{B}} \frac{\tilde{\alpha}^2}{2\kappa} > M_{\mathrm{A}} \tilde{u} \tag{4.4}$$

where $\tilde{\alpha} = 2\beta\phi_{\mathrm{t}}^2 - \alpha$, $\tilde{u} = u(-\phi_{\mathrm{a}} + \phi_{\mathrm{t}})$. The two sides of the inequality represent characteristic relaxation rates via diffusion and reactions, respectively, on length scales set by κ. In many biological situations, relatively rapid thermal diffusion of chemical species is accompanied by a relatively slow reaction-driven turnover time, so that this 'slow reaction' condition is easily obeyed. Hence in this chapter we focus on the unstable regime far away from the threshold of linear instability. We further assume that $\phi_{\mathrm{a}} \ll -\phi_{\mathrm{B}}$ so the reaction dynamics is approximately linear in $\phi(\mathbf{x})$ for values lying between the binodals. This means that we have an approximate symmetry $(\lambda, \zeta, \phi) \to (-\lambda, -\zeta, -\phi)$ in our system, similar to Active Model B+ where this symmetry is exact [11].

Some typical steady states are shown in figure (4.1) for $\lambda = -1, \zeta = -4$, where the Ostwald tension for droplets of the dense phase ($\phi > 0$) are negative. These are directly

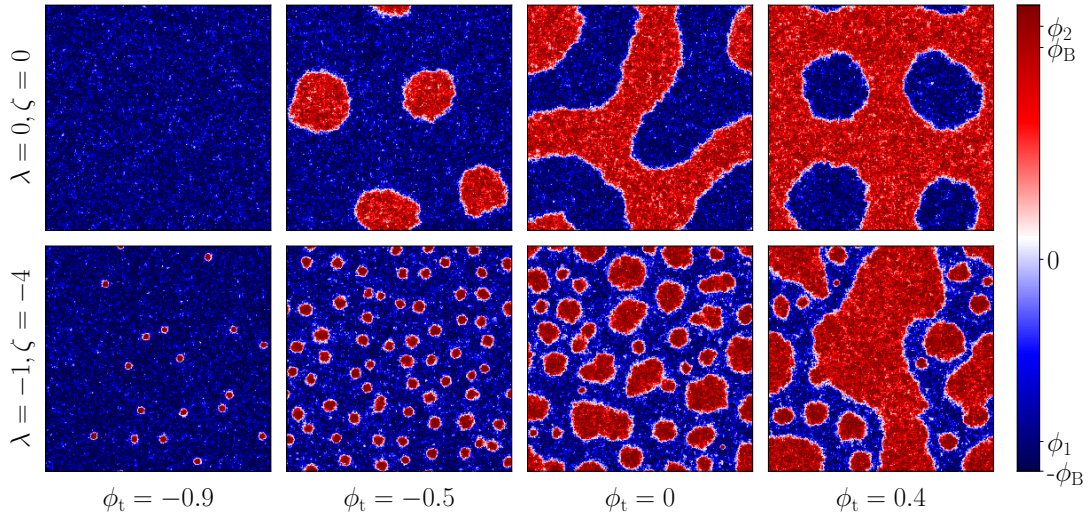

Figure 4.1: Steady state patterns for $\phi_t = -0.9, -0.5, 0, 0.4$ for two sets of (λ, ζ) values. For $\lambda = 0, \zeta = 0$ (as in Model AB), the patterns are stationary modulo noise fluctuations and are shown in the top panel. For $\lambda = -1, \zeta = -4$, the steady states are dynamical with droplets of the dense phase (red) constantly spawning in the dilute phase (blue), snapshots of which are shown in the bottom panel.

compared with the pure Model AB case ($\lambda = \zeta = 0$). For low values of ϕ_t, where pure model AB is in a uniform state we see an emulsion of these dense ('liquid') droplets in the dilute phase ('vapour', $\phi < 0$), stabilized by reverse Ostwald. At high ϕ_t, chosen so that the Model AB mechanism leads to a microphase-separated state with liquid phase in the majority (hence an emulsion of vapour bubbles in liquid), the active current terms cause phase inversion of this state so that the system is liquid-in-vapour. This is inevitable for sufficiently negative λ, ζ where the conservative dynamics causes microphase separation on a relatively short length scale since, importantly, these terms *only* stabilize liquid in vapour droplets and not vice versa (unless their signs are reversed, in which case so is the whole phase diagram).

Because even at these parameter values the binodals $\phi_{2,1}$ are only modestly shifted from the equilibrium values $\pm\phi_B$, the global phase volumes of the liquid and vapour phases remain primarily under the control of the reaction dynamics and are hence set by ϕ_t. At large enough values of this quantity the majority liquid phase unavoidably percolates, but the minority phase of disconnected large vapour bubbles contain within them small liquid droplets that are stabilized by reverse Ostwald. (The interior of such a bubble thus resembles a piece of the liquid-in-vapour emulsion seen at smaller ϕ_t.) These small liquid droplets are continuously produced within the vapour bubbles but then grow, diffuse and merge into the surrounding liquid phase. This behaviour closely resembles the 'bubbly phase separation' reported previously for AMB+, except that in the latter case, there is only a single vapour domain in the system which can effectively be viewed as a bulk phase separation between the liquid-in-vapour emulsion and excess liquid [11]. (Note also

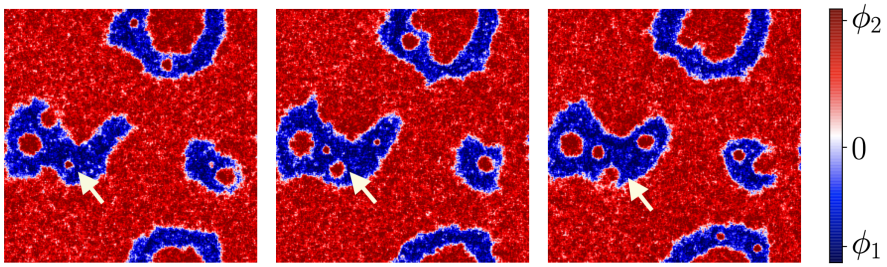

Figure 4.2: Three snapshots of the life-cycle of a dense droplet created inside the dilute phase, as indicated by the arrow. The simulation parameters are $uM_{\mathrm{A}} = 10^{-6}, \phi_{\mathrm{t}} = 0.6$.

that [11] mainly addresses the case with $\lambda, \zeta > 0$ for which the identities of the 'liquid' and 'vapour' phases are, trivially, interchanged from those in the present discussion.) In the presence of the Model AB mechanism, this type of emulsion/liquid bulk phase separation is itself unstable since the bulk liquid phase is not at the target density. Accordingly, for slow reaction dynamics the system must homogenise once again at some larger scale so that the chemical conversion of the majority into the minority species in each neighbourhood can be balanced by diffusive mass transport. Accordingly we see a finite density of the large liquid-in-vapour emulsion bubbles whose size cannot grow further. Echoing the language of [11], we refer to this state as 'bubbly microphase separation'.

A snapshot of the life-cycle of droplets is shown in figure (4.2) showing the growth of a small nucleated droplet, its growth, and coalescence into the surrounding liquid phase. As stated previously this echoes the findings of [11] for the life cycle of liquid droplets within a bulk phase separation between an emulsion of such droplets and excess liquid.

4.3 Ostwald Dynamics in Model AB+

In the mean field limit, the binodals of AMB+, defined as the steady state coexisting densities for a flat interface, can be computed analytically [74]. We will not show the calculation here but merely quote the results for $\lambda = -1, \zeta = -4$: the dense binodal shifts to $\phi_1 = 1.10$ and the dilute binodal shifts to $\phi_2 = -0.86$. These replace the values $\pm\phi_{\mathrm{B}} = \pm 1$ for the passive model (with $\alpha = -\beta$ as chosen above).

In addition, around circular two-dimensional droplets, the density ϕ close to the interface is further modified by an offset depending on the radius of the droplet R. In equilibrium Model B, this curvature induced shift around a liquid droplet is proportional to σ/R, where σ is the surface tension. As shown in [11] for AMB+ the surface tension defined this way can be negative for sufficiently negative of λ and ζ, thus reversing the Ostwald ripening for droplets, arresting their growth at a finite size. If we now switch on the chemical reactions to give Model AB+, then so long as these reactions are slow (which

is the regime addressed in this chapter) the dynamics on the length-scale of the interface width $\xi_0 \simeq \sqrt{\kappa/2\alpha}$ is dominated by the conservative current. This means that we can carry across from AMB+ the results for the curvature-induced offset to the binodals.

Consider N liquid droplets of radius $R_j \gg \xi_0$ for $j \in (1, 2, \ldots, N)$ in a dilute bath in a domain of volume V with periodic boundary conditions. We now single out one droplet of radius R_i and treat the rest as homogeneous background. Let $\phi_\pm(\boldsymbol{x})$ be the composition field inside and outside the singled-out droplet respectively, and define variables $\psi_\pm(\boldsymbol{x})$ as the deviation from the modified binodal densities:

$$\begin{aligned} \phi_-(\boldsymbol{x}) &= \phi_2 + \psi_-(\boldsymbol{x}) \qquad |\boldsymbol{x}| \geq R_i \\ \phi_+(\boldsymbol{x}) &= \phi_1 + \psi_+(\boldsymbol{x}) \qquad 0 \leq |\boldsymbol{x}| < R_i \end{aligned} \tag{4.5}$$

For reasons given in section 3.2.2.1, provided that ϕ_t is close to the modified dilute binodal ϕ_2 (so that there is a large excess of vapour around the droplet), and so long as the timescale separation between conservative and nonconservative dynamics holds (slow reaction regime), we can linearise the deterministic part of equation (4.3) to obtain,

$$\begin{aligned} \partial_t \psi_- &= D_- \nabla^2 \psi_- + (1-\lambda) g_-^0 + g_-^1 \psi_- + V^{-1} \sum_{j=1}^{N} 2\pi R_j J_-^j \\ \partial_t \psi_+ &= D_+ \nabla^2 \psi_+ + g_+^0 + g_+^1 \psi_+ \end{aligned} \tag{4.6}$$

where $D_\pm = M_\mathrm{B}(-\alpha + 3\beta(\phi_{1,2})^2)$ and we have defined $g(\phi) = -M_\mathrm{A}\mu_\mathrm{A}(\phi), g_\pm^0 = g(\phi_{1,2}), g_\pm^1 = g'(\phi_{1,2}), \lambda = V^{-1}\sum_j \pi R_j^2$ for conciseness. In the last term in the equation for ψ_-, J_-^j denotes the current at the surface of the jth droplet and thus this term accounts for the injection of mass by all the droplets. Note that we neglect the κ term here as ψ varies on a length-scale much larger than the interfacial width. The linearised equations need to be solved with the appropriate boundary conditions: at $|\boldsymbol{x}| \to 0$ and $|\boldsymbol{x}| \to \infty$, we only need $\psi_\pm$ to be finite; at the boundary of the droplet, we require $\psi_\pm = \delta_\pm(R)$, where $\delta_\pm(R)$ is the aforementioned offset for the dense and dilute phase respectively.

We will now sketch the perturbative Ostwald calculation with results presented only at key steps and refer to section 3.2.2.1 for more detailed explanations of the scheme. This is inspired by the standard Ostwald calculation for both passive and active systems [11, 47] and its adaptation to multiple droplets [1, 58], but we implemented it here, for the first time, to include *both* the nonconservative reaction terms in the bulk phases *and* the effects of active currents on the matching conditions (following [11]) which cause reversal of the Ostwald dynamics.

For fixed droplet radii $\{R_j\}$, we solve for the stationary state of the linearised equations with $\psi_\pm(R_i) = \delta_\pm(R_i)$, then compute the current $J_\pm^i$ at the interface with the quasi-static

solutions as a function of the droplet radii $\{R_j\}$,

$$\begin{aligned} J_+^i &= D_+ k_+ (c_+ - \delta_+(R_i)) \frac{I_1(k_+ R_i)}{I_0(k_+ R_i)} \\ J_-^i &= -D_- k_- (c_-^i - \delta_-(R_i)) \frac{K_1(k_- R_i)}{K_0(k_- R_i)} \\ c_-^i &= c_-(1-\lambda) - (g_-^1 V)^{-1} \sum_{j=1}^{N} 2\pi R_j J_-^j \end{aligned} \tag{4.7}$$

where $K_{0,1}, I_{0,1}$ are the modified Bessel functions, $k_\pm = \sqrt{-g_\pm^1/D_\pm}$ and $c_\pm = -g_\pm^0/g_\pm^1 \approx \phi_\mathrm{t} - \phi_{2,1}$. At the surface of the singled-out ith droplet (treating the rest as a homogeneous bath), the mismatch of the diffusive currents on the two sides of the interface $J_\pm^i$ creates a non-zero velocity for the droplet boundary, thus changing the radius of the droplet,

$$\partial_t R_i = \frac{J_+^i(R_i) - J_-^i(\{R_j\})}{\phi_1 - \phi_2} \tag{4.8}$$

So far, we have reduced the multiple-droplet dynamics to N coupled equations for $\{R_j\}$ by treating each droplet in isolation. One can then immediately spot a solution where all the droplets have the same radius. Let this radius be R, the currents J_-^i can then be obtained explicitly by substituting the c_-^i equation into the J_-^i equation:

$$J_-^i(R) = -D_- k_- \frac{K_1}{K_0} (c_-(1-\lambda) - \delta_-(R)) \left(1 - \frac{2\lambda D_- k_-}{g_-^1 R} \frac{K_1}{K_0}\right) \tag{4.9}$$

where the arguments of the modified Bessel functions $K_{1,0}$ have been omitted to ease notation. Substituting eq. (4.9) into eq. (4.8) yields the growth rate $\dot{R}$ as a function of R. The resulting analytical expression for the $\dot{R}(R)$-curve is plotted in figure (4.3a) for one droplet in a box of size 256^2 for $\phi_\mathrm{t} < \phi_1$ and $\phi_\mathrm{t} > \phi_1$. Both plots show a stable fixed point: smaller droplets grow towards the stable radius, and larger droplets shrink towards it. These facts respectively explain the spontaneous emergence of liquid droplets within the vapour phase (given the presence of noise at short scales) and also the arrested growth of droplets shown in figure (4.1). There are, however, some important differences between the two plots in figure (4.3a). Observe that the curve for the currents inside the droplet $J_+(R)$ are similar in the two panels, whereas the current in the vapour phase $J_-(R)$ are qualitatively different. In the case where $\phi_\mathrm{t} < \phi_1$, $\psi_-(\boldsymbol{x}) \to c_- \approx (\phi_\mathrm{t} - \phi_1) < 0$ as $|\boldsymbol{x}| \to \infty$ whereas $\psi_-(R) \to 0$ for large R, leading to diffusive currents away from the droplet on the outside. In contrast, for $\phi_\mathrm{t} > \phi_1$, we have positive ψ_- at infinity, thus the current outside the droplet is always towards the droplet. This has profound consequences: for $\phi_\mathrm{t} < \phi_1$, the zero of the $\dot{R}$ has an upper bound at $\delta_-(R) = c_-$, which is independent of the reaction rate M_A; but for $\phi_\mathrm{t} > \phi_1$, there is no upper bound for the stationary fixed-point radius

(at least at the mean field level). Comparisons of the above analysis against numerical simulations with low noise are shown in figure 4.3b: although the perturbative Ostwald calculation does not quantitatively capture the exact time evolution of R, due to the quasi-static assumption, the stable radii between theory and simulations agree reasonably well.

As one increases the number of droplets in the Ostwald calculation (by changing $\lambda = N\pi R^2/V$ in equation (4.9)), the stable fixed-point radius decreases, also observed in [1]; though qualitatively, the fixed-point radius is still substantially larger for $\phi_t > \phi_1$ than $\phi_t < \phi_1$. This explains why, at fixed noise level, the emulsion of small and rather monodisperse liquid droplets seen in the bottom left panel of figure 4.1 takes on a quite different character in the two bottom centre panels, with relatively large and quite polydisperse droplets. Clearly in this high phase-volume emulsion state the droplets are neither uniform nor well separated, so that any further attempt to rationalize their statistics requires a much better understanding of the role of noise in the steady state kinetics. This lies beyond our scope; as noted previously, the issue is a surprisingly complicated one even in AMB+ where chemical reactions are absent [11].

For even larger values of ϕ_t, the Ostwald calculation above continues to qualitatively capture the growth of initially small liquid droplets within vapour regions, but as the droplets grow larger, they come into contact and either form or merge into the continuous phase of liquid which is present in the resulting regime of bubbly or hierarchical microphase separation.

4.4 Conclusion

In this chapter we have furthered our investigation into scalar field theories for non-equilibrium phase separating systems. Specifically, we have presented an initial study of the effect of having diffusive dynamics that breaks detailed balance on its own, on top of a mismatch of chemical potentials between the conservative dynamics and the non-conservative dynamics. This mismatch is separately a hallmark of broken time reversal symmetry (broken detailed balance) in active phase separation whenever both types of dynamics are present at once. The resulting new model, Model AB+, incorporates the λ and ζ terms, describing active currents in Active Model B+, into Model AB which focuses on the chemical potential mismatch in isolation. The latter causes microphase separation whenever the chemical reactions drive the system towards a target density that lies between the binodals of a conserved, diffusive phase separation.

This study was motivated by the ability of the active current terms to reverse the classical Ostwald process [11], which is also associated with a distinct strong coupling regime renormalization group calculations [76]. As a result, Model AB+ has two distinct

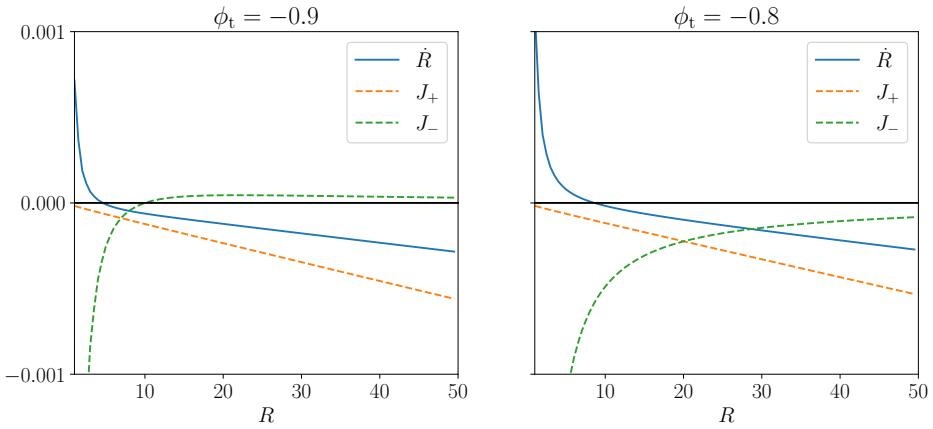

(a)

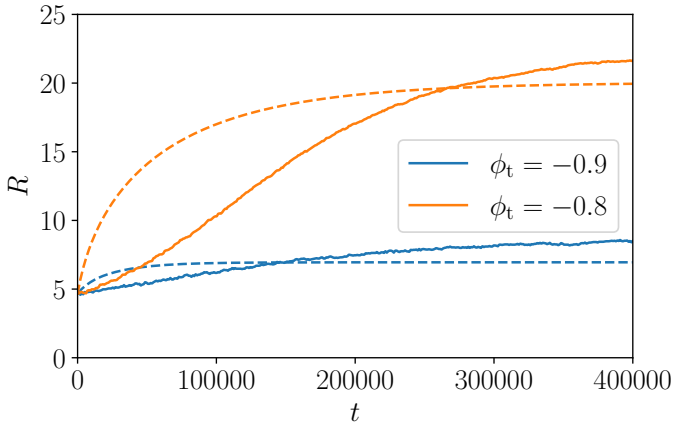

(b)

Figure 4.3: (a) Plots of the growth rate $\dot{R}$ and the currents inside J_+ and outside J_- for a dense (liquid) droplet of radius R in a dilute (vapour) bath for $\phi_t < \phi_1$ and $\phi_t > \phi_1$ (recall $\phi_1 = -0.86$). In both cases, the $\dot{R}$ curve crosses the x-axis from above, indicating a stable fixed point for R. The key difference is that in the left panel the J_- curve is positive as $R \to \infty$ whereas J_- remains negative on the right panel. (b) Comparisons between theoretical predictions (dotted line) against simulations (solid line) for $\phi_t < \phi_1$ and $\phi_t > \phi_1$. All plots are produced with the same reaction rate $uM_A = 1 \times 10^{-6}$. The noise level used in the simulations is $\epsilon = 0.001$.

mechanistic channels for microphase separation. Our work has shown that these can interact in nontrivial ways, giving two distinct types of emulsion state and also a 'bubbly' microphase separation in which the two processes are operative hierarchically on different scales. To be more specific, we focused our studies on parameter regimes where the surface tension for droplets of the dense 'liquid' phase is negative. For ϕ_t close to the dilute 'vapour' binodal ϕ_1, suspensions of stable droplets of finite size are observed. Ostwald calculations of a single droplet reveal that if $\phi_t < \phi_1$ there is an upper limit on the droplet size as $uM_A \to 0$ determined entirely by the diffusive dynamics; whereas for $\phi_t > \phi_1$ such an upper limit does not exist. The dynamics become more complicated for multiple droplets, though the qualitative conclusion remains that there are two structurally distinct liquid-in-vapour emulsions, as reflected in the phase diagram. On the other hand, for ϕ_t close to zero, the system settles into the bubbly microphase separated state, characterized by large but finite domains with densities at the two binodals, but with droplets of the liquid phase continuously created within the vapour domains before merging with the surrounding fluid.

Thus far, we explored some interesting behaviour of Model AB+, but made no attempt to systematically scan its multidimensional parameter space. There is, accordingly, plenty of room to find new physics beyond that presented here. For example, it would be interesting to see what is the interplay between the reverse Ostwald dynamics and the limit cycles observed in Model AB. In these cycles, there is no stationary phase separation but a cycle where phase separation leads to a slow reduction in global density until the system rehomogenizes, whereupon the global density reverses until the system phase separates again. (This is possible when the local reaction rate is sufficiently nonlinear in density.) It is not clear how this oscillation might interact with a conserved dynamics that favours microphase separation, especially when this is itself a highly dynamical process governed by a nontrivial life-cycle for droplets. Finally, as reported separately for Model AB and AMB+, the noise strength ϵ plays an important role in selecting the number and size of droplets in the emulsion state [1, 11] and this aspect deserves further study.

Finally, we have not made any attempt to connect the parameters or mechanisms of Model AB+ directly with any specific microscopic examples of active phase separation, whether within living cells [7, 39–41], bacterial colonies [44], or elsewhere. This is generally not easy because the model is constructed top-down to have a minimal structure. While the results are generic, only a comparison with more microscopic, bottom-up treatments can determine whether individual parameters are large or small in any particular case. For example, in purely conservative phase separation with ABPs (Active Brownian Particles), it was found that hard-core repulsion leads directly to the λ term in AMB+ but that to recover the ζ term, additional (e.g., soft-core) interactions are also required [11]. Despite these difficulties, we believe that the exploration of a generic model such as Model AB+

can suggest mechanistic explanations for structure formation in binary active systems that might otherwise be quite puzzling. A possible example is when there is emergent structure on more than one length scale, as arises in bubbly microphase separation (bottom right panel of figure 4.1).

Chapter 5

Steady state entropy production rate for scalar Langevin field theories

Motivated by the distinct non-equilibrium nature of active matter, recently there has been a surge of interest in quantifying the deviation from equilibrium, and entropy production is such a quantity [18, 27, 31, 32, 77–80].

In a seminal paper by Seifert [77], he introduced the notion of entropy production for a single trajectory, defined in terms of the probability of the forward and the backward path. The total entropy production can be split into two parts: the entropy production of the system and that of the medium (or heat bath). Upon averaging over the probability distribution, the entropy production of the system gives the Gibbs entropy $\left(-\sum_{\mathrm{n}\in\mathrm{states}} p_n \log p_n\right)$, whereas the medium entropy production is directly linked to the heat production in simple cases. Since then, there have been various works on entropy production in systems of particle in the context of active matter [18, 78, 79, 81].

On the other hand, at the macroscopic scale, it has been found that sometimes the coarse-graining procedure does not retain the strong non-equilibrium characteristics of the underlying microscopic interactions [31]. In some cases, the field theoretic description can be directly mapped to an equilibrium theory [6,11], such as the special equilibrium subspace in Model AB described in chapters 2 and 3. To explore this, Nardini et al. extended the definition of the entropy production to field theories, quantifying the amount of time reversal symmetry breaking at the macroscopic level [32]. They proposed an expression for the rate of entropy production of Active Model B (a special case of Active Mode B+ as described in chapter 4, that adds non-equilibrium perturbations to Hohenberg and Halperin's Model B [6, 21]) and computed its steady-state values via numerical averaging of stochastic trajectories.

Meanwhile, in the Macroscopic Fluctuation Theory literature, the concept of symmetric and antisymmetric currents were introduced for diffusive systems, as another way to pinpoint the irreversible aspect of the dynamics [33]. Bertini el al. constructed an adjoint

system whose forward time evolution is identical to a movie of the original system played backwards. Then the antisymmetric current corresponds to the difference between the original current and the current of the adjoint system.

In this chapter, we investigate the link between the entropy production rate and the antisymmetric current. We build upon the results of Nardini et al. [32] and study the entropy production rate (EPR) of the general class of scalar field theories with additive noise, including equilibrium Model A and Model B, which were systematically catalogued in Hohenberg and Halperin [21], as well as their non-equilibrium extensions, such as driven diffusive models [33] and Active Model B+ [6, 11]. Finally we use Model AB introduced in chapter 2 and 3 as a case study on the effect of tracking different information. Model AB describes systems with separate conservative and non-conservative dynamics, often driven by different underlying mechanisms. Recall from chapter 2 and 3 that we found a special subspace where time reversal symmetry is apparently restored for the density field, prompting questions on the behaviour of different EPRs in and near this equilibrium subspace.

The chapter is organised as follows. In section 5.1, we introduce the entropy production associated with a trajectory, as well as its decomposition in terms of internal entropy production and external entropy production, analogous to the system and medium splitting of Seifert [77]. Section 5.2 catalogues various scalar Langevin systems and their steady state solutions, including a detailed discussion of Model AB and its special equilibrium subspace. Next, in section 5.3, we compute the entropy production rate and its connection to the antisymmetric component of the dynamics (defined in a similar way to the antisymmetric current in Macroscopic Fluctuation Theory [33]). A small noise expansion of the EPR is also presented to make progress on models that are not exactly solvable and we demonstrate the method with an application to Model AB. In section 5.4, we investigate the effect of tracking different information by keeping account of separate Model A and Model B contributions to the dynamics in Model AB, and compare the resulting EPR with the results of tracking ϕ-evolution only. In the final section, the results are summarised and possible future work is proposed.

5.1 Entropy production

By the macroscopic nature of field theories, a trajectory or path in the space of field configurations is a bundle of all microscopic realisations that give rise to the same coarse grained description. The segregation into bundles depends on what macroscopic variables (such as the density of a species, the composition variable of a binary fluid or the local particle density) are tracked – broadly speaking, more information leads to finer bundles. The entropy production ΔS associated with such a trajectory is, according to stochastic

thermodynamics, defined as the log of the ratio of the probability of the forward trajectory and the backward trajectory [32, 77],

$$\Delta S = \log \frac{\mathbb{P}[\text{all microscopic realisations of the forward path}]}{\mathbb{P}[\text{all microscopic realisations of the backward path}]} \tag{5.1}$$

Thus it is impossible to talk about entropy production without specifying the information being tracked. Denote the set of available macroscopic variables as $\left\{\boldsymbol{X}(\boldsymbol{x},t)_{t\in[0,\tau]}\right\}$, where the components of $\boldsymbol{X}$ are the variables tracked, $(\boldsymbol{x},t)$ denotes the dependence of $\boldsymbol{X}$ on space and time, and τ is the length of the trajectory. Following the stochastic thermodynamics literature, we define an intermediate quantity, the rate function $\mathbb{R}$, as the log of the path probability $\mathbb{P}$ [27, 33],

$$\mathbb{P}\left[\{\boldsymbol{X}(\boldsymbol{x},t)_{t\in[0,\tau]}\}\right] \propto \exp\left(-\epsilon^{-1}\mathbb{R}\left[\{\boldsymbol{X}(\boldsymbol{x},t)_{t\in[0,\tau]}\}\right]\right) \tag{5.2}$$

where ϵ is a parameter that quantifies the amount of the noise (the meaning will become clear when we write down the rate function explicitly for a scalar Langevin system). Notation-wise, throughout this chapter we use $\mathbb{F}$ to denote functionals of a space-time trajectory, $\mathcal{F}$ for a functional of a spatial field configuration and F to denote functions. We will also silently omit the $\boldsymbol{x}$-dependence and the explicit time dependence of the trajectories from now on. For example, $\mathbb{P}[\{\boldsymbol{X}\}]$ is the probability of the a specific realisation of the time evolution of the fields from time 0 to τ, whereas $\mathcal{P}[\boldsymbol{X}(t),t]$ is the probability of observing the configuration $\boldsymbol{X}(t)$ at time t.

Next, we further factorise the path probability $\mathbb{P}[\{\boldsymbol{X}\}]$ into a product of the probability of the initial conditions $\mathcal{P}[\boldsymbol{X}(0),0]$ and the conditional probability of the evolution given the initial conditions $\mathbb{P}[\{\boldsymbol{X}\}|\boldsymbol{X}(0)]$,

$$\mathbb{P}[\{\boldsymbol{X}\}] = \mathcal{P}[\boldsymbol{X}(0),0]\,\mathbb{P}[\{\boldsymbol{X}\}|\boldsymbol{X}(0)] \tag{5.3}$$

Taking the logarithms of the both sides yields the splitting of the rate function $\mathbb{R}$ in terms of an "instantaneous quasipotential $\mathcal{V}$" (this is not the conventional definition of quasipotential [33] though they do coincide in steady state, which we denote as $\mathcal{V}_{\text{ss}}$) and the action $\mathbb{A}$ of the trajectory,

$$\begin{aligned}
\mathbb{R}[\{\boldsymbol{X}\}] &= \mathcal{V}[\boldsymbol{X}(0),0] + \mathbb{A}[\{\boldsymbol{X}\}] \\
\mathcal{P}[\boldsymbol{X}(t),t] &\propto \exp\left(-\epsilon^{-1}\mathcal{V}[\boldsymbol{X}(t),t]\right) \\
\mathbb{P}[\{\boldsymbol{X}\}|\boldsymbol{X}(0)] &\propto \exp\left(-\epsilon^{-1}\mathbb{A}[\{\boldsymbol{X}\}]\right)
\end{aligned} \tag{5.4}$$

where we note that the explicit t-dependence in $\mathcal{V},\mathcal{P}$ highlights the fact that the probability distribution $\mathcal{P}$ can change over time. In thermal equilibrium, $\epsilon^{-1}\mathcal{V}_{\text{ss}} = \beta\mathcal{F}$ where $\mathcal{F}$ is the

(mesoscopic) free energy functional and $\beta = 1/k_{\mathrm{B}}T$ is the inverse temperature.

In stochastic thermodynamics, the entropy production of a trajectory $\Delta S\left[\{\boldsymbol{X}\}\right]$ is defined as proportional to the difference between the rate function for the forward trajectory $\left\{\boldsymbol{X}(t)_{t\in[0,\tau]}\right\}$ and that of the backward trajectory $\left\{\boldsymbol{X}^{\mathrm{R}}(t)_{t\in[0,\tau]}\right\}$ [27, 77]. The backward time evolution is related to the forward one in a rather intuitive way: $X^{\mathrm{R}}_{\alpha}(t) = \theta_{\alpha}X_{\alpha}(\tau - t)$ where α denotes the index and $\theta_{\alpha} = \pm 1$ depending on whether the variable is even or odd under time reversal (e.g. current is odd, density is even) [27, 33],

$$\epsilon\Delta S[\{\boldsymbol{X}\}] = -\mathbb{R}[\{\boldsymbol{X}\}] + \mathbb{R}[\{\boldsymbol{X}^{\mathrm{R}}\}] \tag{5.5}$$

There is a technical detail associated with the path reversal: the action must be written with Stratonovich (midpoint) discretisation [27, 82] so that the time reversal of the trajectory has the same time discretisation as the forward trajectory [32]. Throughout this chapter, we adopt the Stratonovich discretisation scheme (except one occasion in appendix 5.A where another choice is explicitly stated).

Similarly to the splitting of the rate function, the entropy production can be decomposed into an internal $\Delta S_{\mathrm{Int}}[\{\boldsymbol{X}\}]$, that only depends on the quasipotentials $\mathcal{V}$, and an external part $\Delta S_{\mathrm{Ext}}[\{\boldsymbol{X}\}]$, which depends on the actions $\mathbb{A}$,

$$\begin{aligned}
\Delta S[\{\boldsymbol{X}\}] &= \Delta S_{\mathrm{Int}} + \Delta S_{\mathrm{Ext}} \\
\epsilon\Delta S_{\mathrm{Int}}[\{\boldsymbol{X}\}] &= \mathcal{V}[\boldsymbol{X}(\tau), \tau] - \mathcal{V}[\boldsymbol{X}(0), 0] \\
\epsilon\Delta S_{\mathrm{Ext}}[\{\boldsymbol{X}\}] &= -\mathbb{A}[\{\boldsymbol{X}\}] + \mathbb{A}[\{\boldsymbol{X}^{\mathrm{R}}\}]
\end{aligned} \tag{5.6}$$

The internal entropy production is the field-theoretic extension of Seifert's entropy production of the system, both of which are the difference between the initial and final quasipotential $\mathcal{V}$ [77]. Seifert's argument for the connection to Gibbs entropy also carries through: taking the ensemble average of ΔS_{Int},

$$\begin{aligned}
\langle\Delta S_{\mathrm{Int}}\rangle &= \frac{1}{\epsilon}\left\langle\mathcal{V}(\tau)\right\rangle_{\mathcal{P}(\tau)} - \frac{1}{\epsilon}\left\langle\mathcal{V}(0)\right\rangle_{\mathcal{P}(0)} \\
&= -\int\prod_{\alpha}\mathcal{D}X_{\alpha}\left[\mathcal{P}(\tau)\log\mathcal{P}(\tau)\right] + \int\prod_{\alpha}\mathcal{D}X_{\alpha}\left[\mathcal{P}(0)\log\mathcal{P}(0)\right] + C
\end{aligned} \tag{5.7}$$

where C is a constant and $\int\prod_{\alpha}\mathcal{D}X_{\alpha}$ represents the integration over all configurations of $\boldsymbol{X}$. Observe that the last two terms are the Gibbs entropy of the final and the initial configurations respectively, implying that $\langle\Delta S_{\mathrm{Int}}\rangle$ can be interpreted as the change in the (system) Gibbs entropy.

On the other hand, the meaning of the external entropy production is less clear, though the choice is unique once the internal part of the entropy production is identified. For the example of an over-damped particle introduced in Seifert's paper [77], the external entropy

production can be directly related to the heat dissipated in the bath. However, the coarse graining of the particle dynamics into field trajectories changes the amount of information tracked, and hence the observed entropy production [31]. As a consequence, any direct link between the entropy production and physical, as opposed to informatic, quantities can only be established in a model-specific way [81], if such interpretations exist at all. We would like to note that we are addressing the informatic view of entropy production in this work, rather than heat flow, and we refer to Markovich et al. for treatments of the latter in field theories [83]. The distinction between these two views of the entropy production rate (EPR) is fully discussed in a recent review article [84] which introduces the term 'informatic EPR' or IEPR for the former. In that language, all the EPR's discussed below are IEPRs.

Going back to the calculation, the instantaneous internal (resp. external) entropy production rate (EPR) can be obtained by differentiating the internal (resp. external) entropy production with respect to the final time τ. The expression for the general case is rather cumbersome and not particularly enlightening, so we will only present the formula for the choices of $\boldsymbol{X}$ of our interest. Note that our approach is consistent with the method in Nardini et al. [32]: S in equation (16) of their paper corresponds to our ΔS_{Ext}, but as they subsequently divide by τ and take $\tau \to \infty$ in their definition of the EPR, the internal entropy production ΔS_{Int}, an $O(\tau^0)$ piece, vanishes in the process.

Having developed a general scheme for calculating the entropy production rate of stochastic trajectories, we proceed to introduce the specific class of systems that the formulation will be applied to in the remainder of this chapter.

5.2 Scalar Langevin systems

In this chapter we focus our attention on scalar Langevin systems with additive white noise. Extensions to vectorial systems or systems with multiplicative noise are possible but bring additional complications [82], which we will not discuss here. In this section, we will first write down the most general form, and follow with some examples, including relaxational models (as defined in Tauber et al. [52]) and their non-equilibrium extensions. We will also re-introduce non-equilibrium Model AB for phase-separating systems with additional chemical reactions.

Consider a scalar field ϕ, which can be the (rescaled) density of some particles or the composition variable of a binary fluid. The most general form of Langevin dynamics is,

$$\begin{aligned} \partial_t \phi &= F(\phi) + \sqrt{2\epsilon}\sigma\Lambda \\ \langle \Lambda(\boldsymbol{x}, t)\Lambda(\boldsymbol{y}, s)\rangle &= \delta(\boldsymbol{x} - \boldsymbol{y})\delta(t - s) \end{aligned} \tag{5.8}$$

where $F(\phi)$ is the deterministic dynamics (not to be confused with free energy, which

we denote as $\mathcal{F}[\phi]$ as will be specified later), Λ is a spatial-temporal white noise, σ is an operator independent of ϕ (to be defined later) and ϵ characterises the noise strength. We note that ϵ is the same as the previously mentioned constant in the definition of the rate function, the action and the quasipotential in equation (5.2, 5.4). In equilibrium thermodynamics, $\epsilon = k_{\mathrm{B}}T$, whose role is usually singled out by convention and not absorbed in the definition of quantities such as free energy.

Before we define σ, we take a detour to introduce the notations we use for fields and operators in this chapter. Adopting the notation from linear algebra, we treat the scalar field ϕ as an infinite-dimensional column vector and define its adjoint $\phi^\dagger$ as the corresponding row vector. This enables us to proceed in a basis-independent way and only refer to a specific basis (such as real space or Fourier space) when needed. The inner product between scalar fields ϕ and ψ, denoted as $\phi^\dagger\psi$, is the sum of the products of their elements with respect to some orthogonal basis: $\phi^\dagger\psi = \sum_{i=1}^{\infty} \phi_i^*\psi_i$. For example, in real space $\phi^\dagger\psi = \int \mathrm{d}\boldsymbol{x}\, \phi(\boldsymbol{x})\psi(\boldsymbol{x})$, assuming $\psi(\boldsymbol{x}), \phi(\boldsymbol{x})$ are real; in Fourier space the inner product is $(2\pi)^{-d}\int \mathrm{d}\boldsymbol{q}\, \phi(-\boldsymbol{q})\psi(\boldsymbol{q})$ (note we take the Fourier transform convention $\phi(\boldsymbol{x}) = (2\pi)^{-d}\int \mathrm{d}\boldsymbol{q}\phi(\boldsymbol{q})\exp(-i\boldsymbol{x}\cdot\boldsymbol{q})$ in d dimensions). We can similarly define the outer product in an element-wise way, $(\phi\psi^\dagger)_{ij} = \phi_i\psi_j^*$, naturally extending from vectors to matrices. The operation of matrix O on vector ϕ is defined in the usual way as $(O\phi)_i = \sum_{j=0}^{\infty} O_{ij}\phi_j$. This leads to the definition of the adjoint of a matrix, denoted as $O^\dagger$, defined element-wise as $O^\dagger_{ij} = O^*_{ji}$, with the property that $\phi^\dagger(O\psi) = (O^\dagger\phi)^\dagger\psi$.

With these notations, σ is, in general, an infinite-dimensional matrix that is not a function of ϕ, as we assumed that the noise is not multiplicative. The spatial-temporal noise Λ is a vector and its correlation can be denoted by an outer product: $\left\langle \Lambda(t)\Lambda(s)^\dagger \right\rangle = I\delta(t-s)$ where I is the identity, e.g. in real space I is the delta function $\delta(\boldsymbol{x}-\boldsymbol{y})$. Letting $\eta(t) = \sigma\Lambda(t)$, the correlation of η is

$$\left\langle \eta(t)\eta^\dagger(s) \right\rangle = \left\langle (\sigma\Lambda(t))(\sigma\Lambda(s))^\dagger \right\rangle = \sigma\sigma^\dagger\delta(t-s) \equiv K\delta(t-s) \tag{5.9}$$

where we have defined $K = \sigma\sigma^\dagger$, commonly known as the noise kernel. Crucially, σ is only defined so far as $\sigma\sigma^\dagger$ yields the desired noise kernel K, because noises with the same mean and correlation are indistinguishable [54]. For convenience we will always choose a specific form of σ with the understanding that many other choices are equivalent, as will be illustrated in the next section.

5.2.1 Relaxational models and non-equilibrium modifications

A well-studied subclass of scalar Langevin dynamics consists of the relaxational models systematically catalogued in Hohenberg and Halperin's review [21] that describes the dynamical approach to equilibrium, adopting a top-down method that classifies models

based on the symmetries and conservation laws. For a single scalar field, the dynamics is named Model B if the ϕ field is conserved locally (i.e. $\partial_t \phi = -\boldsymbol{\nabla} \cdot \boldsymbol{J}$ for some current $\boldsymbol{J}$) or Model A for the non-conservative case. With the formalism introduced in the previous section, Model A and Model B can be concisely written down as follows (the noise kernels are diagonal in Fourier space so only the diagonal elements are presented),

$$K_{\mathrm{X}}(\boldsymbol{q}) = M_{\mathrm{X}} |\boldsymbol{q}|^{2\lambda_{\mathrm{X}}}, \qquad F_{\mathrm{X}} = -K_{\mathrm{X}} \frac{\delta \mathcal{F}_{\mathrm{X}}}{\delta \phi}, \qquad \text{for X} = \mathrm{A}, \mathrm{B} \tag{5.10}$$

where M_{X} is a mobility constant and $\lambda_{\mathrm{A}} = 0, \lambda_{\mathrm{B}} = 1$. Alternatively, we can write the noise kernel in real space: $K_{\mathrm{X}} = M_{\mathrm{X}}(i\nabla)^{2\lambda_{\mathrm{X}}}$, which is no longer diagonal (see 5.C for the explicit form of the discrete Laplacian operator on a lattice). As discussed before, the σ matrix is ambiguous, and here we choose it to also be diagonal in Fourier space with elements $\sigma_{\mathrm{X}}(\boldsymbol{q}) = M_{\mathrm{X}}(-i|\boldsymbol{q}|)^{\lambda_{\mathrm{X}}}$. The factor of $-i$ in the definition of σ is picked such that in 1D, $\sigma_{\mathrm{B}} = \sqrt{M_{\mathrm{B}}}\partial_x$. We do note that the more popular representation of noise in Model B is $\boldsymbol{\nabla} \cdot \boldsymbol{\Lambda}$ where $\boldsymbol{\Lambda}$ is a vectorial white noise. This is equivalent to our definition here because $(-i\boldsymbol{q} \cdot \boldsymbol{\Lambda}(\boldsymbol{q}))$ has the same noise correlation as $(-i|\boldsymbol{q}|\Lambda(|\boldsymbol{q}|))$, where λ is a scalar white noise.

For both Model A and Model B, it can be shown that the Fokker-Planck equation for the probability $\mathcal{P}[\phi, t]$ evolves towards the Boltzmann distribution with free energy $\mathcal{F}_{\mathrm{X}}[\phi]$ and temperature $k_{\mathrm{B}}T = \epsilon$. These free energies are generally chosen to be of ϕ^4 square-gradient form – see next section. Furthermore, the system has time reversal symmetry and the $(\phi, \partial_t \phi)$ trajectories obey the principle of detailed balance: the probability of observing a trajectory is the same as the probability of observing the same trajectory in reverse [85–87]. In fact, the same conclusions hold for any sufficiently well-behaved K, as long as there is a "chemical potential" μ such that (i) $F = -K\mu$ and (ii) μ can be written as a functional derivative of some free energy $\mathcal{F}$.

These relaxational models can be extended to non-equilibrium in a 'minimal' way by adding terms that cannot be absorbed via a modification of the free energy (i.e. $\mu \neq \delta_\phi \mathcal{F}$). In particular, in systems with conservation law, we can add a driving term $\boldsymbol{E}(\phi, x)$ to Model B,

$$\partial_t \phi = M_{\mathrm{B}} \boldsymbol{\nabla} \cdot \left(\boldsymbol{\nabla} \frac{\delta \mathcal{F}_{\mathrm{B}}}{\delta \phi} - \boldsymbol{E} \right) + \sqrt{2\epsilon} \sigma_{\mathrm{B}} \Lambda \tag{5.11}$$

As long as $\boldsymbol{E}$ cannot be written as $(-\boldsymbol{\nabla}\mu)$ for some truly integrable chemical potential μ, the system no longer obeys detailed balance and there is no time reversal symmetry [6, 33]. There is generically no analytical solution for the steady state distribution, though in a few special settings it is possible to map back to an equilibrium system. One such example is a 1D system with periodic boundary conditions and $E = \gamma\phi$, modelling interacting

particles driven around a ring by a constant force parallel to the ring[1]. After a Galilean transformation $\phi(x,t) \to \phi(x - M_{\rm B}\gamma t, t)$, the equation is identical to Model B, hence the steady state quasipotential $\mathcal{V}_{\rm ss}$ is the same as the free energy $\mathcal{F}_{\rm B}$ in this case.

A popular choice in active matter literature is to make $\boldsymbol{E}$ depend on ϕ in a way that breaks the time reversal symmetry to lowest order in ϕ and $\boldsymbol{\nabla}$ [6, 11, 12]. For mass-conserving systems, the lowest order terms are $\boldsymbol{E}(\phi) = \lambda\boldsymbol{\nabla}|\boldsymbol{\nabla}\phi|^2 + \zeta(\boldsymbol{\nabla}\phi)(\nabla^2\phi)$, named Active Model B+ in Tjhung et al. [11] (the third term of $O(\nabla^3\phi^2)$ can be absorbed into the free energy if λ and ζ are also adjusted). The former, the λ-term, is a gradient of a local chemical potential $\lambda|\boldsymbol{\nabla}\phi|^2$, which cannot be written as a functional derivative of any free energy. The latter, the ζ-term, leads to macroscopic steady state current, though only its curl-free piece contributes to the ϕ-dynamics as argued in Tjhung et al. [11]. We will expand upon this argument when we look at the entropy production of non-equilibrium systems with conservation laws.

5.2.2 Non-equilibrium Model AB

Another way of breaking time reversal symmetry is to combine two equilibrium dynamics with different free energies [1, 7, 22–24, 37, 45, 58, 59]. Model AB, constructed in chapter 2 from Model B and Model A, represents systems with one scalar field ϕ, subject to *separate* diffusive and reactive dynamics, such as binary fluids with non-equilibrium chemical reactions and active particles with population dynamics. Recall from equation (2.3) in chapter 2 the dynamics of Model AB and rewrite the Model B sector in the notation of equation (5.10),

$$\begin{aligned} \partial_t\phi &= \partial_t\phi_{\rm A} + \partial_t\phi_{\rm B} \\ \partial_t\phi_{\rm A} &= -M_{\rm A}\mu_{\rm A}(\phi) + \sqrt{2\epsilon M_{\rm A}}\Lambda_{\rm A} \\ \partial_t\phi_{\rm B} &= -K_{\rm B}\mu_{\rm B}(\phi) + \sqrt{2\epsilon}\sigma_{\rm B}\Lambda_{\rm B} \end{aligned} \tag{5.12}$$

where $\Lambda_{\rm A}, \Lambda_{\rm B}$ are independent unit white noises and recall that $\sigma_{\rm B}(\boldsymbol{q}) = -i|\boldsymbol{q}|\sqrt{M_{\rm B}}$, $K_{\rm B}(\boldsymbol{q}) = M_{\rm B}|\boldsymbol{q}|^2$. The two chemical potentials $\mu_{\rm A,B}$ are not necessarily functional derivatives of free energies $\mathcal{F}_{\rm A,B}$. For simplicity, we assume here, as in chapters 2 and 3, that they are, but allow $\mathcal{F}_{\rm A} \neq \mathcal{F}_{\rm B}$. This is enough to break time-reversal symmetry, and generically does so at lower order in (∇, ϕ) than the terms needed to break the symmetry in either sector by itself.

Although this set of equations appears different from equation (5.8) at first sight, they can be rewritten in that form by combining the two Gaussian noises into one. Let

[1]The full stochastic PDE for such a system would be $\partial_t\rho = \partial_x\left[D\rho\left(\partial_x\mu + \gamma\right) + \sqrt{2D\rho}\Lambda\right]$. Perturb around some constant density $\rho = \rho_0(1+\phi)$ and we get the one written here once we omit the ϕ-dependence in the mobility.

$\eta = \sqrt{M_\mathrm{A}}\Lambda_\mathrm{A} + \sigma_\mathrm{B}\Lambda_\mathrm{B}$ and we want to find a suitable σ such that $\eta = \sigma\Lambda$ for a unit white noise Λ. As argued in section 5.2, σ can be found by effectively 'square rooting' the noise kernel K, which is also the spatial factor[2] of the noise correlation $\langle \eta(t)\eta^\dagger(s)\rangle$,

$$\begin{aligned}\langle \eta(t)\eta(s)^\dagger\rangle &= M_\mathrm{A}\langle \Lambda_\mathrm{A}(t)\Lambda_\mathrm{A}(s)^\dagger\rangle + M_\mathrm{B}\left\langle (\sigma\Lambda_\mathrm{B}(t))\,(\sigma\Lambda_\mathrm{B}(s))^\dagger\right\rangle \\ &= \left(M_\mathrm{A}I - M_\mathrm{B}\nabla^2\right)\delta(t-s)\end{aligned} \tag{5.13}$$

where we have used the fact that the two noises $\Lambda_{\mathrm{A,B}}$ are independent. We can now read off the noise kernel $K = M_\mathrm{A}I - M_\mathrm{B}\nabla^2$, which is diagonal in Fourier space with elements $K(\boldsymbol{q}) = M_\mathrm{A} + M_\mathrm{B}|\boldsymbol{q}|^2$. Choosing σ to also be diagonal in Fourier space for convenience, then $\sigma(\boldsymbol{q})$ can be any complex root of $K(\boldsymbol{q})$. Here we set $\sigma(\boldsymbol{q}) = \sqrt{M_\mathrm{A}} - i|\boldsymbol{q}|\sqrt{M_\mathrm{B}}$, such that in 1D, $\sigma(x) = \sqrt{M_\mathrm{A}} + \sqrt{M_\mathrm{B}}\partial_x$. Collecting the terms, in the form of equation (5.8), Model AB can be written as,

$$\partial_t\phi = M_\mathrm{B}\nabla^2\mu_\mathrm{B} - M_\mathrm{A}\mu_\mathrm{A} + \sqrt{2\epsilon}\sigma\Lambda \tag{5.14}$$

We showed in chapter 2 that there is a special subspace where the ϕ-dynamics is effectively equilibrium. Since K is non-singular (it is diagonal in Fourier space with nonzero eigenvalues), the inverse exists and we can always find $\mu = -K^{-1}F = \mu_\mathrm{B} + M_\mathrm{A}K^{-1}(\mu_\mathrm{A} - \mu_\mathrm{B})$. As discussed in the section 2.2, if there exists a $\mathcal{F}$ that has this μ as its functional derivative, time reversal symmetry will be restored for the ϕ field. This includes the trivial "true equilibrium" case: $\mu_\mathrm{A} = \mu_\mathrm{B}$, where the phase separation and the chemical reactions are governed by same underlying equilibrium chemical potentials [7].

A more general sufficient condition is when $\mu_\mathrm{B} - \mu_\mathrm{A} = KQ\phi$ for any self-adjoint matrix Q independent of ϕ, such that the overall free energy $\mathcal{F} = \mathcal{F}_\mathrm{B} + \frac{1}{2}\phi^\dagger Q\phi$. For systems of our interest, the diffusive dynamics, controlled by μ_B, drives conservative phase separation. Then the simplest choices for $\mu_{\mathrm{B,A}}$ (lowest order in ϕ and ∇) that has an equilibrium subspace are, as previously described in section 2.2,

$$\begin{aligned}\mu_\mathrm{B} &= c - \alpha\phi + \beta\phi^3 - \kappa\nabla^2\phi \\ \mu_\mathrm{A} &= c + \alpha'\phi + \beta'\phi^3\end{aligned} \tag{5.15}$$

where $\alpha, \beta, \kappa, \alpha', \beta'$ are positive constants and c can take either sign (the constant terms can be taken to be the same w.l.o.g. as the constant term in μ_B has no effect on the dynamics) . Observe that when $\beta = \beta'$, $\mu_\mathrm{B} - \mu_\mathrm{A} = (\alpha + \alpha')\phi - \kappa\nabla^2\phi$, which is linear in ϕ with self-adjoint linear operator $Q(\boldsymbol{q}) = K(\boldsymbol{q})^{-1}\left[(\alpha + \alpha') - \kappa|\boldsymbol{q}|^2\right]$. This gives us a continuous parameter β' that we can tune to bring the system in and out of the

[2]the spatial-temporal correlation factorises into spatial and temporal contributions as shown in the equation below.

equilibrium subspace without dramatically changing the phenomena exhibited. On its own, the Model B sector favours conservative bulk phase separation with the double-well free energy $\mathcal{F}_{\mathrm{B}} = \int \mathrm{d}\boldsymbol{x} \left[-\frac{1}{2}\alpha\phi^2 + \frac{1}{4}\beta\phi^4 + \frac{1}{2}\kappa|\boldsymbol{\nabla}\phi|^2\right]$, whereas the Model A sector describes non-conservative relaxation towards some fixed target density ϕ_{t}. In chapter 3, we surveyed the parameter space of this class of models and found two stable stationary solutions: uniform solution and arrested phase separation. The uniform state is observed for small M_{A}, where the local nonconservative relaxations overcome the phase separating diffusive dynamics, fixing the density at the target density ϕ_{t} of the reactions. After crossing over some critical value of M_{A}, the conservative sector dominates and finite domains of alternating phases are formed, as shown schematicallyin figure 2.1. The length scale of the pattern is determined by the balance of the reactions in the two phases and the steady state current transporting matter across the interface. Interestingly, the information on these macroscopic currents is not available unless we are able to track the Model B and Model A dynamics separately, i.e. distinguishing $\partial_t\phi_{\mathrm{A}}$ from $\partial_t\phi_{\mathrm{B}}$ in equation (5.12). This has profound consequences for the entropy production rate as we will see later.

5.3 Entropy production rate for $(\phi, \partial_t\phi)$

For general scalar Langevin systems, a natural choice is to track the $(\phi, \partial_t\phi)$ trajectories. In this section, we work towards a general expression for the instantaneous entropy production rate (EPR) and show that it is non-negative for every ϕ-configuration in steady state. In addition, we find a non-negative local decomposition of the EPR and discuss its physical interpretations with various examples. Lastly we apply the method to Model AB and, with that as a case study, demonstrate that the EPR can be calculated to lowest order in ϵ for any Langevin system.

Recall from section (5.1) that the entropy production can be split into an internal part and an external part. We will calculate the external entropy production first, which is the difference between the action of the forward and the backward path as shown in equation (5.6). The action for the $(\phi(x,t), \partial_t\phi(x,t))_{t\in[0,\tau]}$ trajectories of a general Langevin system (see equation (5.8)) is an Onsager-Machlup functional [88],

$$\mathbb{A}[\phi, \partial_t\phi] = \frac{1}{4}\int_0^\tau \mathrm{d}t \left[(\partial_t\phi - F)^\dagger K^{-1}(\partial_t\phi - F) + \mathcal{G}[\phi]\right] \tag{5.16}$$

where $\mathcal{G}[\phi]$ is a piece specific to Stratonovich discretisation that is only a functional of ϕ (rather than $\partial_t\phi$) [32]. In our vector notations, $\mathcal{G}[\phi] = 2\epsilon\,\mathrm{Tr}[\delta_\phi F]$ (here $\delta_\phi F$ is a matrix as F and ϕ are both vectors), which in real space is represented by the integral $2\epsilon\int \mathrm{d}\boldsymbol{x}\frac{\delta F(\boldsymbol{x})}{\delta\phi(\boldsymbol{x})}$ [82]. The reversed ϕ-path is the direct time reversal of the forward path $\phi^{\mathrm{R}}(t) = \phi(\tau - t)$, and we differentiate ϕ^{R} with respect time to get $\partial_t\phi^{\mathrm{R}}(t) = -\partial_s\phi(s)|_{s=\tau-t}$. Hence the action for

the reversed trajectories is,

$$\mathbb{A}[\phi^{\mathrm{R}}, \partial_t \phi^{\mathrm{R}}] = \frac{1}{4}\int_0^\tau \mathrm{d}t \left[(-\partial_t\phi - F)^\dagger K^{-1}(-\partial_t\phi - F) + \mathcal{G}[\phi]\right] \tag{5.17}$$

Note that the additional piece $\mathcal{G}[\phi]$ remains the same, as it does not depend on $\partial_t\phi$. Collecting the two results, the external entropy production and its time derivative (the external EPR) are

$$\begin{aligned} \Delta S_{\mathrm{Ext}} &= -\mathbb{A}[\phi, \partial_t\phi] + \mathbb{A}[\phi^{\mathrm{R}}, \partial_t\phi^{\mathrm{R}}] = \frac{1}{\epsilon}\int_0^\tau \mathrm{d}t\, \partial_t\phi^\dagger K^{-1} F(\phi) \\ \epsilon \dot{S}_{\mathrm{Ext}}(t) &= \partial_t\phi^\dagger K^{-1} F(\phi) \end{aligned} \tag{5.18}$$

Next, we take the time derivative of the internal entropy production, which will later be added to $\dot{S}_{\mathrm{Ext}}(t)$ to give the total EPR. As the starting and end points of the trajectories do not depend on $\partial_t\phi$, the internal entropy production is only a function of ϕ: $\epsilon\Delta S_{\mathrm{Int}} = \mathcal{V}[\phi(\tau), \tau] - \mathcal{V}[\phi(0), 0]$. Differentiating with respect to τ along the trajectories and relabelling τ to t [27],

$$\epsilon \dot{S}_{\mathrm{Int}}(t) = \partial_t\phi^\dagger \frac{\delta \mathcal{V}}{\delta \phi} + \partial_t \mathcal{V} \tag{5.19}$$

The first term is the change in quasipotential as a result of moving along the trajectory whereas the second comes from the intrinsic time dependence of the probability distribution. Combining the internal and external terms, we obtain (see also [80]),

$$\epsilon \dot{S} = \partial_t \mathcal{V} + \partial_t\phi^\dagger K^{-1}\left(F(\phi) + K\frac{\delta \mathcal{V}}{\delta \phi}\right) \equiv \partial_t \mathcal{V} + \partial_t\phi^\dagger K^{-1} F_{\mathrm{a}}(\phi) \tag{5.20}$$

where we have defined a new variable $F_{\mathrm{a}} = F + K\frac{\delta \mathcal{V}}{\delta \phi}$ and the subscript "a" denotes that it is the antisymmetric component of the dynamics, as will be explained in the next section. In Stratonovich discretisation, the conditional expectation of $\partial_t\phi$ given the field configuration ϕ at time t is $\langle \partial_t\phi | \phi, t\rangle = F_{\mathrm{a}}(\phi)$ (see appendix 5.A for the precise definition of the conditional expectation and details of the calculation) [27, 77]. Averaging over $\partial_t\phi$ of the trajectory, we find that for each state ϕ (rather than trajectory $\phi(t)_{t\in[0,\tau]}$), the instantaneous entropy production rate is,

$$\epsilon \dot{S}[\phi] = \partial_t \mathcal{V} + F_{\mathrm{a}}^\dagger K^{-1} F_{\mathrm{a}} \tag{5.21}$$

There are two important observations: (1) If we take the ensemble average over the probability distribution $\mathcal{P}(t)$, the first term becomes $\int \mathcal{D}\phi\, \partial_t \mathcal{P}[\phi, t]$ which sums to zero by the conservation of probability [27, 77]. Thus the ensemble entropy production rate is always non-negative, consistent with the Second Law. (2) In steady state $\partial_t \mathcal{V} = 0$, as a

result, the instantaneous EPR $\dot{S}_{\rm ss}$ is non-negative for any field configuration,

$$\epsilon \dot{S}_{\rm ss} = F_{\rm a}^\dagger K^{-1} F_{\rm a} \tag{5.22}$$

Note that this does not imply that individual *trajectories* with negative entropy production do not exist, as the non-negative quantity $\dot{S}[\phi]$ is the entropy production associated with each field configuration, which we obtained by averaging over $\langle \partial_t \phi | \phi \rangle$.

The non-negativity of the steady state EPR can be proved by further decomposing $\dot{S}_{\rm ss}$ as a sum of non-negative elements in a basis-independent way: $\dot{S}_{\rm ss} = \epsilon^{-1} \sum_i |Y_i|^2 \equiv \epsilon^{-1} Y^\dagger Y$ for $|Y| = |\sigma^{-1} F_{\rm a}|$ (only the magnitude of Y is important but not its phase or direction, e.g. $Y = \pm \sigma^{-1} F_{\rm a}$ gives the same decomposition in any basis). In particular, this gives a non-negative spatial decomposition $\dot{s}(\boldsymbol{x}) = \epsilon^{-1} |Y(\boldsymbol{x})|^2$ such that $\dot{S}_{\rm ss} = \int {\rm d}\boldsymbol{x} \dot{s}(\boldsymbol{x})$ and $|Y|$ in real space plays an analogous role as the antisymmetric current in Macroscopic Fluctuation Theory [33] as we will see later. However, we would like to emphasise that it is not a *unique* local decomposition (e.g. $\epsilon^{-1} F_{\rm a}(\boldsymbol{x})(K^{-1} F_{\rm a})(\boldsymbol{x})$ gives the same result upon spatial integration) and *a priori* there is no reason to choose one over the other. The choice of $\dot{s}(\boldsymbol{x})$ is singled out by the fact that it guarantees non-negative local decomposition.

5.3.1 The antisymmetric component $F_{\rm a}$

Roughly speaking, $F_{\rm a}$ $(= F + K \frac{\delta \mathcal{V}}{\delta \phi})$ is the time antisymmetric part of the deterministic evolution; the rigorous version of this statement requires the introduction of the adjoint dynamics. Define the adjoint Fokker-Planck equation such that the time evolution of the probability under the adjoint Fokker-Planck is the same as the forward probability evolution run backwards. Mathematically, this means $\mathcal{P}^{\rm R}(\tau - t) = \mathcal{P}(t)$, where $\mathcal{P}^{\rm R}$ is the solution of the adjoint Fokker-Planck equation. Note that the final conditions of $\mathcal{P}(t)$ would be the initial conditions of $\mathcal{P}^{\rm R}(\tau - t)$. Following [33], we assume that the adjoint system is also of Langevin type and has the same noise kernel. We want to find the deterministic adjoint dynamics $F^{\rm R}$.

Starting with the Fokker-Planck equation for the forward probability distribution $\mathcal{P}[\phi, t]$, omitting the dependence on ϕ to ease notation,

$$\partial_t \mathcal{P}(t) = \delta_\phi^\dagger (F - \epsilon K \delta_\phi) \mathcal{P}(t) \tag{5.23}$$

where δ_ϕ denotes functional derivative with respect to the ϕ-field, which behaves like a vector. On the other hand, the adjoint Fokker-Planck equation is

$$\partial_{t'} \mathcal{P}^{\rm R}(t') = \delta_\phi^\dagger \left(F^{\rm R} - \epsilon K \delta_\phi \right) \mathcal{P}^{\rm R}(t') \tag{5.24}$$

Enforcing the condition that $\mathcal{P}^{\rm R}(\tau - t) = \mathcal{P}(t)$, we must have $t' = \tau - t$ and, by the chain

rule, $\partial_{t'} P^{\mathrm{R}}(t') = -\partial_t \mathcal{P}^{\mathrm{R}}(\tau - t) = -\partial_t \mathcal{P}(t)$. Substituting into the adjoint Fokker-Planck equation and rearranging the terms into a drift term and noise term (remember that we assumed the noise kernel of the adjoint process to the be same), we obtain

$$\partial_t \mathcal{P}(t) = \delta_\phi^\dagger[(2\epsilon K \delta_\phi \log(\mathcal{P}(t)) - F^{\mathrm{R}})\mathcal{P}(t) - \epsilon K \delta_\phi \mathcal{P}(t)] \tag{5.25}$$

Comparing the above with equation (5.23), we can see that the noise terms are the same and the equations will be identical if the drift terms are matched. Recall that $\mathcal{P} \propto \exp(-\epsilon^{-1}\mathcal{V})$, we obtain an expression for F^{R} in terms of the forward dynamics,

$$F^{\mathrm{R}}(\phi, t) = -2K\delta_\phi \mathcal{V}[\phi, t] - F(\phi) \tag{5.26}$$

This naturally leads to the definitions of the symmetric and antisymmetric components $F_{\mathrm{s,a}} \equiv (F \pm F^{\mathrm{R}})/2$,

$$F_{\mathrm{s}} = -K\frac{\delta \mathcal{V}}{\delta \phi}, \quad F_{\mathrm{a}} = F + K\frac{\delta \mathcal{V}}{\delta \phi} \tag{5.27}$$

Note that the forward Fokker-Planck equation needs to be solved to obtain the adjoint dynamics as it requires the value of $\mathcal{V}(t)$ at every instant in time. However, the situation simplifies in steady state where $\mathcal{V}$ remains invariant. Then F_{s} describes the descent to the minimum of the quasipotential, whereas F_{a} characterises the excess driving that maintains the system away from equilibrium. It is not surprising that the entropy production in steady state is only a function of F_{a} – both the entropy production and F_{a} quantify the amount of time reversal symmetry breaking in the system and both vanish in equilibrium.

5.3.2 Connections to Macroscopic Fluctuation Theory

Our decomposition of F into the symmetric and antisymmetric parts $F_{\mathrm{a,s}}$ in equation (5.27) is similar to the decomposition of the diffusive current $\boldsymbol{J}$ in Macroscopic Fluctuation Theory (MFT) literature [33]: $\boldsymbol{J}_{\mathrm{s}} = -\boldsymbol{\nabla}\partial_\phi \mathcal{V}_{\mathrm{ss}}, \boldsymbol{J}_{\mathrm{a}} = \boldsymbol{J} + \boldsymbol{\nabla}\partial_\phi \mathcal{V}_{\mathrm{ss}}$. While our derivation in section (5.3.1) relies on the reversal of the Fokker-Planck equation, in MFT the "adjoint dynamics" is defined for the action of each path: the probability of observing the reversed path in the MFT-"adjoint dynamics" is the same as the probability of the forward path in the forward dynamics. In this section, we ask the following question: is the adjoint dynamics in our definition equivalent to the MFT definition?

Denote the rate function of the adjoint dynamics as $\mathbb{R}^{\mathrm{R}}$, the rate function of the reversed path is,

$$\begin{aligned}\mathbb{R}^{\mathrm{R}}\left[(\phi^{\mathrm{R}}, \partial_t \phi^{\mathrm{R}})_{t\in[0,T]}\right] = \frac{1}{4}\int \mathrm{d}t\ \left[(-\partial_t\phi - F^{\mathrm{R}})^\dagger K^{-1}(-\partial_t\phi - F^R) + 2\epsilon \mathrm{Tr}\left(\delta_\phi F^{\mathrm{R}}\right)\right] \\ + \mathcal{V}[\phi(T), T]\end{aligned}$$

where F^{R} ($= -F - 2K\delta_\phi \mathcal{V}$) is the reversed dynamics we found in section (5.3.1) by reversing the Fokker-Planck equation. If $\mathbb{R}^{\mathrm{R}}\left[(\phi^{\mathrm{R}}, \partial_t \phi^{\mathrm{R}})_{t\in[0,T]}\right] = \mathbb{R}\left[(\phi, \partial_t\phi)_{t\in[0,T]}\right]$, our definition of the adjoint dynamics gives path-wise reversal and therefore would be equivalent to the MFT definition. Taking the difference of the forward and the backward rate functions, we obtain

$$\begin{aligned}\mathbb{R}\left[(\phi, \partial_t\phi)_{t\in[0,T]}\right] - \mathbb{R}^{\mathrm{R}}\left[(\phi^{\mathrm{R}}, \partial_t\phi^{\mathrm{R}})_{t\in[0,T]}\right] = &-\frac{1}{2}\int \mathrm{d}t\, \partial_t\phi^\dagger K^{-1}(F + F^{\mathrm{R}}) \\ &+ \mathcal{V}[\phi(0), 0] - \mathcal{V}[\phi(T), T] \\ &+ \frac{1}{4}\int \mathrm{d}t\, \left[F^\dagger K^{-1} F - (F^{\mathrm{R}})^\dagger K^{-1} F^{\mathrm{R}}\right] \\ &+ \frac{1}{2}\epsilon \int \mathrm{d}t\, \mathrm{Tr}\left[\delta_\phi F - \delta_\phi F^{\mathrm{R}}\right]\end{aligned}$$

Dividing by T and taking the limit $T \to 0$ on both sides,

$$\begin{aligned}\partial_t\mathbb{R} - \partial_t\mathbb{R}^{\mathrm{R}} = &-\frac{1}{2}\partial_t\phi^\dagger K^{-1}(F + F^{\mathrm{R}} + 2K\frac{\delta\mathcal{V}}{\delta\phi}) + \frac{1}{4}\left(F^\dagger K^{-1}F - (F^{\mathrm{R}})^\dagger K^{-1}F^{\mathrm{R}}\right) \\ &- \partial_t\mathcal{V} + \frac{1}{2}\epsilon \mathrm{Tr}\left[\delta_\phi F - \delta_\phi F^{\mathrm{R}}\right]\end{aligned}$$

Substituting in $F^{\mathrm{R}} = -F - 2K\delta_\phi\mathcal{V}$,

$$\partial_t\mathbb{R} - \partial_t\mathbb{R}^{\mathrm{R}} = \frac{1}{4}\left(F^\dagger K^{-1}F - (F^{\mathrm{R}})^\dagger K^{-1}F^{\mathrm{R}}\right) - \partial_t\mathcal{V} + \frac{1}{2}\epsilon\mathrm{Tr}\left[\delta_\phi F - \delta_\phi F^{\mathrm{R}}\right]$$

Or in terms of the symmetric and the antisymmetric dynamics defined as $F_{\mathrm{s,a}} = \left(F \pm F^{\mathrm{R}}\right)/2$,

$$\partial_t\mathbb{R} - \partial_t\mathbb{R}^{\mathrm{R}} = F_{\mathrm{s}}^\dagger K^{-1} F_{\mathrm{a}} - \partial_t\mathcal{V} + \epsilon\mathrm{Tr}\left[\delta_\phi F_{\mathrm{a}}\right]$$

In MFT, the adjoint dynamics is defined for the steady state only ($\partial_t\mathcal{V} = 0$) and in the limit $\epsilon \to 0$. This gives $\partial_t\mathbb{R} - \partial_t\mathbb{R}^{\mathrm{R}} = F_{\mathrm{s}}^\dagger K^{-1}F_{\mathrm{a}}$, so if F_{s} and F_{a} are orthogonal, the adjoint dynamics becomes the path-wise reversal of the forward dynamics and the two definitions become equivalent. Thus we have shown equivalence of the definition of the adjoint dynamics used in this chapter to the previous definition used in MFT subject to the orthogonality of F_{s} and F_{a}. It lies beyond our present scope to establish when such orthogonality is actually present beyond the diffusive systems in [33], corresponding to Model B and its extensions addressed in section 5.2.1.

5.3.3 Entropy production in equilibrium

When the principle of detailed balance holds, the probability of observing a path is the same as the probability of observing the reversed path: $\mathbb{R}[\{\boldsymbol{X}\}] = \mathbb{R}[\{\boldsymbol{X}^{\mathrm{R}}\}]$ [85]. So we

expect the total entropy production ΔS of any trajectory to vanish. In addition, the presence of time reversal symmetry means that all equilibrium systems are self-adjoint. Therefore we expect $F = F^{\mathrm{R}}$, $F_{\mathrm{a}} = 0$ and the instantaneous entropy production rate $\dot{S}[\phi]$ to be zero for all field configurations ϕ.

This can be demonstrated more concretely for the relaxational models introduced in section 5.2. Recall that for this class of systems, $F = -K\frac{\delta \mathcal{F}}{\delta \phi}$ and the stationary measure is the Boltzmann distribution: $\mathcal{V}[\phi] = \mathcal{F}[\phi]$. Thus, for a $(\phi, \partial_t \phi)_{t\in[0,\tau]}$ trajectory, the internal and external entropy productions in steady state (equilibrium) are,

$$\begin{aligned}
\Delta S_{\mathrm{Int}} &= \frac{1}{\epsilon}\left(\mathcal{F}[\phi(\tau)] - \mathcal{F}[\phi(0)]\right) \\
\Delta S_{\mathrm{Ext}} &= -\frac{1}{\epsilon}\int \mathrm{d}t\, \partial_t \phi^\dagger \mu \\
&= -\frac{1}{\epsilon}\int \mathrm{d}t\, \partial_t \phi^\dagger \frac{\delta \mathcal{F}}{\delta \phi} \\
&= -\frac{1}{\epsilon}\left(\mathcal{F}[\phi(\tau)] - \mathcal{F}[\phi(0)]\right)
\end{aligned} \tag{5.28}$$

Observe that the two parts cancel out exactly. The total entropy production ΔS vanishes for each trajectory – the entropy has merely been transferred from the system to the surroundings but the overall value remains the same.

As a consistency check, we can also compute the instantaneous entropy production rate $\dot{S}$ via equation (5.21). Recall from equation (5.27) that $F_{\mathrm{a}} = F + K\frac{\delta \mathcal{V}}{\delta \phi}$, which is identically zero in equilibrium since $\mathcal{V}_{\mathrm{ss}} = \mathcal{F}$. The steady state EPR $\dot{S}_{\mathrm{ss}}$ and its local decomposition $\dot{s}$ are only functions of F_{a} but not F_{s}, hence must both vanish, as expected of time-symmetric dynamics.

5.3.4 Models with mass conservation

Having checked that the entropy production indeed vanishes in equilibrium, we proceed to probe the class of non-equilibrium diffusive systems introduced in section 5.2.1 that breaks time reversal symmetry in a 'minimal' way by adding a driving term to Model B. We will compute the steady state entropy production rate $\dot{S}_{\mathrm{ss}}$ and its non-negative local decomposition $\dot{s}(\boldsymbol{x})$, followed by a discussion of their physical interpretations. For convenience, throughout this section we will omit the subscript 'B' as we only discuss mass-conserving systems.

Recall from section 5.2.1 that the noise kernel K for mass-conserving systems is $-M\nabla^2$, from which we can straight forwardly deduce the antisymmetric component F_{a} and a

formal expression for $\dot{S}_{\rm ss}$

$$\begin{aligned} F_{\rm a} &= F + K\delta_\phi \mathcal{V}_{\rm ss} = M\boldsymbol{\nabla}\cdot[\boldsymbol{\nabla}\left(\mu - \delta_\phi \mathcal{V}_{\rm ss}\right) - \boldsymbol{E}] \\ \dot{S}_{\rm ss} &= \frac{1}{\epsilon M}\int \mathrm{d}\boldsymbol{x}\, F_{\rm a}(\boldsymbol{x})(\nabla^{-2}F_{\rm a})(\boldsymbol{x}) \end{aligned} \tag{5.29}$$

The inverse of the Laplacian operator, denoted as ∇^{-2}, is well defined up to a constant once the boundary conditions are specified. In fact, we can infer that the constant piece must be zero because both $\mathcal{V}$ and $\mathbb{A}$ have no contribution from the $\boldsymbol{q}=0$ mode due to mass conservation, meaning that the entropy production rate cannot have a zero-mode contribution either.

The integrand in the expression for $\dot{S}_{\rm ss}$ gives one spatial decomposition, but that is not the non-negative local EPR $\dot{s}(\boldsymbol{x})$. Recall that $\dot{s}(\boldsymbol{x}) = \epsilon^{-1}|Y(\boldsymbol{x})|^2$, where $|Y| = |\sigma^{-1}F_{\rm a}|$ and $\sigma(\boldsymbol{q}) = -i\sqrt{M}|\boldsymbol{q}|$. The subtleties with $\sigma(\boldsymbol{q}=0)=0$ can again be mitigated by realising that there cannot be a $\boldsymbol{q}=0$ mode in the entropy production rate. For mass-conserving systems, as alluded to in section 5.3.1 and discussed in 5.3.2, $F_{\rm a}$ is closely related to the antisymmetric current $\boldsymbol{J}_{\rm a} = -\boldsymbol{\nabla}\left(\mu - \delta_\phi \mathcal{V}_{\rm ss}\right) + \boldsymbol{E}$ in Macroscopic Fluctuation Theory. In fact, $F_{\rm a} = -\boldsymbol{\nabla}\cdot\boldsymbol{J}_{\rm a}$, which in Fourier space translates to $F_{\rm a}(\boldsymbol{q}) = i\boldsymbol{q}\cdot\boldsymbol{J}_{\rm a}(\boldsymbol{q})$, implying that we can choose $Y(\boldsymbol{q}) = M^{-1/2}\hat{\boldsymbol{q}}\cdot\boldsymbol{J}_{\rm a}$, where $\hat{\boldsymbol{q}} = \boldsymbol{q}/|\boldsymbol{q}|$, with the additional condition that $Y(\boldsymbol{q}=0)=0$. The physical interpretation of this becomes clearer if we decompose $\boldsymbol{J}_{\rm a}$ into a pure gradient piece and a pure curl piece,

$$\boldsymbol{J}_{\rm a} = \boldsymbol{\nabla}\Phi + \boldsymbol{\nabla}\times A \tag{5.30}$$

where Φ is a scalar field and A is a vector field. This is the Helmholtz decomposition, which can always be performed for any vector field: $\Phi = \nabla^{-2}\boldsymbol{\nabla}\cdot\boldsymbol{J}_{\rm a}$, where the inverse Laplacian is well defined as described above. Let the pure gradient part be $\widetilde{\boldsymbol{J}}_{\rm a} = \boldsymbol{\nabla}\Phi$. Since $\widetilde{\boldsymbol{J}}_{\rm a}(\boldsymbol{q}) = -i\boldsymbol{q}\Phi(\boldsymbol{q})$, $\widetilde{\boldsymbol{J}}_{\rm a}$ is in the direction of $\boldsymbol{q}$ while $(\boldsymbol{\nabla}\times\boldsymbol{A})(\boldsymbol{q}) = -i\boldsymbol{q}\times\boldsymbol{A}(\boldsymbol{q})$ is perpendicular to $\boldsymbol{q}$. Therefore

$$|Y(\boldsymbol{q})| = M^{-1/2}|\hat{\boldsymbol{q}}\cdot\boldsymbol{J}_{\rm a}(\boldsymbol{q})| = M^{-1/2}|\widetilde{\boldsymbol{J}}_{\rm a}(\boldsymbol{q})| \tag{5.31}$$

Fourier transform back to real space,

$$\dot{s}(\boldsymbol{x}) = \epsilon^{-1}|Y(\boldsymbol{x})|^2 = (\epsilon M)^{-1}\widetilde{\boldsymbol{J}}_{\rm a}(\boldsymbol{x})\cdot\widetilde{\boldsymbol{J}}_{\rm a}(\boldsymbol{x}) \tag{5.32}$$

In other words, any curl piece (including any constant as this cannot be written as a gradient) in the current gives no contribution to the entropy production rate, which makes sense as the non-gradient part of the current has no effect on the $(\phi, \partial_t\phi)$ trajectories either.

Recall the simple exactly solvable example of particles driven around a 1D ring by a constant force $\boldsymbol{\gamma}$, as discussed in section 5.2. In this case, the steady state probabilities are independent of the driving (i.e. $\mathcal{V}_{\rm ss} = \mathcal{F}$), leading to a clear decomposition of the symmetric and antisymmetric dynamics

$$F_{\rm s} = M\partial_x^2\mu, \quad F_{\rm a} = -M\gamma\partial_x\phi \tag{5.33}$$

The symmetric part controls the descent down the free energy gradient while the antisymmetric part drives the system around the ring. In 1D, the only curl contribution in $J_{\rm a}$ is the constant piece, which we need to subtract off: $\widetilde{J}_{\rm a}(x) = M\gamma(\phi(x) - \bar{\phi})$, where $\bar{\phi}$ is the mean density. Therefore the local entropy production is

$$\dot{s}(x) = \epsilon^{-1}M|\boldsymbol{\gamma}|^2\left(\phi(x) - \bar{\phi}\right)^2 \tag{5.34}$$

Note that the constant circulating current does *not* contribute to EPR at this level because it has no effect on $\partial_t\phi$, whereas deviations in ϕ from the mean density $\bar{\phi}$ are advected by the driving, giving visible TRS breaking in the ϕ dynamics. For more complicated driving, such as Active Model B+, the quasipotential $\mathcal{V}$ is often unknown so it is usually not possible compute the entropy production exactly.

5.3.5 Model AB

Similarly, for Model AB, there is no known solution for the full stochastic dynamics. Nevertheless, one can still write down an expression for the steady state entropy production, assuming that $\mathcal{V}_{\rm ss}$ can at least be approximated. Recall the definition of Model AB from equation (5.14): $\partial_t\phi = M_{\rm B}\nabla^2\mu_{\rm B} - M_{\rm A}\mu_{\rm A} + \sqrt{2\epsilon}\sigma\Lambda$ where $\sigma(\boldsymbol{q}) = \sqrt{M_{\rm A}} - i|\boldsymbol{q}|\sqrt{M_{\rm B}}$. The antisymmetric component in steady state is

$$F_{\rm a} = M_{\rm B}\nabla^2\left(\mu_{\rm B} - \frac{\delta\mathcal{V}_{\rm ss}}{\delta\phi}\right) - M_{\rm A}\left(\mu_{\rm A} - \frac{\delta\mathcal{V}_{\rm ss}}{\delta\phi}\right) \tag{5.35}$$

where as before $\mathcal{V}_{\rm ss}$ is the (unknown) steady state quasipotential. Recall that the local decomposition $\dot{s}(\boldsymbol{x}) = \epsilon^{-1}Y^2$ where $|Y| = |\sigma^{-1}F_{\rm a}|$. Since σ is invertible and diagonal in Fourier space, given $\mathcal{V}_{\rm ss}$, Y can be computed independently for each mode: $|Y(\boldsymbol{q})| = |F_{\rm a}(\boldsymbol{q})/\sigma(\boldsymbol{q})|$. It is possible to then Fourier transform back to real space to obtain an expression for $\dot{s}(\boldsymbol{x})$, but we will not write it out explicitly here as it's both complicated and not particularly enlightening.

5.3.6 Small noise expansion

As we have shown with examples, in general it is extremely rare that one can find an exact analytical expressions for $\dot{S}_{\rm ss}$ or its local decomposition $\dot{s}(\boldsymbol{x})$, as they require the knowledge of $F_{\rm a}$ which in turn depends on an exact solution for the steady state probability distribution (recall that $F_{\rm a} = F + K\frac{\delta \mathcal{V}}{\delta \phi}$ and $\mathcal{P}_{\rm ss} = \exp(-\epsilon^{-1}\mathcal{V}_{\rm ss})$). However, when the noise strength ϵ is small, the stationary distribution is approximately a Gaussian distribution around the deterministic steady state as we will see shortly[3]. As a result, the steady state EPR can be approximated in the small ϵ limit.

The small noise approximation is a standard method for stochastic processes: first expand the scalar field $\phi = \phi_0 + \sqrt{\epsilon}\phi_1 + O(\epsilon)$, then substitute into equation (5.8) and equate the terms to order ϵ^0 and $\epsilon^{1/2}$ separately [54, 55],

$$\begin{aligned} \partial_t \phi_0 &= F(\phi_0) \\ \partial_t \phi_1 &= A(\phi_0)\phi_1 + \sqrt{2}\sigma\Lambda \end{aligned} \tag{5.36}$$

Here $A(\phi_0)$ is the Jacobian "matrix" defined as $A_{ij}(\phi_0) \equiv \delta_{\phi_j} F_i|_{\phi=\phi_0}$. Note that A is a function of ϕ_0 but not ϕ_1. The zeroth order field ϕ_0 captures the deterministic evolution while the ϕ_1 equation corresponds to the Gaussian fluctuation around the deterministic trajectory. Once ϕ_0 has reached its stationary value $\phi_0^{\rm ss}$, the Jacobian A must be negative definite (all eigenvalues negative)[4]. This means ϕ_1 decays exponentially towards a steady state with mean value zero. The steady state correlation of ϕ_1, defined as $C = \left\langle \phi_1 \phi_1^\dagger \right\rangle$, can be calculated using the Lyapunov equation [54, 55],

$$AC + CA^\dagger = -2K \tag{5.37}$$

Once C is known, the steady state quasipotential $\mathcal{V}_{\rm ss}$ can also be obtained to lowest order in ϵ. As ϕ_0 is entirely deterministic, the quasipotential is only a function of the fluctuating field ϕ_1,

$$\mathcal{V}_{\rm ss}[\phi_1] = \frac{\epsilon}{2}\phi_1^\dagger G \phi_1 + O(\epsilon^{3/2}) \tag{5.38}$$

where G is the inverse of C. This holds provided that the system has no continuous symmetry (e.g. translation symmetry if periodic boundary conditions are used); otherwise the additional degree of symmetry has to be explicitly projected out as shown in appendix 5.B so that $G = C^{-1}$ lies in the subspace without the Goldstone mode. Now we have all

[3] In cases where the quasipotential has multiple minima, the approximation is valid for the time window before the escape time of the local minimum.

[4] Modulo any Goldstone mode – see 5.B

the pieces to calculate the time-antisymmetric component F_{a} and $Y = \sigma^{-1}F_{\mathrm{a}}$,

$$\begin{aligned} F_{\mathrm{a}} &= F(\phi) + K\frac{\delta \mathcal{V}_{\mathrm{ss}}}{\delta \phi} = \sqrt{\epsilon}(A+KG)\phi_1 + O(\epsilon) \\ Y &= \sqrt{\epsilon}\left(\sigma^{-1}A + \sigma^{\dagger}G\right)\phi_1 + O(\epsilon) \end{aligned} \tag{5.39}$$

For convenience, define the matrix $E = \sigma^{-1}A + \sigma^{\dagger}G$ such that $Y = \sqrt{\epsilon}E\phi_1 + O(\epsilon)$. Notice that both F_{a} and Y are $O(\sqrt{\epsilon})$, implying that they vanish at the deterministic order and only depend on the fluctuations. Finally, we can write down the local entropy production rate for a steady state configuration $\phi = \phi_0 + \sqrt{\epsilon}\phi_1 + O(\epsilon)$,

$$\dot{s}(\boldsymbol{x})[\phi_1] = \epsilon^{-1}Y(\boldsymbol{x})^2 = \int \mathrm{d}\boldsymbol{y}\mathrm{d}\boldsymbol{z}E(\boldsymbol{x},\boldsymbol{y})\phi_1(\boldsymbol{y})E(\boldsymbol{x},\boldsymbol{z})\phi_1(\boldsymbol{z}) + h.o.t. \tag{5.40}$$

where *h.o.t.* stands for 'higher order terms'. We can proceed to average over the steady state distribution for ϕ_1 to obtain the ensemble EPR,

$$\begin{aligned} \langle \dot{s}(\boldsymbol{x})\rangle &= \int \mathrm{d}\boldsymbol{y}\mathrm{d}\boldsymbol{z}E(\boldsymbol{x},\boldsymbol{y})C(\boldsymbol{y},\boldsymbol{z})E^{\dagger}(\boldsymbol{z},\boldsymbol{x}) + h.o.t. \\ &= \mathrm{Diag}[ECE^{\dagger}](\boldsymbol{x}) + h.o.t. \end{aligned} \tag{5.41}$$

where "Diag" denotes the diagonal of a matrix. It is worth noting that we also get $\left\langle \dot{S}_{\mathrm{ss}}[\phi]\right\rangle$ for free: $\left\langle \dot{S}_{\mathrm{ss}}\right\rangle = \int \mathrm{d}\boldsymbol{x}\,\langle \dot{s}(\boldsymbol{x})\rangle = \mathrm{Tr}(ECE^{\dagger}) + h.o.t.$ Thus far, we have arrived at a general expression for the lowest order noise expansion for the steady state EPR of any scalar Langevin system. The only knowledge required for this calculation is the deterministic steady state solution, which is both more analytically tractable and less numerically expensive than solving the stochastic dynamics.

Interestingly, we can now identify a sufficient condition for the entropy production to vanish at the leading order in ϵ: when A, K are simultaneously diagonalisable. Let the shared eigenstates be $\{v_i\}$ and the corresponding eigenvalues for A and K be $\{a_i\}$ and$\{k_i\}$ respectively[5]. In this shared eigenspace spanned by $\{v_i\}$, the Lyapunov equation simplifies to $C_{ij}a_j^* + C_{ij}a_i = -2k_i\delta_{ij}$ (no summation convention). Since A is negative definite, implying that $\{a_i\}$ are all real negative numbers, $C_{ij} = -2k_i\delta_{ij}/(a_i + a_j)$, from which we conclude that all off-diagonal elements of C vanish whereas the diagonal elements are known exactly: $C_{ii} = -k_i/a_i$. Substituting into the expression for E, we see that E is also diagonal in the eigenspace and its eigenvalues $\{e_i\}$ are,

$$e_i = \sigma_i^{-1}a_i + \sigma_i^* C_{ii}^{-1} = \sigma_i^{-1}a_i - \sigma_i^* a_i/k_i = 0 \tag{5.42}$$

where the definition of σ has been used to deduce $\sigma_i\sigma_i^* = k_i$. As a result, for any steady state

[5]If there are symmetries or conservation laws, we only work in the relevant physical subspace. See 5.B and section 5.3.4

field fluctuation ϕ_1 around the stationary solution $\phi_0^{\rm ss}$, we have $Y = \sqrt{\epsilon} E\phi_1 + O(\epsilon) = O(\epsilon)$ and the local EPR $\dot{s}(\boldsymbol{x})$ associated with any configuration is at least of order ϵ.

To sum up, we have arrived at a general result for the ensemble average of steady state EPR $\langle \dot{s}(\boldsymbol{x}) \rangle$ at $O(\epsilon^0)$ that only requires the deterministic solution as an input. Moreover, if the Jacobian A and the noise kernel K can be simultaneously diagonalised, the EPR becomes at least $O(\epsilon)$.

5.3.7 Small noise expansion of Model AB

The small noise expansion is especially useful when the steady state of the full stochastic equations cannot be solved analytically. Such is the situation for Model AB away from the special equilibrium subspace described in section 5.2.2. The general scheme is independent of the basis chosen and it turns out to be much simpler in Fourier space. We will therefore perform our algebraic manipulations in Fourier space throughout and only transform back to the real space in the end to calculate $\dot{s}(\boldsymbol{x})$.

The first step of the calculation is to obtain the Jacobian matrix A from the steady state solution $\phi_0^{\rm ss}$, which in Fourier space is explicitly defined as $A(\boldsymbol{q}, \boldsymbol{q}_1) = \delta_{\phi(\boldsymbol{q}_1)} F(\boldsymbol{q})|_{\phi=\phi_0^{\rm ss}}$. Recall from equation (5.14, 5.15) that

$$\begin{aligned} F(\boldsymbol{q}) &= -M_{\rm A}\mu_{\rm A}(\boldsymbol{q}) - M_{\rm B} q^2 \mu_{\rm B}(\boldsymbol{q}) \\ \mu_{\rm A}(\boldsymbol{q}) &= c\,\delta_{\boldsymbol{q},0} + \alpha'\phi(\boldsymbol{q}) + \beta' \sum_{\boldsymbol{q}_1,\boldsymbol{q}_2} \phi(\boldsymbol{q}_1)\phi(\boldsymbol{q}_2)\phi(\boldsymbol{q}-\boldsymbol{q}_1-\boldsymbol{q}_2) \\ \mu_{\rm B}(\boldsymbol{q}) &= -\alpha\phi(\boldsymbol{q}) + \kappa q^2 \phi(\boldsymbol{q}) + \beta \sum_{\boldsymbol{q}_1,\boldsymbol{q}_2} \phi(\boldsymbol{q}_1)\phi(\boldsymbol{q}_2)\phi(\boldsymbol{q}-\boldsymbol{q}_1-\boldsymbol{q}_2) \end{aligned} \tag{5.43}$$

where $\sum_{\boldsymbol{q}}$ is a short-hand for integrating over $\mathrm{d}\boldsymbol{q}/(2\pi)^d$ in infinite domain and summing over all $\boldsymbol{q}$ modes in finite domain. Similarly $\delta_{\boldsymbol{q},\boldsymbol{q}'}$ is the appropriate identity matrix in the Fourier space. Performing the functional derivative,

$$\begin{aligned} A(\boldsymbol{q}, \boldsymbol{q}_1) =& M_{\rm A} \left[c\,\delta_{\boldsymbol{q},0}\delta_{\boldsymbol{q}_1,0} + \alpha'\delta_{\boldsymbol{q},\boldsymbol{q}_1} + 3\beta' \sum_{\boldsymbol{q}_2} \phi_0^{\rm ss}(\boldsymbol{q}_2)\phi_0^{\rm ss}(\boldsymbol{q}-\boldsymbol{q}_1-\boldsymbol{q}_2) \right] \\ &+ M_{\rm B} q^2 \left[(-\alpha + \kappa q^2)\delta_{\boldsymbol{q},\boldsymbol{q}_1} + 3\beta \sum_{\boldsymbol{q}_2} \phi_0^{\rm ss}(\boldsymbol{q}_2)\phi_0^{\rm ss}(\boldsymbol{q}-\boldsymbol{q}_1-\boldsymbol{q}_2) \right] \end{aligned} \tag{5.44}$$

We can see that A is in general non-diagonal in Fourier space and it is indeed a functional of the deterministic solution $\phi_0^{\rm ss}$. As discussed in section 5.2.2, there are typically two stable stationary solutions: the uniform state and arrested phase separation.

In the uniform state, $\phi_0^{\rm ss}(\boldsymbol{q}) = \phi_{\rm t}\delta_{\boldsymbol{q},0}$, where $\phi_{\rm t}$ is the target density of the Model A sector. Substituting $\phi_0^{\rm ss}$ into the expression for A, we can see that $A(\boldsymbol{q}, \boldsymbol{q}_1)$ is nonzero only

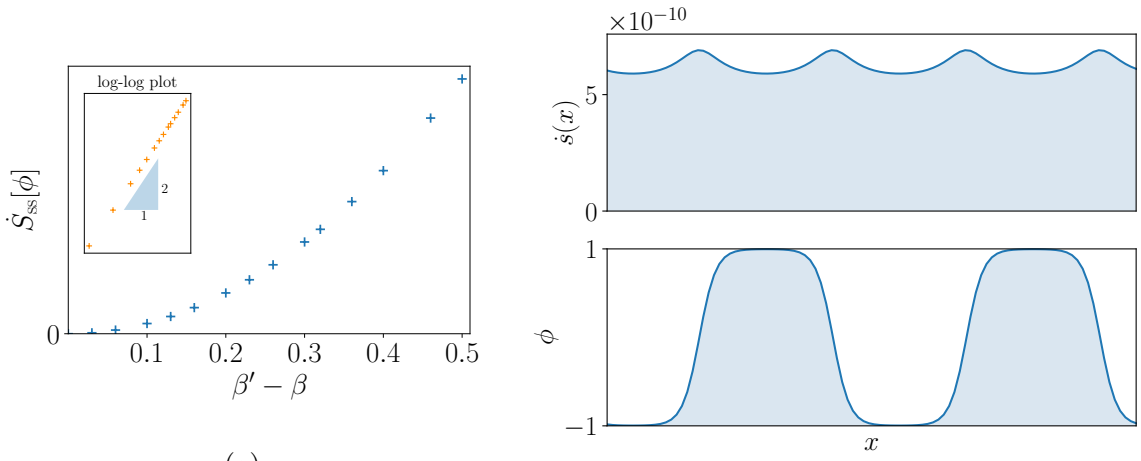

Figure 5.1: (A) Plot of $\dot{S}_{\rm ss}[\phi]$ against $\beta' - \beta$ along with the same data on log-log scale, showing $\dot{S}_{\rm ss}[\phi] \propto (\beta' - \beta)^2$ for small $\beta' - \beta$. Observe that the entropy production rate indeed goes to zero as the equilibrium subspace ($\beta' = \beta$) is approached. (B) The upper panel shows the local entropy production rate $\dot{s}(x)$ (in arbitrary units) and the lower panel shows the corresponding $\phi(x)$. The spatial distribution is mostly uniform with small peaks at the interface. The parameter values are $\alpha = \beta = \alpha' = 1, \beta' = 1.1, \kappa = 5, M_{\rm B} = 0.1, M_{\rm A} = 5 \times 10^{-6}$.

if $\boldsymbol{q} = \boldsymbol{q}_1$. In other words, A is diagonal in Fourier space. Recall that the noise kernel K is also diagonal in Fourier space with diagonal elements $K(\boldsymbol{q}) = M_{\rm A} + M_{\rm B} q^2$. We can conclude that A, K are simultaneously diagonalisable and consequently $\dot{s}(\boldsymbol{x}) = O(\epsilon)$. This is echoed by the work of Nardini et al. [32]: they found the entropy production rate of Active Model B to also be $O(\epsilon)$ in the uniform state. In fact, our line of argument directly applies to their model – the Jacobian and noise kernel for Active Model B are both diagonal in Fourier space, unless $\phi^0_{\rm ss}$ is non-uniform.

On the other hand, in the phase separated state, $A(\boldsymbol{q}, \boldsymbol{q}_1)$ has nonzero off-diagonal elements and A, K are no longer simultaneously diagonalisable. Consequently, the entropy production rate is of order ϵ^0, again echoing the findings of Nardini et al. for the non-homogeneous state of Active Model B [32].

We have explored numerically small values of $\beta' - \beta$ that lead to approximately the same spatial pattern as the equilibrium case ($\beta' = \beta$) to highlight the role of the entropy production rate as a measure of the irreversibility in the system. We refer to section 5.3.6 for details of the spatial discretisation method and subtleties associated with finite domains. The final results are shown in Fig. 5.1. The total steady state entropy production $\dot{S}_{\rm ss}[\phi]$ vanishes in the equilibrium subspace as expected. The spatial decomposition $\dot{s}(x)$ is indeed non-negative everywhere with small peaks at the interfaces, where particles are pumped from the dilute phase to the dense phase.

Additionally, we found that $\dot{S}_{\rm ss}[\phi] \propto (\beta' - \beta)^2$ for the range of $\beta' - \beta$ probed, as shown

in Fig. 5.1a. This can be explained via a perturbative calculation around the equilibrium subspace. Let $\Delta = \beta' - \beta$, and recall from section 5.2.2 that the deterministic dynamics F is the sum of the equilibrium part $(-K\delta_\phi \mathcal{F})$ and an order Δ non-equilibrium piece. Then the Jacobian matrix A shows a similar splitting: $A = -KH + O(\Delta)$, where H is the Hessian of the free energy $\mathcal{F}$, defined as $H_{ij} = \delta_{\phi_i}\delta_{\phi_j}\mathcal{F}$. Note that H is by definition symmetric. The Lyapunov equation can be solved perturbatively yielding the correlation matrix $C = H^{-1} + O(\Delta)$ and its inverse $G = H + O(\Delta)$[6]. As a result, $E = \sigma^{-1}(A + KG) = O(\Delta)$ and $\dot{S}_{\rm ss} = \mathrm{Tr}(ECE^\dagger) = O(\Delta^2)$ as observed.

So far, we have presented a general formula for the entropy production rate $\dot{S}[\phi]$ of the $(\phi, \partial_t\phi)$ trajectories, as well as a non-negative spatial decomposition $\dot{s}(\boldsymbol{x})$ of its steady state value $\dot{S}_{\rm ss}[\phi]$. We demonstrated the computation with a small noise expansion for Model AB, showing that the EPR indeed vanishes as the equilibrium subspace is approached and scales as expected with the deviation from equilibrium $(\beta' - \beta)$. We emphasis that all the computations we have performed until now are of the entropy production rate of the ϕ-trajectories and we do not expect the same conclusions if different information is tracked, as we will show in the next section.

5.4 Entropy production rate for $(\phi, \partial_t\phi_{\rm A}, \partial_t\phi_{\rm B})$ in Model AB

In this section, we explore the consequences of tracking more information in addition to the ϕ-evolution. A natural choice is to separate the local density change $\partial_t\phi$ into Model A and Model B contributions $\partial_t\phi = \partial_t\phi_{\rm A} + \partial_t\phi_{\rm B}$, as defined in equation (5.12). Now we repeat the entire EPR calculation for the new trajectories $(\phi, \partial_t\phi_{\rm A}, \partial_t\phi_{\rm B})$, including deriving the new expressions for the internal and external entropy productions.

For the internal entropy production rate $\dot{S}_{\rm Int}$, our expression for the $(\partial_t\phi, \phi)$ trajectories can be recycled because the initial condition for the path is only a function of ϕ rather than the time derivatives. Substituting $\partial_t\phi_{\rm A} + \partial_t\phi_{\rm B}$ for $\partial_t\phi$ in equation (5.19) yields

$$\epsilon\dot{S}_{\rm Int} = (\partial_t\phi_{\rm A} + \partial_t\phi_{\rm B})^\dagger \frac{\delta\mathcal{V}}{\delta\phi} + \partial_t\mathcal{V} \tag{5.45}$$

The action functional for the new trajectories is more complicated. Applying the standard derivation for the Onsager-Machlup function [88] to $(\partial_t\phi_{\rm A}, \phi)$ and $(\partial_t\phi_{\rm B}, \phi)$ in equation

[6] With the usual caveats regarding inverting matrices in the presence of Goldstone modes – see appendix 5.B

(5.12) separately,

$$\begin{aligned}\mathbb{A}[\phi, \partial_t\phi_{\mathrm{A}}, \partial_t\phi_{\mathrm{B}}] =& \frac{1}{4}\int \mathrm{d}t\, \left((\partial_t\phi_{\mathrm{B}} + K_{\mathrm{B}}\mu_{\mathrm{B}})^\dagger K_{\mathrm{B}}^{-1}(\partial_t\phi_{\mathrm{B}} + K_{\mathrm{B}}\mu_{\mathrm{B}}) + \mathcal{G}_{\mathrm{A}}[\phi]\right) \\ &+ \frac{1}{4M_{\mathrm{A}}}\int \mathrm{d}t\, \left((\partial_t\phi_{\mathrm{A}} + M_{\mathrm{A}}\mu_{\mathrm{A}})^\dagger (\partial_t\phi_{\mathrm{A}} + M_{\mathrm{A}}\mu_{\mathrm{A}}) + \mathcal{G}_{\mathrm{B}}[\phi]\right)\end{aligned} \tag{5.46}$$

where $\mathcal{G}_{\mathrm{A,B}}[\phi]$ are functionals of ϕ only, as a consequence of the Stratonovich convention for the path integral. One can check that this yields the action for $(\phi, \partial_t\phi)$ path once we change the variable to $\partial_t\phi = \partial_t\phi_{\mathrm{A}} + \partial_t\phi_{\mathrm{B}}$ and integrate over one of $(\partial_t\phi_{\mathrm{A}}, \partial_t\phi_{\mathrm{B}})$. As before, under time reversal, the time derivatives flip sign: $\partial_t\phi^{\mathrm{R}}_{\mathrm{A,B}}(t) = -\partial_s\phi_{\mathrm{A,B}}(s)|_{s=\tau-t}$. After repeating the steps taken previously (section 5.3), we take the difference between the action of the forward path and that of the reversed path to obtain the external entropy production rate,

$$\epsilon\dot{S}_{\mathrm{Ext}} = -\partial_t\phi^\dagger_{\mathrm{B}}\mu_{\mathrm{B}} - \partial_t\phi^\dagger_{\mathrm{A}}\mu_{\mathrm{A}} \tag{5.47}$$

Adding $\dot{S}_{\mathrm{Int}}$ and $\dot{S}_{\mathrm{Ext}}$ gives the total instantaneous entropy production rate,

$$\epsilon\dot{S}[\phi, \partial_t\phi_{\mathrm{A}}, \partial_t\phi_{\mathrm{B}}] = \partial_t\mathcal{V} - \partial_t\phi^\dagger_{\mathrm{B}}\left(\mu_{\mathrm{B}} - \frac{\delta\mathcal{V}}{\delta\phi}\right) - \partial_t\phi^\dagger_{\mathrm{A}}\left(\mu_{\mathrm{A}} - \frac{\delta\mathcal{V}}{\delta\phi}\right) \tag{5.48}$$

Once again, we average over the time derivatives $(\partial_t\phi_{\mathrm{A}}, \partial_t\phi_{\mathrm{B}})$ using the conditional expectations $\langle\partial_t\phi_{\mathrm{A}}|\phi, t\rangle = -M_{\mathrm{A}}(\mu_{\mathrm{A}} - \delta_\phi\mathcal{V})$ and $\langle\partial_t\phi_{\mathrm{B}}|\phi, t\rangle = -K_{\mathrm{B}}(\mu_{\mathrm{B}} - \delta_\phi\mathcal{V})$. We refer to appendix 5.A for a rather involved calculation of the conditional expectations, but one can check that they indeed add up to the same $\langle\partial_t\phi|\phi, t\rangle$ as before. This yields the total entropy production rate for the configuration ϕ

$$\epsilon\dot{S}^{\mathrm{AB}}[\phi] = \partial_t\mathcal{V} + (\mu_{\mathrm{B}} - \delta_\phi\mathcal{V})^\dagger K_{\mathrm{B}}(\mu_{\mathrm{B}} - \delta_\phi\mathcal{V}) + M_{\mathrm{A}}(\mu_{\mathrm{A}} - \delta_\phi\mathcal{V})^\dagger(\mu_{\mathrm{A}} - \delta_\phi\mathcal{V}) \tag{5.49}$$

Notice that $\dot{S}^{\mathrm{AB}}$ possesses similar properties as the entropy production rate $\dot{S}[\phi]$ in equation (5.21): non-negative upon averaging over the stochastic trajectories and non-negative for each field configuration ϕ in steady state. Furthermore, we can also decompose the new steady state EPR, denoted as $\dot{S}^{\mathrm{AB}}_{\mathrm{ss}}[\phi]$, into local non-negative contributions $\dot{s}^{\mathrm{AB}}(\boldsymbol{x})$ such that $\dot{S}^{\mathrm{AB}}_{\mathrm{ss}}[\phi] = \int \mathrm{d}\boldsymbol{x}\dot{s}^{\mathrm{AB}}(\boldsymbol{x})$,

$$\epsilon\dot{s}^{\mathrm{AB}}[\boldsymbol{x}] = Y_{\mathrm{B}}(\boldsymbol{x})Y_{\mathrm{B}}(\boldsymbol{x}) + Y_{\mathrm{A}}(\boldsymbol{x})Y_{\mathrm{A}}(\boldsymbol{x}) \tag{5.50}$$

where $Y_{\mathrm{B}} = \sigma_{\mathrm{B}}(\mu_{\mathrm{B}} - \delta_\phi\mathcal{V}_{\mathrm{ss}})$and $Y_{\mathrm{A}} = \sqrt{M_{\mathrm{A}}}(\mu_{\mathrm{A}} - \delta_\phi\mathcal{V}_{\mathrm{ss}})$. Following the arguments made in section (5.3.4), we can see that, if given the quasipotential $\mathcal{V}_{\mathrm{ss}}$, $Y_{\mathrm{B}}(\boldsymbol{x})^2 = M_{\mathrm{B}}^{-1/2}|\tilde{\boldsymbol{J}}_{\mathrm{a}}(\boldsymbol{x})|^2$, where $\tilde{\boldsymbol{J}}_{\mathrm{a}}(\boldsymbol{x})$ is the curl-free piece of the diffusive current and equals $\boldsymbol{\nabla}(\mu_{\mathrm{B}} - \delta_\phi\mathcal{V}_{\mathrm{ss}})$ in this case. Thus we can assign Y^2_{B} as the entropy production rate of Model B with quasipotential $\mathcal{V}_{\mathrm{ss}}$. Similar arguments can be made for Y_{A}: recall from equation (5.10) that

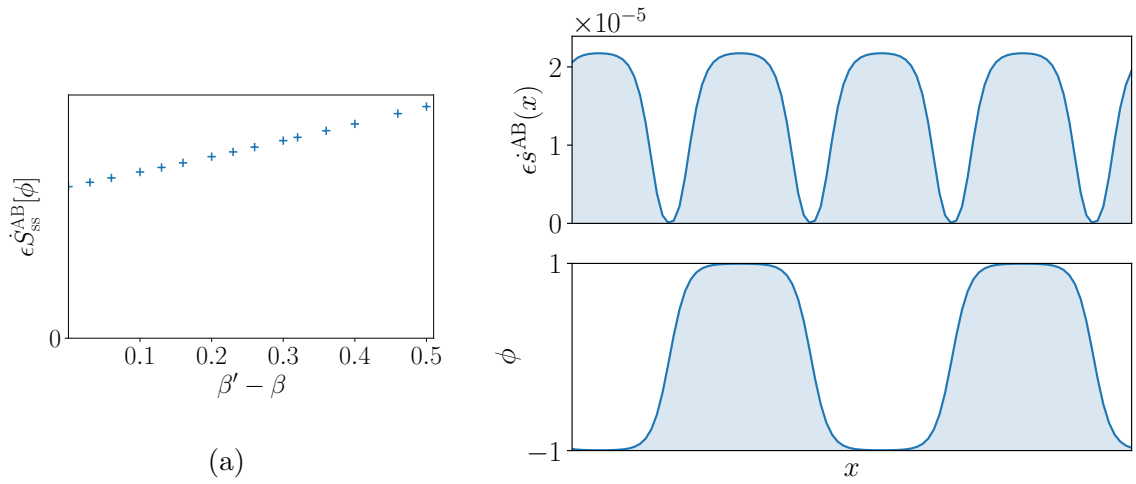

(a) (b)

Figure 5.2: (A) Plot of $\epsilon\dot{S}_{\rm ss}^{\rm AB}[\phi]$ against $\beta' - \beta$. In contrast with Fig. 5.1, the entropy production rate remains non-zero in the equilibrium subspace. (B) The upper panel shows the spatial decomposition of the entropy production rate $\dot{s}^{\rm AB}(x)$ and the lower panel shows the corresponding $\phi(x)$. Most of the entropy production is due to the Model A currents in the plateaus. The parameter values are $\alpha = \beta = \alpha' = 1, \beta' = 1.1, \kappa = 5, M_{\rm B} = 0.1, M_{\rm A} = 5 \times 10^{-6}$.

for Model A, $K_{\rm A} = M_{\rm A}$ and $\sigma_{\rm A} = \sqrt{M_{\rm A}}$; hence we obtain the antisymmetric component $F_{\rm a}^{\rm A} = M_{\rm A}\left(\mu_{\rm A} - \partial_\phi \mathcal{V}_{\rm ss}\right)$ and the corresponding $Y_{\rm A} = \sigma^{-1} F_{\rm a}^{\rm A} = \sqrt{M_{\rm A}}\left(\mu_{\rm A} - \delta_\phi \mathcal{V}_{\rm ss}\right)$. Note that the quasipotential $\mathcal{V}_{\rm ss}$ is that of the Model AB dynamics, which is qualitatively different from Model A or Model B on its own.

We would like to emphasize that this clear splitting in terms of Model A and Model B contributions is a consequence of tracking the two sectors separately via $(\partial_t \phi_{\rm B}, \partial_t \phi_{\rm B})$. Although both $\dot{S}_{\rm ss}^{\rm AB}[\phi]$ and the previously calculated entropy production rate $\dot{S}_{\rm ss}[\phi]$ (equation (5.22)) are functionals of the field configuration ϕ only, once the time derivatives have been averaged over, they are entirely different quantities and there is no direct path to convert between them.

The new entropy production rate $\dot{S}_{\rm ss}^{\rm AB}[\phi]$ is plotted in Fig. 5.2 for the same parameters as the numerical calculations that produced Fig. 5.1 in the previous section. We also retain the assumption that $\epsilon \ll 1$ and only compute expressions to lowest order in ϵ, for easy comparison with the calculation of $\dot{S}_{\rm ss}$. Since both $\mu_{\rm A}, \boldsymbol{\nabla}\mu_{\rm B}$ are non-zero at the deterministic level, whereas $\mathcal{V}_{\rm ss}$ is of order ϵ (see equation (5.38)), we can see that, to leading order in ϵ, $Y_{\rm A,B}$ are only functions of the deterministic steady state $\phi_{\rm ss}^0$: $Y_{\rm A}^2 = M_{\rm A}(\mu_{\rm A}(\phi_{\rm ss}^0))^2 + O(\sqrt{\epsilon})$ and $Y_{\rm B}^2 = M_{\rm B}(\boldsymbol{\nabla}\mu_{\rm B}(\phi_{\rm ss}^0))^2 + O(\sqrt{\epsilon})$. As a result, the new entropy production rate $\dot{S}_{\rm ss}^{\rm AB}$, as well as its local decomposition $\dot{s}^{\rm AB}(\boldsymbol{x})$, are of order $1/\epsilon$, as opposed to $\dot{S}_{\rm ss}$ and $\dot{s}(\boldsymbol{x})$, which are both at most $O(\epsilon^0)$ as shown in equation (5.41).

The difference between the two EPRs is manifested more dramatically in the equilibrium

subspace: μ_{A} and $\boldsymbol{\nabla}\mu_{\mathrm{B}}$ both remain finite in this limit and so does $\dot{S}_{\mathrm{ss}}^{\mathrm{AB}}$, as shown in Fig. 5.2a, whereas $\dot{S}_{\mathrm{ss}}$ vanishes as the special subspace is approached (see Fig. 5.1a). Near the equilibrium subspace, $\dot{S}_{\mathrm{ss}}^{\mathrm{AB}}$ appears to increase linearly with with the deviation $\beta' - \beta$, in contrast with the quadratic scaling observed for $\dot{S}_{\mathrm{ss}}$. This can be explained by expanding $\dot{S}_{\mathrm{ss}}^{\mathrm{AB}}$ for small $\Delta = \beta' - \beta$ as before. The deterministic steady state solution ϕ_{ss}^0 remains approximately the same across the range of Δ probed. Furthermore, as we only vary β' but keep β fixed, $(\boldsymbol{\nabla}\mu_{\mathrm{B}})$ stays constant while $\mu_{\mathrm{A}}(\Delta) = \mu_{\mathrm{A}}(\Delta = 0) + O(\Delta)$, leading to an $O(\Delta)$ piece in Y_{A}^2 and hence $\dot{S}_{\mathrm{ss}}^{\mathrm{AB}} \propto \Delta$ upon spatial integration.

Another interesting observation is that the local entropy production rate $\dot{s}^{\mathrm{AB}}(x)$ is more prominent at the plateaus, although the value remains finite at the interfaces, as shown in Fig. 5.2b. To explain this phenomenon, we start with examining the local Model A and Model B contributions separately: $Y_{\mathrm{A}}^2 (= M_{\mathrm{A}}\mu_{\mathrm{A}}^2)$ is large at the plateaus, where the magnitude of the field $|\phi_{\mathrm{ss}}^0|$ is maximum, and goes to zero at the interfaces where $\phi_{\mathrm{ss}}^0 = 0$; on the other hand, $Y_{\mathrm{B}}^2 (= M_{\mathrm{B}}|\boldsymbol{\nabla}\mu_{\mathrm{B}}|^2)$ is large at the interface, where the gradient is sharp, and small in the plateaus. Next, let the length scale of the pattern be L. In steady state, we have, approximately, $M_{\mathrm{B}}\mu_{\mathrm{B}}/L^2 \sim M_{\mathrm{A}}\mu_{\mathrm{A}}$, from which we can deduce that $Y_{\mathrm{A}}^2/Y_{\mathrm{B}}^2 \sim M_{\mathrm{B}}/(M_{\mathrm{A}}L^2)$. For the input parameters of our simulations, this ratio is much greater than 1. Thus the spatial decomposition $\dot{s}^{\mathrm{AB}}$ is dominated by Model A contributions, which accounts for the peaks at the plateaus.

To conclude, in this section we presented an alternative way of tracking information for Model AB, and arrived at new expressions for the total steady state entropy production rate $\dot{S}_{\mathrm{ss}}^{\mathrm{AB}}$ and the local production rate $\dot{s}^{\mathrm{AB}}(\boldsymbol{x})$. Both quantities are markedly different from their counterparts in section 5.3.7, in terms of their behaviour in the equilibrium subspace, scaling with the deviation $(\beta' - \beta)$ and the spatial profile of the local entropy production. Generically there is no pathway of conversion between the new entropy production rates and the ones in section 5.1, highlighting the importance of the information tracked. Recall that these calculations treat entropy production as an informatic quantity, and hence dependent on what variables are tracked; we are not attempting to calculate a physical heat production whose full elucidation would require tracking of *all* microscopic sources of dissipation underlying the model (see [83]).

5.5 Conclusion

In this chapter, we presented a method to compute the entropy production rate $\dot{S}$ for scalar Langevin systems with additive noise, as a quantitative measure of the extent to which the time reversal symmetry is broken at the macroscopic scale. We discussed in detail the EPR of equilibrium systems and their non-equilibrium extensions, as well as a case study of Model AB that describes systems with mismatched conservative and non-conservative

dynamics.

Following the work of Seifert [27, 77] in stochastic thermodynamics, we defined the field-theoretic entropy production ΔS for a trajectory as the difference between the rate function of the forward path and that of the reversed path. The entropy production rate is subsequently obtained by differentiating ΔS with respect to time. It is often convenient to split ΔS into an internal piece ΔS_{Int} and an external piece ΔS_{Ext}, before taking the time derivatives of both and summing the internal and external contributions to give the total rate of change. The internal entropy production is a "surface term" in time, accounting for the difference in the Gibbs entropies of the initial and final state. The external part is the contribution from the action. Though ΔS_{Ext} can be related to the heat production in simple particle-based systems, its physical interpretation in general systems is less clear.

In field theories, the probability of a trajectory in configuration space, and hence its rate function and the entropy production rate, depends on the macroscopic variables used to define the path. We first explored the natural choice of tracking $(\partial_t\phi, \phi)$ trajectories. In steady state, we found that the resulting entropy production rate $\dot{S}_{\mathrm{ss}}[\phi]$ of every field configuration is non-negative and there also exists a spatial decomposition $\dot{s}(\boldsymbol{x})$ that is guaranteed to be locally non-negative. Both are only function of the time-antisymmetric component of the dynamics $F_{\mathrm{a}} = F + K\delta_\phi \mathcal{V}$, which is another measure of the deviation from equilibrium, analogous to the antisymmetric currents in Macroscopic Fluctuation Theory. In equilibrium, both $\dot{S}_{\mathrm{ss}}$ and $\dot{s}(\boldsymbol{x})$ vanish as expected from the principle of detailed balance. For Model-B type systems with mass conservation, the local entropy production is $(\epsilon M)^{-1}|\widetilde{\boldsymbol{J}}_{\mathrm{a}}|^2$ where $\widetilde{\boldsymbol{J}}_{\mathrm{a}}$ is the pure gradient part of the antisymmetric current, as any curl-part does not show in the ϕ-evolution and therefore cannot contribute to the entropy production.

In practice, the computation of the antisymmetric dynamics F_{a} and therefore the steady state EPR requires the knowledge of the quasipotential $\mathcal{V}_{\mathrm{ss}}$, which is only known exactly for solvable systems. To make progress, we performed a perturbative expansion in the noise magnitude ϵ that only requires the (numerical or analytical) solution of the deterministic equation. In steady state, both the total EPR and its spatial decomposition are at most of order ϵ^0. In the special case where the noise kernel K and the Jacobian A are simultaneously diagonalisable, both $\dot{S}_{\mathrm{ss}}$ and $\dot{s}$ are $O(\epsilon)$, echoing the findings of Nardini et al. [32]. For Model AB, we found that the total steady state EPR vanishes in the equilibrium subspace and scales quadratically with the deviation $\beta' - \beta$ near the subspace. The spatial decomposition $\dot{s}(x)$ is positive everywhere with small peaks at the interfaces.

To understand the effect of tracking different macroscopic variables, we then computed the EPR of Model AB with additional information on contributions from the Model A and Model B sectors. The new entropy production rate $\dot{S}^{\mathrm{AB}}$ is of order ϵ^{-1}, reflecting the fact that once the conservative and non-conservative parts are tracked separately, the dynamics

is irreversible in time even at the deterministic level. In steady state, the EPR $\dot{S}_{\rm ss}^{\rm AB}$ of each field configuration is also non-negative and we can identify a non-negative spatial decomposition that constitutes of a Model A contribution related to the local reactions and a Model B contribution from the macroscopic currents. Both the new steady state EPR $\dot{S}_{\rm ss}^{\rm AB}$ and its spatial decomposition $\dot{s}^{\rm AB}$ show qualitatively different phenomena to their counterparts in the previous case: $\dot{S}_{\rm ss}^{\rm AB}$ remains finite in the special subspace and increases linearly with $\beta' - \beta$; $\dot{s}^{\rm AB}$ exhibits large peaks at the plateaus instead of the interfaces.

While in this work we mainly focused on the small noise expansion, there is a lot of potential for interesting studies on whether the spatial decomposition will change as the noise amplitude increases, as there is no reason to believe that the terms that are higher order in ϵ have the same spatial distribution as the leading order term. In addition, our formalism rests on the additivity of noise within the Langevin framework and not the scalar character of the fields involved (although we restricted to this case for simplicity of notation). Accordingly it can be easily extended to vectorial or tensorial systems with applications to swarming active matter and active liquid crystals. This could allow a deeper understanding of entropy production in these wider classes of active systems, whose analysis using stochastic thermodynamics has recently been initiated [83, 89].

Appendix

5.A Expectation values with Stratonovich discretisation

In this appendix, we will define and evaluate the conditional expectations $\langle \partial_t \phi | \phi, t \rangle$ and $\langle \partial_t \phi_{\mathrm{A,B}} | \phi, t \rangle$ that are essential in averaging over the time derivatives to obtain an expression for the EPR of a field configuration ϕ in section 5.3 and 5.4. We will only demonstrate the calculation explicitly for a simple one dimensional case, though generalisation to field theories should be relatively straight forward.

Consider a single-variable stochastic differential equation (SDE) with non-multiplicative noise,

$$\dot{x} = f(x) + \sqrt{2\epsilon K}\Lambda$$

where Λ is a unit white noise. This equation is only well-defined once the discretisation scheme is specified, but as the noise is non-multiplicative all discretisations are equivalent. Without loss of generality we choose the endpoint discretisation: for a set of discrete time steps $\{t_i\}$ with spacing Δt, the discretised SDE is

$$\Delta x(t_i) = f[x(t_{i+1})]\Delta t + \Delta W(t_i)$$

where $\Delta x(t_i) = x(t_{i+1}) - x(t_i)$ and W is a Wiener process with correlation $\langle \Delta W(t_i) \Delta W(t_j) \rangle = 2\epsilon K \Delta t \delta_{ij}$. Note that the discretisation of the SDE is a separate choice from that of the path integral. For the purpose of entropy production, we always use the Strato-discretised action functional but that does not limit our choice of discretisation for the SDE.

The conditional expectation $\langle \dot{x} | x, t \rangle$ in section 5.3 is the expectation value of $\dot{x}$ at time t given that a fixed value of x at time t. The $\dot{x}$ here can traced back to the $\dot{x}$ in the action functional $\mathbb{A}$, which follows the Stratonovich (midpoint) scheme. Thus the discretised version of the conditional expectation is,

$$\langle \dot{x} | x, t \rangle = \mathbb{E}\left[\lim_{\Delta t \to 0} \frac{\Delta x(t_{i-1}) + \Delta x(t_i)}{2\Delta t} \middle| x(t_i) = x \right]$$

The rest of this derivation is presented in Seifert's papers [77] and we will not repeat here. He showed that $\langle \dot{x}|x,t\rangle = f(x) - \epsilon K \partial_x \log P(x,t) = f(x) + K\partial_x V(x,t)$, where $V(x,t)$ is the quasipotential defined in the same way as for fields: $P(x,t) \propto \exp(-\epsilon^{-1}V(x,t))$.

Next, we consider the one dimensional version of Model AB, where there are two separate contributions to the time derivative with independent noises. As before, we choose endpoint discretisation though all choices are equivalent,

$$\begin{aligned}
\Delta x(t_i) &= \Delta x_{\mathrm{A}}(t_i) + \Delta x_{\mathrm{B}}(t_i) \\
\Delta x_{\mathrm{A}}(t_i) &= f_{\mathrm{A}}[x(t_{i+1})]\Delta t + \Delta W_{\mathrm{A}}(t_i) \\
\Delta x_{\mathrm{B}}(t_i) &= f_{\mathrm{B}}[x(t_{i+1})]\Delta t + \Delta W_{\mathrm{B}}(t_i)
\end{aligned}$$

where $W_{\mathrm{A,B}}$ are independent Wiener processes with $\langle \Delta W_{\mathrm{A,B}}(t_i)\Delta W_{\mathrm{A,B}}(t_j)\rangle = 2\epsilon K_{\mathrm{A,B}}\Delta t\delta_{ij}$. The one dimensional version of the conditional expectation in section 5.4 is $\langle \dot{x}_{\mathrm{A}}|x,t\rangle$, formally defined as

$$\langle \dot{x}_{\mathrm{A}}|x,t\rangle = \mathbb{E}\left[\lim_{\Delta t\to 0} \frac{\Delta x_{\mathrm{A}}(t_{i-1}) + \Delta x_{\mathrm{A}}(t_i)}{2\Delta t}\middle| x(t_i) = x\right]$$

Our calculation for the conditional expectation mainly follows the line of Seifert's calculation [77]. First, by linearity of the conditional expectation, we can evaluate the following before taking the limit of $\Delta t \to 0$,

$$\begin{aligned}
\mathbb{E}\left[\Delta x_{\mathrm{A}}(t_{i-1}) + \Delta x_{\mathrm{A}}(t_i)|x(t_i) = x\right] &= \mathbb{E}\left[\Delta x_{\mathrm{A}}(t_{i-1})|x(t_i)\right] + \mathbb{E}\left[\Delta x_{\mathrm{A}}(t_i)|x(t_i) = x\right] \\
&= \mathbb{E}\left[f_{\mathrm{A}}[x_{i-1}]\Delta t + \Delta W_{\mathrm{A}}(t_{i-1})|x(t_i) = x\right] \\
&\quad + \mathbb{E}\left[f_{\mathrm{A}}[x(t_i)]\Delta t + \Delta W_{\mathrm{A}}(t_i)|x(t_i) = x\right]
\end{aligned}$$

The second term is a forward time conditional expectation. Using the non-anticipating property of the Wiener process,

$$\begin{aligned}
\mathbb{E}\left[f_{\mathrm{A}}[x(t_{i+1})]\Delta t + \Delta W_{\mathrm{A}}(t_i)|x(t_i) = x\right] &= \mathbb{E}\left[f_{\mathrm{A}}[x(t_{i+1})]\Delta t|x(t_i) = x\right] \\
&= \mathbb{E}\left[f_{\mathrm{A}}[x(t_i)]\Delta t + O\left(\Delta t^{3/2}\right)|x(t_i) = x\right] \\
&= f_{\mathrm{A}}(x)\Delta t + O\left(\Delta t^{3/2}\right)
\end{aligned}$$

The first term is trickier as $x(t_i)$ is not independent of $\Delta W_{\mathrm{A}}(t_{i-1})$. Writing the conditional expectation of the noise term as an explicit integral over the probabilities,

$$\mathbb{E}\left[f_{\mathrm{A}}[x(t_i)]\Delta t + \Delta W_{\mathrm{A}}(t_{i-1})|x(t_i) = x\right] = f_{\mathrm{A}}(x) + \int \mathrm{d}\xi\, \xi P\left(\Delta W_{\mathrm{A}}(t_{i-1}) = \xi|x(t_i) = x\right)$$

Omitting the time label on ΔW_{A} for brevity, and using Bayes' theorem for the conditional

probability,

$$\begin{aligned}\mathbb{E}\left[\Delta W_{\mathrm{A}}|x(t_i)=x\right] &= \int \mathrm{d}\xi P\left(x(t_i)=x|\Delta W_{\mathrm{A}}=\xi\right)\frac{P(\Delta W_{\mathrm{A}}=\xi)}{P(x(t_i)=x)} \\ &= \int \mathrm{d}\xi\mathrm{d}\eta\, P(x(t_i)=x|\Delta W_{\mathrm{A}}=\xi, x(t_{i-1})=\eta)\frac{P(\Delta W_{\mathrm{A}}=\xi)P(x(t_{i-1})=\eta)}{P(x(t_i)=x)}\end{aligned}$$

Inspection of the conditional probability $P(x(t_i)=x|\Delta W_{\mathrm{A}}=\xi, x(t_{i-1})=\eta)$ reveals that it is equivalent to the probability of the difference

$$P(x(t_i)=x|\Delta W_{\mathrm{A}}=\xi, x(t_{i-1})=\eta) = P(\Delta W_{\mathrm{B}}=x-\eta-\xi-f_{\mathrm{A}}(x)\Delta t-f_{\mathrm{B}}(x)\Delta t) \equiv P(\Delta W_{\mathrm{B}}=\zeta)$$

where we defined a new variable ζ at the last equality. Next, we simplify the following fraction in the integrand by expanding in small Δx,

$$\frac{P(x(t_{i-1})=\eta)}{P(x(t_i)=x)} = 1-(x-\eta)\partial_x \log P(x,t_i)$$

Changing the integration variable from η to ζ and combining the terms,

$$\begin{aligned}\mathbb{E}\left[\Delta W_{\mathrm{A}}|x(t_i)=x\right] &= \int \mathrm{d}\xi\mathrm{d}\zeta\, \xi P(\Delta W_{\mathrm{B}}=\zeta)P(\Delta W_{\mathrm{A}}=\xi)\left[1-(\zeta+\xi+f_{\mathrm{A}}(x)\Delta t+f_{\mathrm{B}}(x)\Delta t)\partial_x \log P\right] \\ &= -\int \mathrm{d}\xi\, \xi^2 P(\Delta W_{\mathrm{A}}=\xi)\partial_x \log P + O\left(\Delta t^{3/2}\right) \\ &= -2\epsilon K_{\mathrm{A}}\Delta t\partial_x \log P + O\left(\Delta t^{3/2}\right)\end{aligned}$$

where we have used the correlation for the Wiener process W_{A} in the last line. Adding the terms together, the conditional expectation is

$$\mathbb{E}\left[\Delta x_{\mathrm{A}}(t_{i-1})+\Delta x_{\mathrm{A}}(t_i)|x(t_i)=x\right] = 2f(x)\Delta t - 2\epsilon K_{\mathrm{A}}\partial_x \log P(x,t_i)$$

Dividing both sides by Δt and taking the limit $\Delta t \to 0$, we obtain the desired conditional expectation,

$$\mathbb{E}\left[\dot{x}_{\mathrm{A}}(t)|x(t)=x\right] = f(x) - \epsilon K_{\mathrm{A}}\partial_x \log P(x,t) = f(x) + K_{\mathrm{A}}\partial_x V(x,t)$$

This concludes the calculation the one dimensional version of the conditional expectation values mentioned in section 5.4, and we refer back to the main text for how it is used to calculate the entropy production rate of $(\phi, \partial_t\phi_{\mathrm{A}}, \partial_t\phi_{\mathrm{B}})$ trajectories.

5.B Entropy production with continuous symmetry

This appendix discusses the details of the calculation of the local entropy production in section 5.3.6 in the case of a spontaneously broken continuous symmetry in the system.

In the presence of the broken symmetry, there exists a Goldstone mode v: an eigenvector of the matrix A with zero eigenvalue. In our case, with periodic boundary conditions, our system possesses translational symmetry (invariance under $\phi(x) \to \phi(x + \delta x)$). In fact, the Goldstone mode v equals $\partial_x \phi^0_{\rm ss}$, where $\phi^0_{\rm ss}$ is the deterministic steady state solution. Another consequence is that the quasipotential $\mathcal{V}_{\rm ss}$ also has the same symmetry. Recall from equation (5.38) that $\mathcal{V}_{\rm ss}[\phi_1] = -\frac{\epsilon}{2}\phi_1^\dagger G \phi_1$ (without the degeneracy, G is the inverse of the correlation function). G also has v as an eigenvector with eigenvalue zero. The projection operator $P = 1 - vv^\dagger$ defines the projection into the subspace without the Goldstone mode. We can immediately see that $AP = A$ and $GP = P$.

Recall from equation (5.41) that to lowest order in the noise parameter ϵ,

$$\langle \dot{s} \rangle = \text{Diag}\left[ECE^\dagger\right] + O(\epsilon^{1/2})$$

where $E = \sigma^{-1}A + \sigma^\dagger G$. Note that we also have $EP = E$: the Goldstone mode v is also an eigenvector of E with zero eigenvalue. Hence

$$\left\langle \dot{S} \right\rangle = \text{Diag}\left[E(PCP)E^\dagger\right] + O(\epsilon^{1/2})$$

This implies that only correlations in the subspace contribute towards the total entropy production. Hence we only need to solve the reduced Lyapunov equation obtained by multiplying the full Lyapunov equation by P on the left and right,

$$(PAP)(PCP) + (PCP)(PA^\dagger P) = -2(PKP) \tag{5.51}$$

In practice, we add a small eigenvalue λ in the Goldstone mode, and define $A_\lambda = A + \lambda vv^\dagger$. This makes the original Lyapunov equation well-defined and solvable. Let the corresponding solution of the λ- regularised equation be C_λ such that

$$A_\lambda C_\lambda + C_\lambda A_\lambda^\dagger = -2K$$

Multiplying the equation on the left and right by the projection P gives

$$PA_\lambda C_\lambda P + PC_\lambda A_\lambda^\dagger P = -2PKP$$

Note that $PA_\lambda = P(A + \lambda vv^\dagger) = PA$ and $AP = A$, the above equation is equivalent to

$$(PAP)(PC_\lambda P) + (PC_\lambda P)(PA^\dagger P) = -2PKP$$

Comparing with equation (5.51) reveals that $PC_\lambda P = PCP$.

Next we proceed to calculate G. The quadratic form of the quasipotential leads to the inverse relation in the subspace $PCPG = GPCP = P$. Use the same trick as before and let $\tilde{C}_\lambda = PCP + \lambda vv^\dagger$ (not the same as C_λ), we have

$$P = P\tilde{C}_\lambda^{-1}\tilde{C}_\lambda P = P\tilde{C}_\lambda^{-1}PPCP$$

Thus we can identify $G = P\tilde{C}_\lambda^{-1}P$ and use it to calculate E. Note that λ remains finite throughout the calculation.

5.C Numerical implementations

In this section, we outline the numerical implementations of the small noise expansion of the entropy production rate for Model AB. In section 5.3.7, we performed the computations in Fourier space and only transform back to the real space at the last step to obtain the spatial decomposition. The Fourier transform applies to infinite continuous spatial domain but needs to be modified for numerical studies as the simulation box size is only finite and so is the number of grid points. This is because the discrete Jacobian matrix A used in the weak noise expansion must the same as the Jacobian of the numerical integration of the deterministic PDE such that A is negative definite (modulo Goldstone modes) as assumed.

For numerical integration of PDEs, there are two methods of spatial discretisation for domains with periodic boundary conditions: finite difference method and pseudospectral method. Both methods converge for Model AB simulations in one dimension for a relatively small spatial domain, such is the case of interest here. In this chapter, we use the former for simplicity though our analysis can be easily extended to the latter. In finite difference scheme, the Laplacian operator is represented by the following matrix,

$$(\nabla^2)_{mn} = \frac{1}{a^2}\left(-2\delta_{m,n} + \delta_{m,n-1} + \delta_{m,n+1}\right) \tag{5.52}$$

where the indices wrap around and a is the lattice spacing. In our simulations, we always rescale the parameters such that $a = 1$ so we will drop it from now on. The finite-difference Laplacian is diagonalised by the discrete Fourier Transform matrix $U_{mn} = L^{-1/2}\exp(-2\pi imn/L)$ with diagonal elements $d_n = -2\left[1 - \cos(2\pi n/L)\right]$, where L is the length of the domain (remember $a = 1$). As a sanity check, we can see that for small n

and large L, $d_n \approx (2\pi n/L)^2 = q_n^2$, where q_n are the discrete Fourier modes. This means that the eigenspace for the discrete Laplacian operator is the (discrete) Fourier space and we can use Fast Fourier Transform algorithms to go between the eigenspace and the real space. In addition, we can obtain the discrete Jacobian matrix A by substituting d_n for q^2 in equation (5.44) and the noise kernel K is diagonal in Fourier space with elements $K_n = M_\mathrm{A} + M_\mathrm{B} d_n$. The rest of the computation follows rather straight forwardly by using the results of 5.B to take care of the Goldstone mode and the Lyapunov equation can be solved using the Bartels-Stewart algorithm [90], which is part of many popular numerical libraries such as Scipy and LAPACK.

Chapter 6

Conclusion

In this thesis, we formulated two scalar field theories with increasing complexity, Model AB and Model AB+, for a novel class of non-equilibrium reaction-diffusion systems with phase-separating conservative dynamics, and explored the physical behaviours of both theories. Examples in this class include biomolecular condensates [7], bacteria colonies [45] and binary polymer mixtures with externally maintained reactions [22].

Model AB was constructed as a minimal theory for this general class of systems. It combines equilibrium Model B and Model A in Hohenberg and Halperin's classification for the conservative and non-conservative sectors respectively. We argued that the mismatch between the free energies of the two sectors is sufficient to break detailed balance without TRS-breaking terms in either sector. For the majority of chapter 3, we studied a 'canonical' version of Model AB, retaining lowest order terms in the Landau-Ginzburg expansion in each sector, plus one additional quadratic term in the reaction dynamics to ensure that the global mean density does not decouple from other degrees of freedom. We showed that our canonical model captures various collective behaviours reported of more complex models of this non-equilibrium reaction-diffusion class across the literature, including microphase separation (with lamellar or droplet patterns depending on the target density of the reaction), anti-coarsening via droplet-splitting and steady state oscillations between a homogeneous and a phase-separated state [7, 22, 23, 44, 45].

In chapter 4, we furthered our investigation into non-equilibrium reaction-diffusion systems by studying the effect of having diffusive dynamics that breaks time reversal symmetry on its own, on top of the mismatch of Model B and Model A free energies. We named the resulting theory Model AB+, as it incorporates the λ and ζ terms in Active Model B+ [11] into Model AB. The model was motivated by the ability of the λ and ζ terms to cause microphase separation on their own by reversing the classical Ostwald process, as well as RG calculations showing a new strong coupling regime associated with these terms [76]. We focussed specially on regimes where the surface tension for droplets are negative and found a novel steady state where the system exhibits 'bubbly' microphase

separation with small droplets of the liquid phase continuously created within the minority vapour phase before growing in size and merging with the surrounding liquid majority phase. Our study was not intended as a systematic exploration of the parameter space of Model AB+, and we believe there is plenty of room to find new physics in the model, such as the effect of the λ and ζ terms on the steady state oscillations of Model AB studied at the end of chapter 3. We also note that although we have not made any attempt to connect parameters of Model AB(+) with practical experimental settings – a task that is generally extremely hard – we believe our studies can already suggest mechanistic pathways for emergent phenomena that could be rather puzzling otherwise, such as the 'bubbly' state or limit cycles, as were discussed in chapter 4 and section 3.4 respectively.

In general, Model AB(+) is far away from equilibrium. However, we found an equilibrium subspace where time reversal symmetry is accidentally restored for space-time trajectories of the density field ϕ. As a result, we were able to extract an effective free energy that encodes the screened Coulomb repulsion, which frustrates the bulk phase separation at a finite length-scale. Comparing with parameter regimes near the equilibrium subspace, we concluded that our exact mapping gives a good qualitative guide to the physical behaviour nearby.

Intrigued by the equilibrium subspace in Model AB, we studied the entropy production as a measure of the amount of time reversal symmetry breaking in a system, with the intention of looking at Model AB as a case study. Following the work of Seifert [27, 77], we defined the entropy production ΔS along a field trajectory as the log of the probability ratio between the forward and the backward path. The entropy production rate (EPR) can subsequently be obtained by taking the time derivative of ΔS. We formulated a general method for calculating the steady state EPR of spatio-temporal $(\partial_t\phi, \phi)$ trajectories for scalar field theories with additive noise (extensions to vectorial or tensorial theories would also be straightforward). The resulting EPR $\dot{S}_{\rm ss}[\phi]$ is non-negative for every field configuration ϕ and there also exists a local decomposition $\dot{s}(\boldsymbol{x})$ that is guaranteed to be non-negative. The latter is quadratic in the time-antisymmetric component of the dynamics $F_{\rm a}$, which has close relations with the antisymmetric currents in Macroscopic Fluctuation Theory [33]. Unsurprisingly, the time-asymmetric component $F_{\rm a}$ is identically zero in equilibrium and therefore so are $\dot{s}$ and $\dot{S}_{\rm ss}$.

To alleviate the problem that $\dot{S}_{\rm ss}$ requires the knowledge of the steady state distribution, we presented a perturbative expansion in the weak noise limit that only requires the steady state solution of the deterministic equation, which can be done numerically at a much lower computational cost compared to solving the full probability distribution. For Model AB, we found that the total steady state EPR goes continuously to zero as we approach the special equilibrium subspace, sharpening the claim that we expect similar physics in or near the subspace.

In fact, even in the special equilibrium subspace, although time reversal symmetry appears to be restored for the coarse-grained ϕ-field, the underlying microscopic dynamics remains strongly non-equilibrium, as shown in a separate calculation where we computed the EPR of the same model with additional information of the Model A and Model B contributions to the rate of change of density $\partial_t \phi$. The enlarged EPR does not vanish in the special equilibrium subspace, instead diverging in the low-noise limit, as the diffusive currents, which are now tracked, are irreversible at the deterministic level. In steady state, we can identify a non-negative spatial decomposition of this enlarged EPR that combines a Model A contribution related to the local chemical reactions and a Model B contribution from the diffusive currents. The comparison between the two EPRs shows that the entropy production is not an absolute quantity but depends on which degrees of freedom are followed and which are coarse-grained over.

Most studies presented in this thesis have been performed for small noise or in the deterministic limit. While this has been sufficient to understand the qualitative behaviours of our models and the scaling of EPR with ϵ in the weak noise limit, we observed that the noise strength plays a significant role in quantitative predictions such as the steady state pattern length (or droplet size) in Model AB, echoing the findings of Tjhung et al. for Model B+ [11]. Analytical progress without taking the weak noise limit may be possible by taking advantage of the exact free energy in the equilibrium subspace. Accordingly, the role of noise is certainly an interesting avenue to pursue for future research.

Bibliography

[1] Y. I Li and M. E Cates. Non-equilibrium phase separation with reactions: a canonical model and its behaviour. *J. Stat. Mech.: Theory Exp.*, 2020(5):053206, 2020.

[2] Y. I. Li and M. E. Cates. Hierarchical microphase separation in non-conserved active mixtures. *Eur. Phys. J. E*, 44:119, 2021.

[3] Y. I. Li and M. E. Cates. Steady state entropy production rate for scalar langevin field theories. *J. Stat. Mech. Theory Exp.*, 2021:013211, 2021.

[4] S. Ramaswamy. The mechanics and statistics of active matter. *Annu. Rev. Condens. Matter Phys.*, 1:323–345, 2010.

[5] M. C. Marchetti, J.-F. Joanny, S. Ramaswamy, T. B. Liverpool, J. Prost, M. Rao, and R. A. Simha. Hydrodynamics of soft active matter. *Rev. Mod. Phys.*, 85:1143, 2013.

[6] M. E. Cates and J Tailleur. Motility-induced phase separation. *Annu. Rev. Condens. Matter Phys.*, 6(1):219–244, 2015.

[7] C. A. Weber, D. Zwicker, F. Jülicher, and C. F. Lee. Physics of active emulsions. *Rep. Prog. Phys.*, 82:064601, 2019.

[8] V. Narayan, S. Ramaswamy, and N. Menon. Long-lived giant number fluctuations in a swarming granular nematic. *Science*, 317:105–108, 2007.

[9] J. Deseigne, S. Léonard, O. Dauchot, and H. Chaté. Vibrated polar disks: spontaneous motion, binary collisions, and collective dynamics. *Soft Matter*, 8:5629–5639, 2012.

[10] R. Singh and M. E. Cates. Hydrodynamically interrupted droplet growth in scalar active matter. *Phys. Rev. Lett.*, 123:148005, 2019.

[11] E. Tjhung, C. Nardini, and M. E. Cates. Cluster phases and bubbly phase separation in active fluids: reversal of the Ostwald process. *Phys. Rev. X*, 8:031080, 2018.

[12] J. Toner and Y. Tu. Long-range order in a two-dimensional dynamical XY model: how birds fly together. *Phys. Rev. Lett.*, 75:4326, 1995.

[13] T. Vicsek, A. Czirók, E. Ben-Jacob, I. Cohen, and O. Shochet. Novel type of phase transition in a system of self-driven particles. *Phys. Rev. Lett.*, 75:1226–1229, 1995.

[14] P. Romanczuk, M. Bär, W. Ebeling, B. Lindner, and L. Schimansky-Geier. Active brownian particles. *Europ. Phys. Jour. Special Topics*, 202:1–162, 2012.

[15] M. J. Schnitzer. Theory of continuum random walks and application to chemotaxis. *Phys. Rev. E*, 48:2553, 1993.

[16] H. C. Berg. *E. coli in Motion*. Springer, 2008.

[17] T. F. F. Farage, P. Krinninger, and J. M. Brader. Effective interactions in active brownian suspensions. *Phys. Rev. E*, 91:042310, 2015.

[18] É. Fodor, C. Nardini, M. E. Cates, J. Tailleur, P. Visco, and F. van Wijland. How far from equilibrium is active matter? *Phys. Rev. Lett.*, 117:038103, 2016.

[19] D. S. Dean. Langevin equation for the density of a system of interacting langevin processes. *J. Phys. A*, 29:L613, 1996.

[20] M. E. Cates and J. Tailleur. When are active brownian particles and run-and-tumble particles equivalent? consequences for motility-induced phase separation. *EPL*, 101:20010, 2013.

[21] P. C. Hohenberg and B. I. Halperin. Theory of dynamic critical phenomena. *Rev. Mod. Phys.*, 49:435–479, 1977.

[22] S. C. Glotzer, D. Stauffer, and N. Jan. Monte Carlo simulations of phase separation in chemically reactive binary mixtures. *Phys. Rev. Lett.*, 72:4109–4112, 1994.

[23] S. C. Glotzer, E. A. Di Marzio, and M. Muthukumar. Reaction-controlled morphology of phase-separating mixtures. *Phys. Rev. Lett.*, 74:2034–2037, 1995.

[24] S. C. Glotzer and A. Coniglio. Self-consistent solution of phase separation with competing interactions. *Phys. Rev. E*, 50:4241–4244, 1994.

[25] M. Tarzia and A. Coniglio. Lamellar order, microphase structures, and glassy phase in a field theoretic model for charged colloids. *Phys. Rev. E*, 75:011410, 2007.

[26] M. Tarzia and A. Coniglio. Pattern formation and glassy phase in the ϕ^4 theory with a screened electrostatic repulsion. *Phys. Rev. Lett.*, 96:075702, 2006.

[27] Seifert U. Stochastic thermodynamics, fluctuation theorems and molecular machines. *Rep. Prog. Phys.*, 75:126001, 2012.

[28] C. Jarzynski. Nonequilibrium equality for free energy differences. *Phys. Rev. Lett.*, 78:2690, 1997.

[29] J. Kurchan. Fluctuation theorem for stochastic dynamics. *J. Phys. A*, 31:3719, 1998.

[30] J. L. Lebowitz and H. Spohn. A gallavotti–cohen-type symmetry in the large deviation functional for stochastic dynamics. *J. Stat. Phys.*, 95:333–365, 1999.

[31] P. Pietzonka and U. Seifert. Entropy production of active particles and for particles in active baths. *J. Phys. A*, 51:01LT01, 2017.

[32] C. Nardini, É. Fodor, E. Tjhung, F. Van Wijland, J. Tailleur, and M. E. Cates. Entropy production in field theories without time-reversal symmetry: Quantifying the non-equilibrium character of active matter. *Phys. Rev. X*, 7:021007, 2017.

[33] L. Bertini, A. De Sole, D. Gabrielli, G. Jona-Lasinio, and C. Landim. Macroscopic fluctuation theory. *Rev. Mod. Phys.*, 87:593, 2015.

[34] M. Motoyama. Morphology of binary mixtures which undergo phase separation during chemical reactions. *J. Phys. Soc. Jpn.*, 65:1894–1897, 1996.

[35] M. Motoyama and T. Ohta. Morphology of phase-separating binary mixtures with chemical reaction. *J. Phys. Soc. Jpn.*, 66:2715–2725, 1997.

[36] S. Puri and H. L. Frisch. Segregation dynamics of binary mixtures with simple chemical reactions. *J. Phys. A*, 27:6027, 1994.

[37] S. Puri and H. L. Frisch. Phase separation in binary mixtures with chemical reactions. *Int. J. Mod. Phys. B*, 12:1623–1641, 1998.

[38] R. Lefever, D. Carati, and N. Hassani. Comment on "Monte Carlo simulations of phase separation in chemically reactive binary mixtures". *Phys. Rev. Lett.*, 75:1674, 1995.

[39] J. Berry, C. P. Brangwynne, and M. Haataja. Physical principles of intracellular organization via active and passive phase transitions. *Rep. Prog. Phys.*, 81:046601, 2018.

[40] W. M. Jacobs and D. Frenkel. Phase transitions in biological systems with many components. *Biophys. J.*, 112:683 – 691, 2017.

[41] A. A. Hyman, C. A. Weber, and F. Jülicher. Liquid-liquid phase separation in biology. *Ann. Rev. Cell Dev. Biol.*, 30:39–58, 2014.

[42] O. Wueseke, D. Zwicker, A. Schwager, Y. L. Wong, K. Oegema, F. Jülicher, A. A. Hyman, and J. B. Woodruff. Polo-like kinase phosphorylation determines Caenorhabditis elegans centrosome size and density by biasing SPD-5 toward an assembly-competent conformation. *Biol. Open*, 5:1431–1440, 2016.

[43] D. Zwicker, M. Decker, S. Jaensch, A. A. Hyman, and F. Jülicher. Centrosomes are autocatalytic droplets of pericentriolar material organized by centrioles. *Proc. Natl Acad. Sci. USA*, 111:E2636–E2645, 2014.

[44] M. E. Cates, D. Marenduzzo, I. Pagonabarraga, and J. Tailleur. Arrested phase separation in reproducing bacteria creates a generic route to pattern formation. *Proc. Natl Acad. Sci. USA*, 107:11715–11720, 2010.

[45] T Grafke, M. E. Cates, and E Vanden-Eijnden. Spatiotemporal self-organization of fluctuating bacterial colonies. *Phys. Rev. Lett.*, 119:188003, 2017.

[46] R. Wittkowski, A. Tiribocchi, J. Stenhammar, R. J. Allen, D. Marenduzzo, and M. E. Cates. Scalar ϕ^4 field theory for active-particle phase separation. *Nat. Commun.*, 5:4351, 2014.

[47] M. E. Cates and E. Tjhung. Theories of binary fluid mixtures: from phase-separation kinetics to active emulsions. *J. Fluid Mech.*, 836:1, 2018.

[48] F. Liu and N. Goldenfeld. Dynamics of phase separation in block copolymer melts. *Phys. Rev. A*, 39:4805–4810, 1989.

[49] C. B. Muratov. Theory of domain patterns in systems with long-range interactions of Coulomb type. *Phys. Rev. E*, 66:066108, 2002.

[50] C. Sagui and R. C. Desai. Ostwald ripening in systems with competing interactions. *Phys. Rev. Lett.*, 74:1119–1122, 1995.

[51] H. Hinrichsen. Non-equilibrium critical phenomena and phase transitions into absorbing states. *Adv. Phys.*, 49:815–958, 2000.

[52] U. C. Täuber. *Critical Dynamics: a Field Theory Approach to Equilibrium and Non-equilibrium Scaling Behavior*. Cambridge University Press, 2014.

[53] A. Lefevre and G. Biroli. Dynamics of interacting particle systems: stochastic process and field theory. *J. Stat. Mech.: Theory Exp.*, 2007:P07024, 2007.

[54] C. Gardiner. *Stochastic Methods*. Springer Berlin, 2009.

[55] N. G. Van Kampen. *Stochastic Processes in Physics and Chemistry*. Elsevier, 1992.

[56] J. Tailleur and M. E. Cates. Statistical mechanics of interacting run-and-tumble bacteria. *Phys. Rev. Lett.*, 100:218103, 2008.

[57] J. J. Christensen, K. Elder, and H. C. Fogedby. Phase segregation dynamics of a chemically reactive binary mixture. *Phys. Rev. E*, 54:R2212, 1996.

[58] D. Zwicker, A. A. Hyman, and F. Jülicher. Suppression of ostwald ripening in active emulsions. *Phys. Rev. E*, 92:012317, 2015.

[59] D Zwicker, R Seyboldt, C. A Weber, A. A Hyman, and F Jülicher. Growth and division of active droplets provides a model for protocells. *Nat. Phys.*, 13:408, 2017.

[60] J. P. Boyd. *Chebyshev and Fourier spectral methods*. Berlin: Springer, 2001.

[61] S. A. Orszag. On the elimination of aliasing in finite-difference schemes by filtering high-wavenumber components. *J. Atmos. Sci.*, 28:1074–1074, 1971.

[62] P. E. Kloeden and E. Platen. *Numerical solution of stochastic differential equations*. Springer Science & Business Media, 2013.

[63] S. A. Brazovskiĭ. Phase transition of an isotropic system to a nonuniform state. *J. Exp. Theor. Phys.*, 41:85, 1975.

[64] I. W. Hamley. *Block Copolymers in Solution: Fundamentals and Applications*. John Wiley & Sons, 2005.

[65] M. C. Cross and P. C. Hohenberg. Pattern formation outside of equilibrium. *Rev. Mod. Phys.*, 65:851–1112, 1993.

[66] M. Cross and H. Greenside. *Pattern Formation and Dynamics in Nonequilibrium Systems*. Cambridge University Press, 2009.

[67] P-G. De Gennes and J. Prost. *The Physics of Liquid Crystals*. Oxford University Press, 1993.

[68] W. Ostwald. Studien über die bildung und umwandlung fester körper. *Z. Phys. Chem.*, 22:289–330, 1897.

[69] I. M. Lifshitz and V. V. Slyozov. The kinetics of precipitation from supersaturated solid solutions. *J. Phys. Chem. Solids*, 19:35–50, 1961.

[70] A. J. Bray. Theory of phase-ordering kinetics. *Adv. Phys.*, 51(2):481–587, 2002.

[71] T Grafke and E Vanden-Eijnden. Non-equilibrium transitions in multiscale systems with a bifurcating slow manifold. *J. Stat. Mech.: Theory Exp.*, 2017:093208, 2017.

[72] Kyozi K. and Takao O. Kink dynamics in one-dimensional nonlinear systems. *Physica A*, 116:573 – 593, 1982.

[73] R. Wittkowski, A. Tiribocchi, J. Stenhammar, R. J. Allen, D. Marenduzzo, and M. E. Cates. Scalar φ 4 field theory for active-particle phase separation. *Nat Commun*, 5(1):1–9, 2014.

[74] A. Tiribocchi, R. Wittkowski, D. Marenduzzo, and M. E. Cates. Active model h: acalar active matter in a momentum-conserving fluid. *Phys. Rev. Lett.*, 115:188302, 2015.

[75] R. Singh and M. E. Cates. Hydrodynamically interrupted droplet growth in scalar active matter. *Phys. Rev. Lett.*, 123:148005, 2019.

[76] F. Caballero, C. Nardini, and M. E. Cates. From bulk to microphase separation in scalar active matter: A perturbative renormalization group analysis. *J. Stat. Mech.: Theory Exp.*, 2018:123208, 2018.

[77] U. Seifert. Entropy production along a stochastic trajectory and an integral fluctuation theorem. *Phys. Rev. Lett*, 95:040602, 2005.

[78] D. Mandal, K. Klymko, and M. R. DeWeese. Entropy production and fluctuation theorems for active matter. *Phys. Rev. Lett.*, 119:258001, 2017.

[79] S. Shankar and M. C. Marchetti. Hidden entropy production and work fluctuations in an ideal active gas. *Phys. Rev. E*, 98:020604, 2018.

[80] O. Niggemann and U. Seifert. Field-theoretic thermodynamic uncertainty relation. *J. Stat. Phys.*, 178:1–33, 2020.

[81] L. Dabelow, S. Bo, and R. Eichhorn. Irreversibility in active matter systems: Fluctuation theorem and mutual information. *Phys. Rev. X*, 9:021009, 2019.

[82] A. W. C. Lau and T. C. Lubensky. State-dependent diffusion: Thermodynamic consistency and its path integral formulation. *Phys. Rev. E*, 76:011123, 2007.

[83] T. Markovich, É. Fodor, E. Tjhung, and M. E. Cates. Thermodynamics of active field theories: Energetic cost of coupling to reservoirs. *Phys. Rev. X*, 11:021057, 2021.

[84] E. Fodor, R. L. Jack, and M. E. Cates. Irreversibility and biased ensembles in active matter: Insights from stochastic thermodynamics. *arXiv preprint arXiv:2104.06634*, 2021.

[85] D. Mukamel. Phase transitions in nonequilibrium systems. In M.E. Cates and M.R. Evans, editors, *Soft and fragile matter*, page 237. Taylor & Francis, 2000.

[86] P. M. Chaikin and T. C. Lubensky. *Principles of Condensed Matter Physics*. Cambridge University Press, 1995.

[87] M. E. Cates. Active field theories. *arXiv preprint arXiv:1904.01330*, 2019.

[88] L. Onsager and S. Machlup. Fluctuations and irreversible processes. *Phys. Rev.*, 91:1505, 1953.

[89] A. Borthne and R. Adhikari. Fluctuations, response, and self-sustained oscillations in an active cosserat solid. To appear.

[90] R. H. Bartels and G. W. Stewart. Solution of the matrix equation AX + XB = C. *Commun. ACM*, 15:820–826, 1972.